Quantum Dot Dissipation in Microwave Resonators

Toward High Bandwidth Charge Readout

Havir, Harald

2025

Citation for published version (APA):
Havir, H. (2025). *Quantum Dot Dissipation in Microwave Resonators: Toward High Bandwidth Charge Readout*. Department of Physics, Lund University.

Total number of authors:
1

Quantum Dot Dissipation in Microwave Resonators

Toward High-Bandwidth Charge Readout

HARALD HAVIR
DEPARTMENT OF PHYSICS | FACULTY OF ENGINEERING | LUND UNIVERSITY

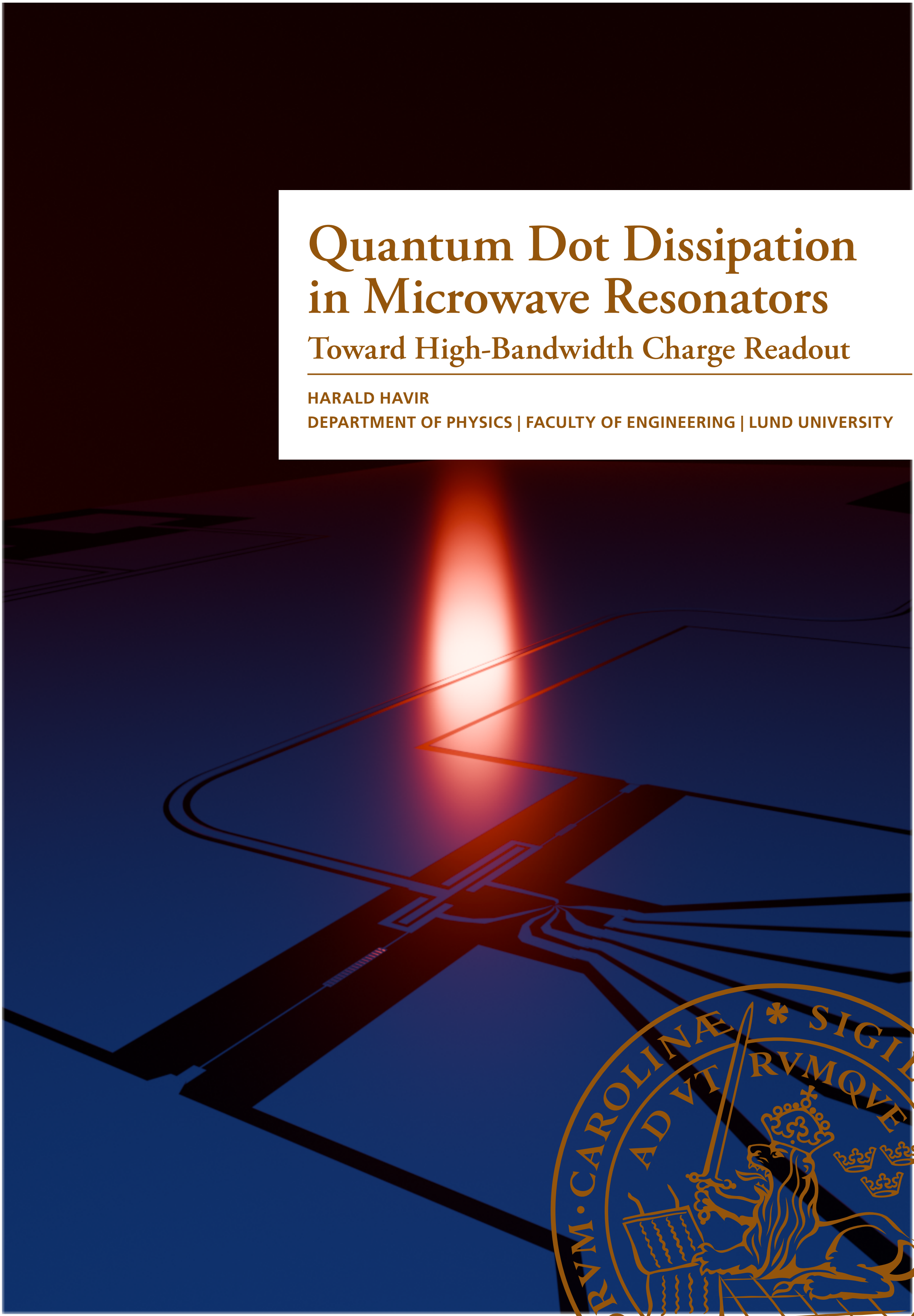

Quantum Dot Dissipation in Microwave Resonators

Quantum Dot Dissipation in Microwave Resonators

Toward High-Bandwidth Charge Readout

by Harald Havir

LUND
UNIVERSITY

Thesis for the degree of Doctor
Thesis advisors: Assoc. Prof. Ville F. Maisi, Prof. Peter Samuelsson
Faculty opponent: Prof. Natalia Ares

To be presented, with the permission of the Faculty of Engineering of Lund University, for public criticism in the Rydberg lecture hall at the Department of Physics on Friday, the 10th of October 2025 at 09:15.

DOKUMENTDATABLAD enl SIS 61 41 21

Organization
LUND UNIVERSITY

Department of Physics
Box 118
SE–221 00 LUND
Sweden

Document name
DOCTORAL DISSERTATION

Date of disputation
2025-10-10

Sponsoring organization

Author(s)
Harald Havir

Title and subtitle
Quantum Dot Dissipation in Microwave Resonators Toward High-Bandwidth Charge Readout

Abstract

Detecting a single elementary charge has become an important task to achieve as applications within quantum technologies such as for qubit readout, nanothermodynamics or single shot photodetection rely on the location of single electrons. The use of microwave resonators as the readout method for the charge sensitive single electron devices, such as quantum dots, has been extensively used to achieve high-speed charge readout. By matching the input impedance of the resonator to the high impedance of the quantum dot, this yields a large signal with a bandwidth set by the dissipation rate of the resonator. Most implementations of these systems use an external inductance which together with the parasitic capacitance of the input line forms a resonant circuit. This limits the resonance frequency and impedance of the resonator which sets an upper limit to the bandwidth of the resonator, limiting the maximum readout speed. By instead using the resonators typically employed in circuit quantum electrodynamics for this readout, this limit can be bypassed.

In Paper I, we study the dissipation in the quantum dot at these increased frequencies enabled by a coplanar waveguide resonator. Here, as the energy of the microwave photons is no longer negligible compared to the temperature of the sensor, additional transport in the QD becomes enabled. This results in increased dissipation for asymmetric QDs, and the appearance of spin-dependent dissipation. Additionally, we show that the photon energy broadens the linewidth of the quantum dot as seen by the microwave resonator, decreasing the maximum sensitivity of the sensor.

In Paper II, we use a high impedance Josephson junction (JJ) array resonator to further increase the readout bandwidth. We find here that by operating the resonator in the nonlinear regime, the added dissipation from the quantum dot sensor qualitatively changes the signal, enabling a frequency shift along the steep edge of the response. This leads to a near-unity signal without the need to satisfy the impedance matching condition imposed upon a linear resonator. By avoiding this matching condition we show that the bandwidth of the resonator can be further increased, allowing faster maximum readout speeds in the resonator. Finally, we discuss further benefits and limits to a high-impedance device operating in the nonlinear regime.

Key words
circuit quantum electrodynamics, low-dimensional transport, microwave resonators, quantum dots, charge sensing, nonlinearities

Classification system and/or index terms (if any)

Supplementary bibliographical information

Language
English

ISSN and key title

ISBN
978-91-8104-646-5 (print)
978-91-8104-647-2 (pdf)

Recipient's notes

Number of pages
138

Price

Security classification

I, the undersigned, being the copyright owner of the abstract of the above-mentioned dissertation, hereby grant to all reference sources the permission to publish and disseminate the abstract of the above-mentioned dissertation.

Signature ______________________ Date 2025-08-28

Quantum Dot Dissipation in Microwave Resonators

Toward High-Bandwidth Charge Readout

by Harald Havir

LUND
UNIVERSITY

A doctoral thesis at a university in Sweden takes either the form of a single, cohesive research study (monograph) or a summary of research papers (compilation thesis), which the licentiate student has written alone or together with one or several other author(s).

In the latter case the thesis consists of two parts. An introductory text puts the research work into context and summarizes the main points of the papers. Then, the research publications themselves are reproduced, together with a description of the individual contributions of the authors. The research papers may either have been already published or are manuscripts at various stages (in press, submitted, or in draft).

Cover illustration front: Render of a nanowire device connected to SQUID-array resonators.

Cover illustration back: Photo of the Maisi research group from 2024.

Funding information: The thesis work was financially supported in no particular order by: the Swedish Research Council (VR), The Foundational Questions Institute (FQXi), The Wallenberg Centre for Quantum Technology (WACQT), NanoLund, and the European Research Council (ERC).

Division of Solid State Physics
Department of Physics
Faculty of Engineering
Lund University

Box 118
SE-221 00 LUND
Sweden

isbn: 978-91-8104-646-5 (print)
isbn: 978-91-8104-647-2 (pdf)

Printed in Sweden by Media-Tryck, Lund University, Lund 2025

Life is hard,
we deserve our small celebrations.
-Tetris

Contents

List of publications

This thesis is based on the following publications, referred to by their Roman numerals:

I **Quantum Dot Source-Drain Transport Response at Microwave Frequencies**

H. Havir, S. Haldar, W. Khan, S. Lehman, K. A. Dick, C. Thelander, P. Samuelsson and V. F. Maisi
Phys. Rev. B **108**, 205417

II **Near-Unity Charge Readout in a Nonlinear Resonator without Matching**

H. Havir, A. Cicovic, P. Glidic, S. Haldar, S. Lehman, K. A. Dick, and V. F. Maisi
arXiv:2505.17709v1

Paper I is reproduced with permission of the publisher, paper II is reproduced with permission from the co-authors.

Publications not included in this thesis

III **High Impedance Microwave Resonators with Two-Photon Nonlinearities**

S. Andersson, **H. Havir**, S. Haldar, V.F. Maisi
Nat Commun **16**, 552 (2025)

IV **High Impedance Josephson Junction Resonators in the Transmission Line Geometry**
A. Ranni, **H. Havir**, S. Haldar, V.F. Maisi
Appl. Phys. Lett. **123**, 114002 (2023)

V **Energetics of microwaves probed by double quantum dot absorption**

S. Haldar, **H. Havir**, W. Khan, S. Lehmann, C. Thelander, K.A. Dick, V.F. Maisi
Phys. Rev. Lett. **130**, 087003 (2023)

VI **Continuous Microwave Photon Counting by Semiconductor-Superconductor Hybrids**
S. Haldar, D. Barker, **H. Havir**, A. Ranni, S. Lehmann, K.A. Dick, V.F. Maisi
Phys. Rev. Lett **133**, 217001 (2024)

VII **Coherence of an Electronic Two-Level System under Continuous Charge Sensing by a Quantum Dot Detector**
S. Haldar, M. Munk, **H. Havir**, W. Khan, S. Lehmann, C. Thelander, K.A. Dick, P. Samuelsson, P.P. Potts, V.F. Maisi
Phys. Rev. Lett **134**, 023601 (2025)

VIII **Decoherence in a crystal-phase defined double quantum dot charge qubit strongly coupled to a high-impedance resonator**
A. Ranni, S. Haldar, **H. Havir**, S. Lehmann, P. Scarlino, A. Baumgartner, C. Schönenberger, C. Thelander, K.A. Dick, P.P. Potts, V.F. Maisi
Phys. Rev. Research **6**, 043134 (2024)

IX **Microwave power harvesting using resonator-coupled double quantum dot photodiode**
S. Haldar, D. Zenelaj, P.P. Potts, **H. Havir**, S. Lehmann, K.A. Dick, P. Samuelsson, V.F. Maisi
Phys. Rev. B **109**, L081403 (2024)

Acknowledgements

I would like to thank my supervisor, **Ville**, for giving me the opportunity to pursue a Ph.D in his group and providing me with his support and guidance in my studies and research. You have been an excellent supervisor and always gave me every opportunity to perform excellent science. I also want to thank my co-supervisor **Peter** for always being approachable when I have questions about theory, and for always providing encouraging input into my work.

The other members of Ville's group have all provided useful feedback, advice and knowledge. For this, I want to thank **Waqar** for taking me under his wing when I first arrived here, **David** for his patience with my quantum dot questions, **Subhomoy** for the tireless efforts he has put into making- and teaching me how to make devices, and **Antti** for introducing me to the shadow evaporation techniques used in the cleanroom. Additionally, **Samuel**, **Andrea** and **Pierre**, you have all brought such an incredible atmosphere to the group and made every day a joy.

Next, all of my experimental work has been dependent on the use of nanowires expertly grown by **Sebastian**, **Claes** and **Kimberly**, without your contributions none of my work could have happened.

A lot of my work has also been helped by the weekly meetings with the device group. In addition to providing me with a space to present my own experimental data, I have had the pleasure of learning so much about your research topics as well. Particularly, I want to thank **Markus** who has worked on very similar nanowire quantum dots as I and been able to share in all of my experimental woes.

While science for the sake of science is a lot of fun, a good workplace helps plenty. The division of solid state physics is an excellent place to do work with immense support from all the cleanroom staff who are always keen and ready to provide support when processing issues arise, sometimes even off-hours. The administrative staff here have also been a joy to work with, not only for their stellar support in administrative tasks, but also for the extra effort they put into making the division a fun place to work at. Finally, the head of division, **Dan**, always makes

Last but not least, endless gratitude to my family, **Christin**, **Jiri**, **Wander** and of course my wonderful girlfriend **Helena** for all of your love, support and encouragement.

Populärvetenskaplig sammanfattning

Det nu berömda oljedroppsexperimentet, utfört år 1909 av Millikan och Fletcher var det experimentella arbetet som först bevisade att elektronisk laddning var kvantiserad i form av antal elektroner. Idag har teknologins utveckling gått så långt att vi kan utföra experiment där rörelsen av enstaka elektroner faktiskt spelar en roll, till exempel som den minsta beräkningskomponenten i en kvantdator, eller som resultatet av en interaktion, så som absorption av en foton. För att kunna genomföra dessa experiment behöver man kunna detektera närvaron av en enstaka elektron i en komponent. Detta görs tack vare kvantkomponenter vars ledningsförmåga är starkt beroende av den elektrostatiska omgivningen, bland annat så kallade kvantprickar som används i den här avhandlingen. Dessa komponenter fungerar som transistorer, som kan visa ett binärt resultat: 1 eller 0, beroende på om en elektron befinner sig i eller utanför den önskade komponenten. För att ta del av den här transistorns resultat så måste man därför genomföra en mätning av transistorns ledningsförmåga.

Det enklaste sättet att mäta ledningsförmågan är att mäta en ström genom kvantpricken. Då strömmen som genereras i dessa små kvantkomponenter är väldigt liten tar en sådan mätning dock lång tid. För att göra detta snabbare gör man istället en indirekt mätning genom att ansluta en högfrekvent resonator till kvantpricken. Resonatorn fungerar lite som en mikrovågsugn som ser till at den högfrekventa signalen (mikrovågorna) hålls inom en välbestämd volym där den kan studsa ända tills den interagerar med kvantpricken (maten). Med hjälp av en liten öppning i resonatorn kan man studera hur mycket av signalen som absorberas av kvantpricken, vilket beror på kvantprickens ledningsförmåga. Med den här avläsningsmetoden kan man göra mätningarna snabbare, med en hastighet proportionell mot frekvensen av mikrovågssignalen.

Denna avhandlingen innehåller resultat från två artiklar däri vi studerar mikrovågsresonatorer med en frekvens mellan 4 och 8 GHz och hur dessa interagerar med kvantprickar. I den första artikeln visar vi att vid mikrovågsfrekvenser kan energin lagrad i resonatorns oscillationer leda till ytterligare ledningsfenomen som inte har betydelse vid lägre frekvenser. I den andra artikeln studerar vi en icke-linjär resonator och visar att dess interaktioner med kvantprickarna leder till kvalitativt olika förändringar i den utlästa signalen från resonatorn, vilket resulterar i en bättre förmåga att urskilja kvantprickens tillstånd med kort mättid. Arbetet presenterat i avhandlingen hjälper således till att öka förståelsen för interaktionerna som tar plats i utläsningen av elementärladdningen, och kan användas för att genomföra dessa mätningarna snabbare än tidigare genomfört.

Popular science summary

The now famous oil-drop experiment, performed in year 1909 by Millikan and Fletcher was the experimental work that first proved that electric charge was quantized in the form of a whole number of electrons. Today, the advancement of technology has progressed far enough that we can perform experiments where the motion of individual electrons actually matters, for example as the smallest computational component of a quantum computer, or as the result of an interaction such as the absorption of a photon. In order to perform these experiments, one needs to be able to detect the presence of a single electron within a component. This is accomplished with the use of small quantum devices whose conductivity depends strongly on the electrical surroundings, for instance a quantum dot. These devices work as transistors that can show a binary result: 1 or 0, depending on if an electron is in or out of the measured component. In order to know the result of this device, however, one must perform a measurement of its conductivity.

The easiest way to measure conductivity of a quantum dot is to pass a current through it. However, as the current generated in these small quantum devices is very small, such a measurement takes a long time. In order to perform this readout faster, one instead makes an indirect measurement by connecting the quantum dot to a high-frequency resonator. This resonator works like a microwave oven that ensures that the high-frequency signal (the microwave) is contained within a specified volume where it can bounce back and forth until it interacts with the quantum dot (the food). Thanks to a small opening in the resonator, one can study how much of the signal is absorbed by the quantum dot, which depends on how well it conducts. With this readout method, one can make the measurements faster, with a speed proportional to the frequency of the microwave signal.

This thesis contains the results of two scientific papers where we study microwave resonators with a frequency between 4 - 8 GHz, and how these interact with quantum dots. In the first paper, we show that in this frequency range, the energy stored within the oscillations of the resonator can lead to additional conduction phenomena that are not present at lower frequencies. In the second paper we study a nonlinear resonator and show that its interactions with the quantum dot leads to qualitative differences in the readout signal from the resonator that result in a better ability to distinguish the two states of the quantum dot. The work presented in this thesis thus helps to increase the understanding for the interactions that take place in the readout of the elemental charge, and can thus be used to perform these measurements faster than previously accomplished.

Chapter 1

Introduction

The detection of single electrons in solid state materials has applications such as readout in Qubit systems [1–7], single shot microwave photodetection [8–11], metrological standards [12,13], studying cooper pair breaking [14–16] and nanothermodynamics and fluctuations [17–23]. To perform the charge readout on these systems of interest (SOI), a capacitive connection to a sensor, typically based off of single electron device such as quantum point contacts (QPCs) [24–28], single electron transistors (SETs) [29, 30] or quantum dots (QDs) [31–33] is implemented. A change in the charge on the SOI is then reflected in the current of the sensor which is to be measured. However, the high resistance set by the resistance quantum $R > 25.8$ kHz of the sensor along with the $C \approx 0.1$ pF/m capacitance of the coaxial cable connecting it to the amplifier typically results in a measurement bandwidth typically below tens of kiloherz [34–36]. This can be improved to MHz bandwidths by moving the amplification to the mK stage, which instead adds an experimental difficulty of increasing the necessary cooling power at the mixing chamber stage.

In 1998, an alternative detection method was proposed by Shoelkopf et. al. [37]. This detection scheme utilizes an electrical resonating circuit coupled to the sensor. As the sensor conductance acts as a source of dissipation in the microwave cavity, a measurement of the reflected signal from the cavity reveals the state of the sensor. The resonator here acts as an impedance matching network, allowing the high impedance of the sensor system to be coupled to a low impedance environment, where the readout speed is instead set by the linewidth of the resonator. This detection scheme has been heavily utilized in the past with resonators in the 100 MHz - 1 GHz frequency, enabling readout bandwidths ranging from 10 - 100 MHz range [38–50].

In addition to the large bandwidth, one needs the resonator to match the impedance of the sensor to the input impedance of the transmission line [35, 48, 51] to extract a large signal from the sensor for the fast readout. More precisely, the sensor dissipation κ_s needs to match the input coupling rate κ_c, which is responsible for determining the bandwidth of the resonator [49]. As the sensor dissipation depends on the conductance of the sensor, the bandwidth of the resonator cannot be set arbitrarily high as this would reduce the signal strength of the readout. Fortunately, both the input coupling and the sensor dissipation become more prominent with increasing resonance frequency. With the implementations based off of external matching networks, however, the parasitic capacitance used to form the resonant mode cannot be reduced further, preventing any increase to the resonance frequency.

In this thesis we study implementations to the resonance circuit based on the cavities used in circuit QED experiments [52] with resonance frequencies in the 4-8 GHz radio frequency (RF) band to extend the bandwidth of the resonator. At this frequency range, the photon energy in the cavity exceeds the electronic thermal energy in typical low-temperature transport experiments. This leads to additional ways for the microwave signal to dissipate into the quantum dot.

This is studied in Paper I where we use a coplanar waveguide resonator [53] to study the interaction between the sensor and the resonator. We find that the energy of the microwave photon enables dissipation for a larger range of energies than low frequency transport would permit, as photon absorption into the quantum dot becomes permitted. Furthermore, this photon absorption depends on the spin configuration of the quantum dot, leading to plateaus in the resonator response with respect to the energy level of the quantum dot which could be used for stable multi-level charge readout, as well as a reduction in the charge noise of the sensor. Additionally, we find that the dissipation for quantum dots with asymmetric barriers also greatly exceeds the low-frequency result.

Next, in paper II we use a resonator based on arrays of Josephson junctions [54, 55]. These provide a large kinetic inductance, allowing to make a high impedance device for larger coupling to the sensor. In addition to this, we show that the strongly nonlinear Josephson junctions [56, 57] operated with a dissipative charge sensor lead to a frequency shift across the steep slope in the nonlinear response as is used for the readout of superconducting qubits with an inherently dispersive readout [58–62]. Using this we avoid the matching condition, achieving a near-unity signal with a resonator with large internal losses and a small sensor dissipation. This opens up the use of higher bandwidths without sacrificing signal strength, which may enable high fidelity charge readout with 10 ns measurement times. Additionally, we see that the nonlinearities may enable protection against charge noise and backaction effects.

Chapter 2

Low Frequency Quantum Dot Transport

Quantum dots (QDs) are nanoscopic systems made from semiconductors[1] where the conducting electrons are prevented from moving freely in all three dimensions. By confining the electrons in all three dimensions the QD is effectively a zero-dimensional object which, just like in atoms, provides a discrete density of states, arising in part due to quantum mechanical confinement, and in part due to the coulomb repulsion between the negatively charged particles [64]. This discrete level spacing can be used to interact with light, with applications such as display technology [65], single-photon sources [66], lasing [67, 68], bio-imaging [69, 70] or solar cells [71]. Additionally, the QD can be electrically connected to an environment, where the discrete level spacing can be used as an energy filter for current transport, allowing for applications within quantum computation [5, 6], nano thermodynamics [19] or charge detection [72–75]. This chapter will focus on this last application of quantum dots, starting with a phenomenological description of electrically connected quantum dots.

2.1 Phenomenological Description

We consider the quantum dot as in Fig. 2.1 (a), where the electron island is connected to the environment via tunnel barriers with some capacitance $C_{\mathrm{L(R)}}$ resulting in a tunnel coupling $\Gamma_{\mathrm{L(R)}}$ to the left (right) metallic lead. The third terminal is an external

---

[1] Quantum confinement only becomes noticeable when the confinement is on the order of the wavelength of the electrons. Semiconductors have a notably longer wavelength as compared to metals, making this choice of material a necessity for quantum effects [63].

voltage source, called the gate voltage V_{G} which is also capacitively coupled to the island via a (weaker) capacitance C_{G}. With this, the total capacitance of the island, also called the self-capacitance is $C_{\Sigma} = C_{\mathrm{L}} + C_{\mathrm{R}} + C_{\mathrm{G}}$, which sets the charging energy for adding a single electron

$$E_C = \frac{e^2}{C_\Sigma}. \tag{2.1}$$

With this, Fig. 2.1 (b) shows an energy diagram of the quantum dot with the two leads having filled electron states up to the chemical potential $\mu_{\mathrm{L(R)}}$.

This is typically achieved by confining a conducting area from the surroundings using some potential barriers through which electronic transport is classically forbidden, but quantum mechanically permitted through tunneling [30].

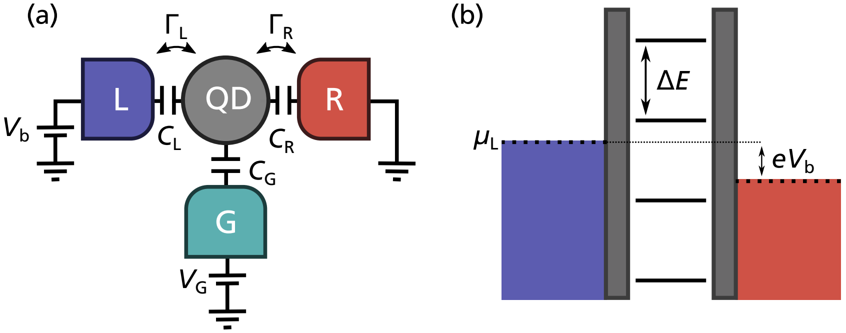

Figure 2.1: Schematic of a quantum dot with transport through the left (right) tunnel barrier of the quantum dot mediated by the tunnel coupling Γ_{L} (Γ_{R}). A voltage bias V_b between the two contacts defines a direction of transport, while the potential of the quantum dot is altered using the gate voltage V_G which is coupled to the dot via a capacitor.

Considering a quantum dot illustrated in Figure 2.1 with the tunnel barrier Γ_{L} (Γ_{R}) connecting it to the left (right) electron reservoir (henceforth referred to as "lead") we effectively end up with a three-level system where the electrons in the left (right) lead have chemical potential μ_{L} (μ_{R}) and the nearest available energy level in the quantum dot has energy ε. For an electron to enter from the left (right) lead it must have an energy equal to the energy of the available state in the quantum dot, and similarly for an electron to tunnel out of the dot, it must have an energy equal to some available state in the left (right) lead.

We can then control the transport through the quantum dot using two voltage sources: The gate voltage V_G is capacitively coupled to the quantum dot and is used to change the energy ε of the dot by an amount $\varepsilon = \alpha_G V_G$ where $\alpha_g = C_G/C_\Sigma$. The bias

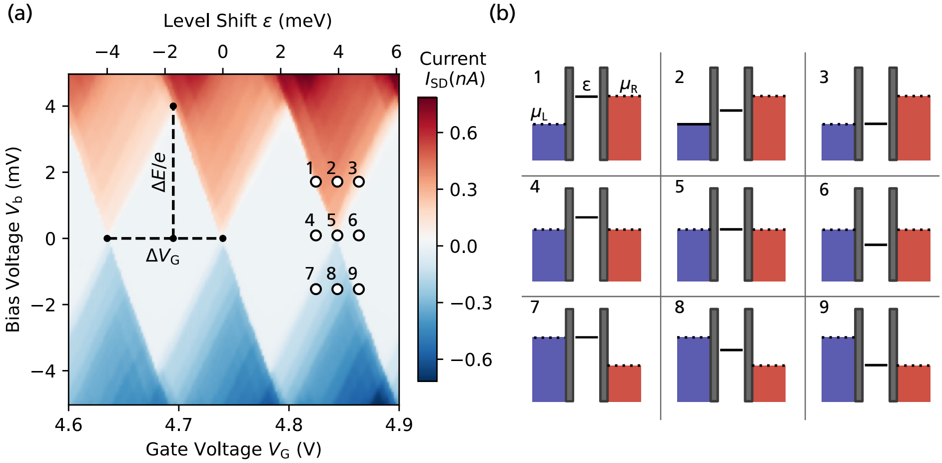

Figure 2.2: **(a)** Measurement data of the coulomb diamonds in a quantum dot. The vertical line shows the bias voltage required to add the next electron $\Delta E/e$, while the horizontal line shows the corresponding gate voltage ΔV_G. The axis on top shows the level shift $\varepsilon = \alpha_\mathrm{g}(V_\mathrm{G} - V_{\mathrm{G},0})$ **(b)** Illustration of the nine highlighted points from (a) showing schematically the energies of the left/right leads and the quantum dot.

voltage introduces a difference in energy between the two leads $\mu_\mathrm{R} - \mu_\mathrm{L} = eV_b$, which can be used to define a direction of transport through the dot.

A typical measurement to show the presence of quantum dots is to sweep both the gate voltage and bias voltage while measuring the current to produce the so-called charge stability diagram, and is shown for a real device in figure 2.2. From this measurement, we can find the charging energy ΔE as the vertical height of the diamonds as well as the corresponding gate voltage required to add another electron ΔV_G. The ratio between these gives the lever arm, α_g and the slope of the diamonds gives the relative ratio of the capacitances. Finally, we see evidence of some excited states, which are visible as additional diagonal lines within the conducting region of the measured data.

2.2 Zero-Bias Conductance

Instead of considering the current, we can study the differential conductance dI/dV_b of the quantum dot, which tells how much the quantum dot current changes in response to a small bias voltage. Figure 2.4 (a) shows the differential conductance from the previously presented coulomb diamonds. We see that the conductance appears as sharp lines outlining the diamond pattern, with additional lines within the regions of finite current. These additional lines correspond to excited states, and will not be further elaborated on herein, but are discussed in more detail in Ref. [76].

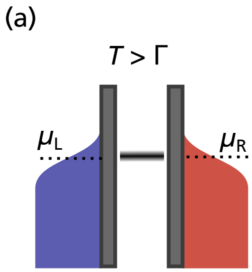

Figure 2.3: Transport through the quantum dot occurs for a range of energies due to **(a)** the Fermi-Dirac distribution in the leads **(b)** the lifetime broadening of the quantum dot due to the large tunnel rates Γ or **(c)** both of these simultaneously.

Describing the conductance mathematically in general is a quite difficult task, however near zero bias, the current depends linearly on the bias voltage in what is known as the linear response regime. Here, mathematical descriptions of the conductance are easier to derive as a function of the tunnel couplings in the quantum dot. Taking a higher resolution measurement conductance at zero bias voltage, as in figure 2.4 (b) with respect to the gate voltage reveals that it rises from zero in coulomb blockade to some maximum value after which it diminishes again, producing a line with some height G_{max} and width σ. The finite width of the line arises due to one or both of the following: First, the temperature of the system causes the electron distribution in the leads to not be perfectly sharp, but instead follow the Fermi-Dirac distribution, $f = \left(1 + e^{\varepsilon/k_\text{B}T}\right)^{-1}$, which leads to a range of energies on the order of $k_\text{B}T$ for which there are electrons and holes accessible for tunneling transport. Second, as the electrons confined on the quantum dot only remain there for a finite time τ, after which they tunnel out via the barriers, the energy of the confined state is smeared by the Heisenberg uncertainty principle, giving a linewidth of $\Gamma \propto \hbar/\tau$. Whichever of these broadening energy scales dominates, typically sets the transport properties of the quantum dot, which will now be discussed in more detail.

2.2.1 Weakly Coupled Quatum Dot

In the weak-coupling limit the tunnel couplings Γ are much smaller than the thermal energy $k_\text{B}T$, meaning that the quantum dot level can be treated effectively as a delta function. The transport here can be analyzed microscopically as the system is well-described by a particle current of electrons tunneling across the barriers with a rate $\Gamma/\hbar$, and theories treating this limit are hence called "sequential tunneling" theories. By studying the system around zero bias in the so-called linear regime, where the current varies linearly with the applied bias voltage, analytical solutions for the

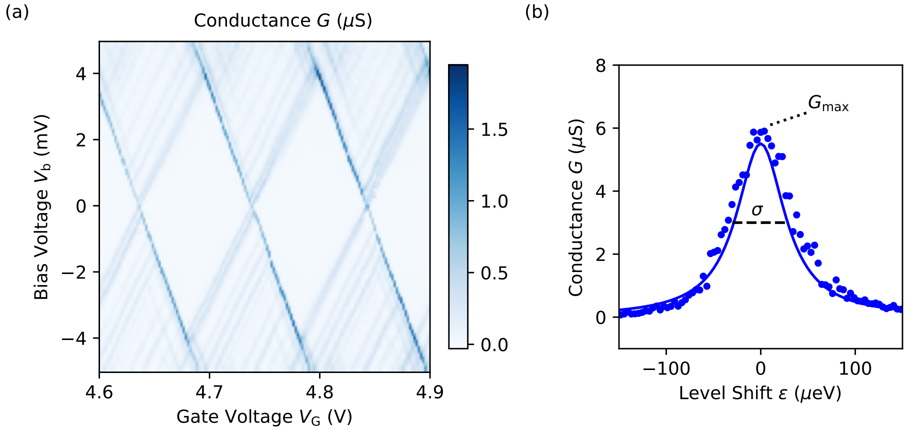

Figure 2.4: **(a)** The differential conductance of the quantum dot as a function of the gate and bias voltage. **(b)** an example of the zero bias conductance in the lifetime broadening limit with $\Gamma_1 = 60\ \mu$S and $\Gamma_2 = 2.3\ \mu$S. The linewidth σ and maximum conductance G_{max} are indicated.

conductance can be derived [29], [77]. In the limit where only one level contributes to the current, i.e. $k_{\mathrm{B}}T \ll e^2/C_\Sigma$, the conductance is

$$G_0 \frac{\pi}{2} \frac{\Gamma_{\mathrm{L}}\Gamma_{\mathrm{R}}}{k_{\mathrm{B}}T(\Gamma_{\mathrm{L}}+\Gamma_{\mathrm{R}})} f(\varepsilon/k_{\mathrm{B}}T) f(-\varepsilon/k_{\mathrm{B}}T) \tag{2.2}$$

where ε is the level shift of the electronic state contributing to the current. From this equation, we can find analytical values for $G_{\mathrm{max}} = \frac{e^2}{4k_{\mathrm{B}}T\hbar}\frac{\Gamma_{\mathrm{L}}\Gamma_{\mathrm{R}}}{\Gamma_{\mathrm{L}}+\Gamma_{\mathrm{R}}}$ and $\sigma \approx 3.52 k_{\mathrm{B}}T$

2.2.2 Coherent transport theory

As the tunnel rates increase, sequential tunneling models considering only one simultaneous tunneling event become unreliable as co-tunneling events become more frequent [78]. In this limit, the transport can be understood through Landauer-Büttiker theory [79, 80] which provides another avenue to calculate the zero-bias conductance given the tunnel couplings Γ_{L}, Γ_{R} of the QD. This approach considers the electrons as non-interacting elastic scatterers where the conductance is given by the transmission of the system. These are not trivial assumptions to make as quantum dots are described by electron-electron interactions, but end up describing the zero bias conductance well, while completely ignoring the effects of charging energy.

To begin, we consider the quantum dot as a resonant system coupled to the two leads, with tunnel rates $\Gamma_{\mathrm{L}}/\hbar$, $\Gamma_{\mathrm{R}}/\hbar$ and a single non-interacting transport channel. As there is some finite lifetime for any state on the dot, this can be seen as a decaying system with a finite lifetime broadening $\Gamma = \Gamma_{\mathrm{L}} + \Gamma_{\mathrm{R}}$. The Breit-Wigner formula [81] gives the transmission of the QD as energies ε, given the dot energy ε_i

$$T(\varepsilon) = \frac{\Gamma_{\mathrm{L}}\Gamma_{\mathrm{R}}}{(\varepsilon - \varepsilon_i)^2 + (\Gamma/2)^2}. \tag{2.3}$$

For transport to occur, we need an available state in the left lead, and an empty state in the right lead at an energy E or vice versa. The electron flow at this energy will then be proportional to the difference in filling between the two leads, as well as the transmission of the dot, while the total flow will then be given by the sum of the flows at all different energies, or

$$I(\varepsilon) = \frac{e}{h}\int_{-\infty}^{\infty} T(\varepsilon) f(\varepsilon - \mu_{\mathrm{L}})(1 - f(\varepsilon - \mu_{\mathrm{R}}))d\varepsilon. \tag{2.4}$$

At low bias ($\mu_{\mathrm{L}}, \mu_{\mathrm{R}} \approx \mu$), the current is linear with respect to the bias, and the conductance $G = dI/dV$ can be written as

$$G(\varepsilon) = \frac{e^2}{h}\int_{-\infty}^{\infty} T(\varepsilon)\frac{df(\varepsilon - \mu)}{d\varepsilon}d\varepsilon \tag{2.5}$$

for each non-interacting transport channel [2]. This equation can be fitted to find the tunnel couplings Γ_{L} and Γ_{R} of the system, but it can also be further treated in the two limits of low temperature and high temperature.

Lifetime Broadening Limit: For low temperatures such that $k_{\mathrm{B}}T \ll \Gamma$, the Fermi distributions are sharp in comparison to the lifetime of the dot, which in the limit $T \to 0$ results in the analytic solution of the integral

$$G(\varepsilon) = -\frac{e^2}{h}T(\varepsilon)\int_{-\infty}^{\infty} \frac{df(\varepsilon)}{d\varepsilon}d\varepsilon = \frac{e^2}{h}\frac{\Gamma_{\mathrm{L}}\Gamma_{\mathrm{R}}}{(\varepsilon - \varepsilon_i)^2 + (\Gamma_{\mathrm{L}} + \Gamma_{\mathrm{R}})^2/4}. \tag{2.6}$$

In this limit, the conductance through the quantum dot is thus only dependent on the barriers and the tunnel couplings for each barrier can be uniquely determined, given a measurement of the conductance.

High Temperature Limit: In the high temperature limit, the Fermi distribution is smeared such that it is constant in the neighborhood of ε_i. The integral of equation

---

[2] Typical quantum systems have two transport channels as there are two electron states (spin up vs down) at each energy. The overall conductance is thus multiplied by an additional factor of two.

(2.5) then yields

$$\begin{aligned} G(\varepsilon) =& \frac{e^2}{h}\int_{-\infty}^{\infty} T(\varepsilon')\frac{df(\varepsilon')}{d\varepsilon'}d\varepsilon' = \\ =& \frac{e^2}{h}\int_{-\infty}^{\infty} T(\varepsilon')\frac{df(\varepsilon')}{d\varepsilon'}|_{\varepsilon'=\varepsilon-\varepsilon_i}d\varepsilon' = \\ =& \frac{e^2}{4k_\mathrm{B}T\hbar}\frac{\Gamma_\mathrm{L}\Gamma_\mathrm{R}}{\Gamma_\mathrm{L}+\Gamma_\mathrm{R}}\frac{1}{\cosh^2(\frac{\varepsilon-\varepsilon_i}{2k_\mathrm{B}T})}, \end{aligned}$$

which is the same expression as in the weak coupling limit presented previously.

2.3 Charge Detection

In order to use the quantum dot as a charge detector, we measure the current as a function of gate voltage at some fixed bias voltage. In figure 2.5 we see $I_\mathrm{SD}(V_G)$ for a finite (positive) bias voltage, where we observe clear periodic steps in the current as we successively access higher charge states of the quantum dot. In these steep slopes, the current thus changes quickly for a small change in gate voltage.

If we now consider a secondary system of interest (SOI) which is capacitively coupled to our quantum dot, the charge state on the SOI will cause an effective gate voltage shift ΔV_G to the quantum dot. If the quantum dot is then tuned to one of these sensitive points and the charge configuration on the SOI changes, we will as a result see a changing current flowing through the quantum dot, granting us information about what caused this change. By then measuring the current as a function of time we can observe electron tunneling events in real time.

The bandwidth (temporal resolution) of this charge detection is typically set by the amplification circuit, as some finite averaging time is required in order to determine the current with sufficient precision to make a measurement, and is typically on the order of some kHz, but this can be improved by moving to high frequency readout methods which will be discussed in the following chapters.

2.4 Double Quantum Dots

2.4.1 Charge Configuration

By placing two QDs in series, connected to each other, as illustrated in Fig. 2.6, we end up with a double quantum dot (DQD). In these systems, we have two bound states

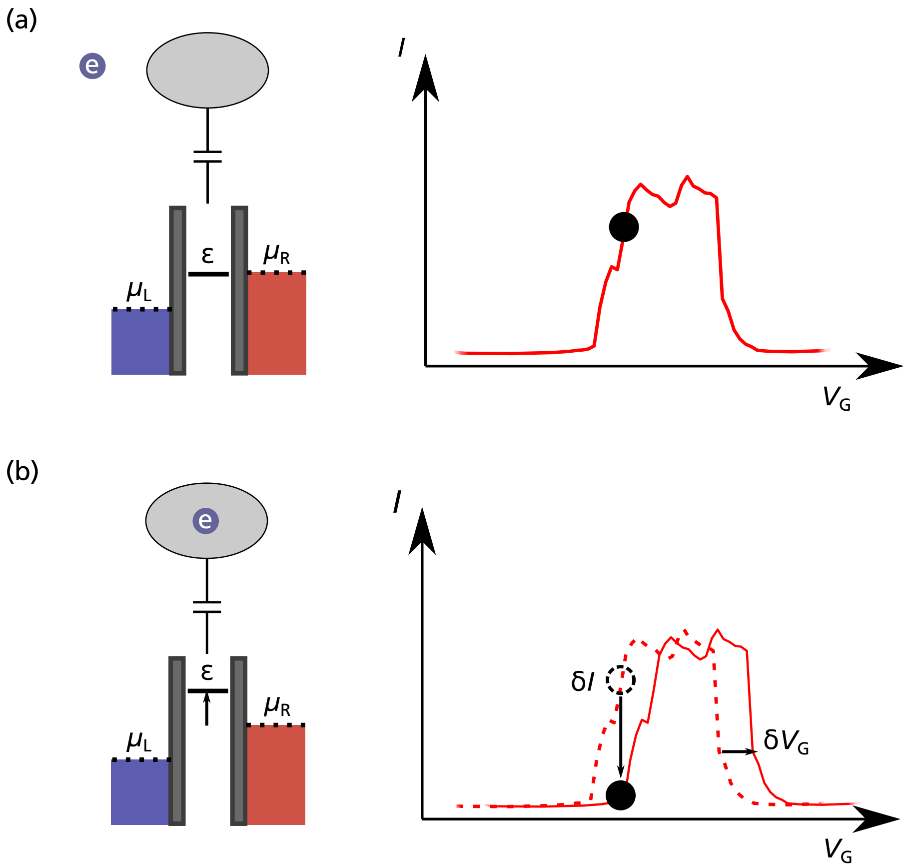

Figure 2.5: Illustration of the charge detector operation. **(a)** The quantum gate voltage V_{G} is set to where there is a large slope in the current. **(b)** An electron (blue circle) is added to the sensed system (gray ellipse). The additional charge offsets the gate voltage, resulting in a reduced current I through the sensor.

where we can tune the energy difference between the states to make qubits [82, 83], information engines [19, 84], photon emitters [85, 86] or absorbers [8, 10]. Within this thesis, we have used the charge sensitive quantum dot to probe a DQD. This section will thus introduce the charge configuration seen in the experiments, following Ref. [87].

We begin by viewing the DQD as two single-level systems that are controlled by external gate voltages. The total electrostatic energy of the double quantum dot is then

$$U = \frac{1}{2}\left(E_{\mathrm{CL}} N_{\mathrm{L}}^2 + E_{\mathrm{CR}} N_{\mathrm{R}}^2\right) + N_{\mathrm{L}} N_{\mathrm{R}} E_{\mathrm{Cm}} + f(V_{\mathrm{GL}}, V_{\mathrm{GR}}).$$

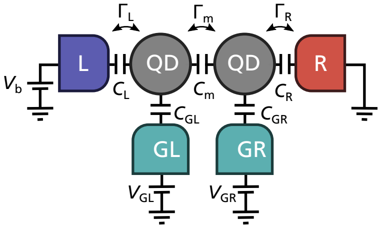

Figure 2.6: Schematic illustration of a double quantum dot. The coupling between the two dots takes the form of an additional interdot tunnel barrier with capacitance C_{m} and corresponding tunnel rate Γ_m.

Here, $E_{\mathrm{C,L(R)}}$ is the charging energy of the left (right) quantum dot given by

$$E_{\mathrm{CL}} = \frac{e^2}{C_{\Sigma,\mathrm{L}}}\left(\frac{1}{1-\frac{C_{\mathrm{m}}^2}{C_{\Sigma,\mathrm{L}}C_{\Sigma,\mathrm{R}}}}\right)$$

$$E_{\mathrm{CR}} = \frac{e^2}{C_{\Sigma,\mathrm{R}}}\left(\frac{1}{1-\frac{C_{\mathrm{m}}^2}{C_{\Sigma,\mathrm{R}}C_{\Sigma,\mathrm{L}}}}\right),$$

E_{Cm} is the energy shift on the left (right) due to the addition of an electron in the right (left) dot

$$E_{\mathrm{Cm}} = \frac{e^2}{C_{\mathrm{m}}}\left(\frac{1}{\frac{C_{\Sigma,\mathrm{L}}C_{\Sigma,\mathrm{R}}}{C_{\mathrm{m}}^2}-1}\right),$$

and $f(V_{\mathrm{GL}}, V_{\mathrm{GR}})$ is the energy shift due to the external gate voltage

$$\begin{aligned} f(V_{\mathrm{GL}}, V_{\mathrm{GR}}) = {} & \frac{1}{e}\left[C_{\mathrm{GL}}V_{\mathrm{L}}\left(N_{\mathrm{L}}E_{\mathrm{CL}} + N_{\mathrm{R}}E_{\mathrm{Cm}}\right) + C_{\mathrm{GR}}V_{\mathrm{R}}\left(N_{\mathrm{R}}E_{\mathrm{CR}} + N_{\mathrm{L}}E_{\mathrm{Cm}}\right)\right] \\ & + \frac{1}{e^2}\left[\frac{1}{2}C_{\mathrm{GL}}^2V_{\mathrm{L}}^2E_{\mathrm{CL}} + C_{\mathrm{GR}}^2V_{\mathrm{R}}^2E_{\mathrm{CR}} + C_{\mathrm{GL}}C_{\mathrm{GR}}V_{\mathrm{L}}V_{\mathrm{R}}E_{\mathrm{Cm}}\right] \end{aligned}$$

We see that the charging energy terms are the same as those of a single dot, with a correction term due to the cross-capacitance C_{m}. Removing this cross capacitance, we end up with two separate quantum dots, as illustrated in Fig. 2.7 (a). Here, an increase in the left (right) gate voltage only changes the number of electrons on the left (right) quantum dot. If we instead increase the coupling between the two dots, the left (right) gate voltage instead changes the energy of both dots equally. In this case, the DQD acts essentially as a single quantum dot with two separate gate voltages, as in Fig. 2.7 (b). The corresponding charge stability diagrams, shown in Fig. 2.7 (c), and (d) show the regions of fixed charge that result from varying the gate voltages in these two cases.

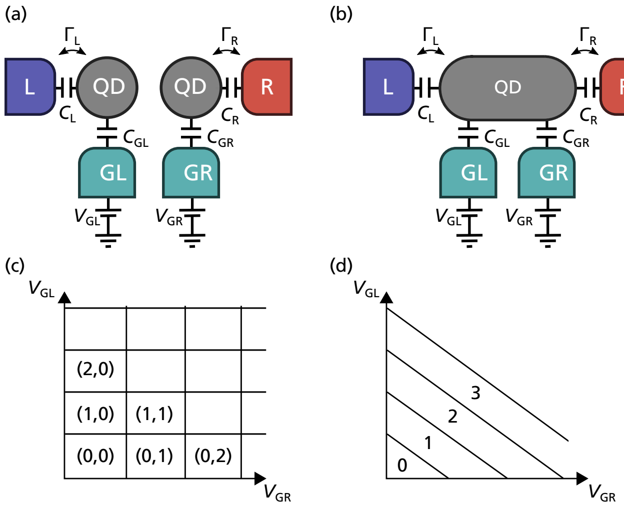

Figure 2.7: Two extreme cases of the value of C_m illustrated. **(a)** shows the case where $C_\mathrm{m} = 0$, resulting in two fully separated quantum dots whereas **(b)** shows the case where $C_\mathrm{m} \to \infty$ such that the two dots are fully coupled into one larger quantum dot. **(c)** and **(d)** show then the corresponding charge stability diagrams, with the number of electrons labeled as (L, R) in (c) and with the total number of electrons in (d).

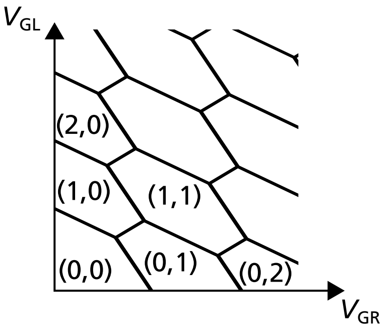

Figure 2.8: The charge stability diagram of a double quantum dot with an intermediate value of C_m with the number of electrons on the left and right dot indicated by the numbers (L,R).

With an intermediate value of C_m instead, the additional cross-coupling results in an additional energy required to add pairs of electrons. This separates the corners of the square stability diagram from each other, resulting in a hexagonal pattern as in Fig. 2.8 (a). We also note that increasing the gate voltages now have an effect on the number of electrons in the opposite dot, leading to the hexagonal pattern being slanted.

2.4.2 Finite-Bias Transport

Thus far, we have only consider the unbiased DQD, adding a bias voltage across the DQD will, just as for the QD allow current to flow only in some energy level configurations. Just as for the single QD, we can make an energy diagram where we see that for current to flow, we need to let an electron tunnel sequentially from one lead to another via the two dots. In Fig. 2.9 we show energy diagrams for a set bias voltage, with our gate voltages tracing the edge of electron transport. Starting with case 1, we here have a large detuning between the two gates, such that both energy levels just barely fit within the bias window. As we move down within the figure, the detuning shrinks, allowing us to shift both energy levels higher / lower in energy while still remaining within the current transport window. At the bottom, both levels are aligned, allowing the gate voltage to sweep the entire biasing window. Notably, shifting the detuning direction of the quantum dots (such that the right dot is lower in energy than the left in this case), the electron transport becomes blocked, as the electron would get stuck in the lower-energy dot without opportunity to tunnel out.

This results in the triangle-shaped region of current transport in the charge stability diagram of Fig. 2.9, which emerges at each of the triple points. The solid lines here indicate the boundaries of the charge regions, which compared to the dotted lines for the unbiased transport shows that the charge regions have shifted as a result of the applied bias voltage. Notably, we know that the width of the base (tracing the points 4-6) corresponds in energy to the applied bias voltage. This allows us to establish an energy scale in the direction of the interdot transition line. Similarly, a horizontal (vertical) line from point 1 will at the intersect with the interdot transition line gives the lever arm for the right (left) gate voltage.

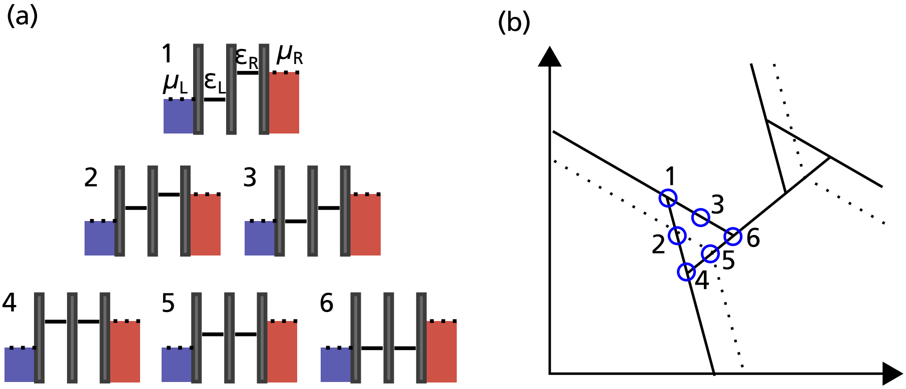

Figure 2.9: **(a)** Six energy diagrams showing the edge states for which current transport is permitted in a DQD with a finite bias across it. **(b)** The emerging finite bias triangle in the charge stability diagram.

Chapter 3

Linear Resonators

Resonating systems in general are systems in which a signal with a specific frequency will oscillate back and forth. This resonance comes as a consequence of two *dispersive* elements which enable an internal transfer of energy with minimal losses. Springs or pendulums are examples of mechanical resonators in which a mass is raised and lowered in a periodic fashion, as the energy is transferred between being entirely potential to being entirely kinetic. Electrical resonators typically transform energy in the form of accumulated charge on a capacitor to current through an inductor. This chapter will cover the essential details needed to understand the input/output transport properties of microwave resonators that make them useful as readout circuits for dissipative quantum systems.

3.1 Coplanar Waveguide Resonators

In the work presented in this thesis, microwave resonators have been coupled to quantum dots in order to study the dissipative response at the microwave frequency range for the purpose of fast charge readout. These are constructed using a long floating superconducting strip as pictured in figure 3.1 (a), with capacitors defined by gaps in the transmission line. These coplanar waveguide cavities do not have single ”lumped” elements where all of the circuit capacitance, inductance, or conductance are located. Instead, the line is better understood as a continuous line with some distributed parameters L_s, C_s, R_s, and G_s as shown in figure 3.1 (b). At resonance the electric field and current in the resonator oscillates in a standing wave. This allows the mapping of L_S, and C_S into their lumped-element equivalences $L = \frac{2L_\mathrm{S}l}{\pi^2}$, $C = \frac{C_\mathrm{S}l}{2}$ that describe the resonator response close to the fundamental resonance frequency [53].

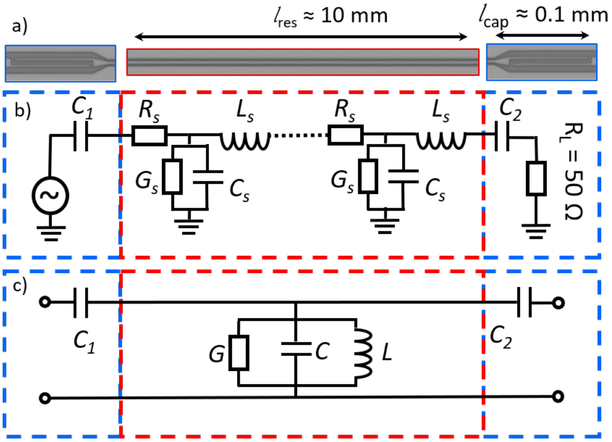

Figure 3.1: (a) Composite pictures from an optical microscope showing the geometry of a bare, two-port coplanar waveguide. The light gray areas are the Niobium which constitutes the waveguide and the ground plane, while the dark gray areas are the gaps. **(b)** The distributed element representation of the waveguide. **(c)** The equivalent lumped element circuit.

The loss terms R_s and G_s result in a total loss term captured by the lumped element conductance G. In the coming sections, we will mathematically describe the system, ending up in an expression for the reflection coefficient r of the resonator [1]. We will do this first by considering a quantized LC oscillator, followed by a two-port network approach.

3.2 Hamiltonian Solution

3.2.1 Quantization of an LC circuit

The simplest form of electrical resonator is the lumped element LC resonator, which consists of closed circuit with a capacitor and inductor. An illustration of this circuit is shown in Figure 3.2. In this system, the energy moves from being stored as a charge on the capacitor with capacitance C, to a magnetic field in the inductor with inductance L. This shift of energy oscillates back and forth with a resonance frequency ω_r.

Conventionally, the energy stored in the oscillator is pictured as arising from the movement of electric charge q, such that the electrons in the conductor form a potential energy by charging up the capacitor $E_{\mathrm{pot}} = \frac{1}{2C}q^2$. This potential energy is then transformed into kinetic energy as the capacitor discharges and creates a current

---

[1] The words ”reflection coefficient” are to describe the amplitude reflection coefficient r, the magnitude of this quantity $|r|$, and its square - the power reflection coefficient $R = |r|^2$ depending on context. I try to make it clear which definition is considered at any point within this thesis.

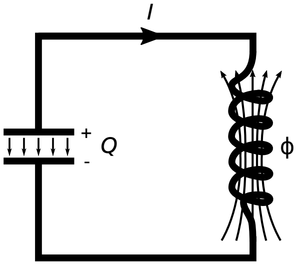

Figure 3.2: The simplest electrical oscillator consisting of only a single inductor L and capacitor C.

flow through the inductor where $E_{\text{kin}} = \frac{L}{2}I^2 = \frac{L}{2}\dot{q}^2$. However, one can just as well consider the magnetic flux ϕ stored in the inductor as the variable, such that the potential energy is given by $E_{\text{pot}} = \frac{1}{2L}\phi^2$. The corresponding kinetic energy is then $E_{\text{kin}} = \frac{C}{2}\dot{\phi}^2$, where the time-derivative of the flux gives rise to a voltage $V = L\dot{I} = \dot{\phi}$. Despite being a less intuitive picture, the choice of using the flux as the variable becomes convenient later on when we will introduce non-linearities to the inductance L.

We write the Hamiltonian of the LC oscillator

$$H = \frac{1}{2C}Q^2 + \frac{\phi^2}{2L}, \tag{3.1}$$

and we can promote the variables Q and ϕ to quantum operators by enforcing the canonical commutation relation

$$\left[\hat{Q}, \hat{\phi}\right] = -i\hbar. \tag{3.2}$$

Although the oscillations in energy are readily viewed as a collective motion of electrons in the resonator, the quantized excitations herein can just as well be viewed as photons with creation- and annihilation operators

$$\hat{a}^\dagger = -i\frac{1}{\sqrt{2C\hbar\omega_{\text{r}}}}\hat{Q} + \frac{1}{\sqrt{2L\hbar\omega_{\text{r}}}}\hat{\phi} \tag{3.3}$$

$$\hat{a} = i\frac{1}{\sqrt{2C\hbar\omega_{\text{r}}}}\hat{Q} + \frac{1}{\sqrt{2L\hbar\omega_{\text{r}}}}\hat{\phi}. \tag{3.4}$$

Here we see as a sanity check that the product of the two ladder operators yields the photon number

$$\hat{a}^\dagger\hat{a} = \frac{E_{\text{pot}} + E_{\text{kin}}}{\hbar\omega_r} = n, \tag{3.5}$$

which enables us to write the Hamiltonian

$$\hat{H}_{\text{LC}} = \hbar\omega_{\text{r}}(\hat{a}^\dagger\hat{a} + \frac{1}{2}). \tag{3.6}$$

This is the familiar solution to a quantum harmonic oscillator with eigenstates corresponding to an integer number of photons with energy $E_n = \hbar\omega_\mathrm{r}$ residing in the cavity.

3.2.2 Input-Output Theory

So far, the Hamiltonian only describes the energy of the oscillating mode within the cavity. However, this is an experimentally boring system, as there is no way to probe and study its dynamics. In order to do this, we need to couple the cavity to the environment. Physically, we do this by introducing a capacitive [53, 88] or inductive [88,89] coupling to the current or voltage antinodes respectively. This forms an input-output port for the photons in the cavity. In order to model this system theoretically, I will follow closely Refs. [90,91], where we model the environment as a Bosonic bath.

3.2.2.1 One-Port Resonator

We begin by considering our oscillator to be coupled via a single port to an environment made from a large number of independent Bosonic modes with Hamiltonian

$$\hat{H}_{\text{bath}} = \sum_q \hbar\omega_q \hat{b}_q^\dagger \hat{b}_q, \tag{3.7}$$

where b and $b^\dagger$ are the creation and annihilation operators of the bath, and q labels the different (orthogonal) modes. We next consider the interaction Hamiltonian for energy-conserving intcoperactions where a photon is transferred from the oscillator and into the bath or vice versa

$$\hat{H}_{\text{int}} = -i\hbar \sum_q (f_q \hat{a}^\dagger \hat{b}_q - f_q^* \hat{b}_q^\dagger a), \tag{3.8}$$

with f_q representing the amplitude of the interaction for mode q.

Together with the Hamiltonian of the bare LC oscillator we find the system Hamiltonian

$$\hat{H} = \hat{H}_{\text{LC}} + \hat{H}_{\text{bath}} + \hat{H}_{\text{int}} \tag{3.9}$$

from which we can find the equation of motion (EOM) for a bath mode

$$\dot{\hat{b}}_q = \frac{i}{\hbar}\left[\hat{H}, \hat{b}_q\right] = -i\omega_q b_q + f_q \hat{a}, \tag{3.10}$$

which is the EOM of a forced linear oscillator that has an exact solution

$$\hat{b}_q(t) = e^{-i\omega_q(t-t_0)}\hat{b}_q(t_0) + \int_{t_0}^{t} d\tau e^{-i\omega_q(t-\tau)} f_q^* \hat{a}(\tau) \tag{3.11}$$

where t_0 represents a time long before the interaction of any wave-packet with the cavity.

Similarly, the EOM for the LC oscillator is

$$\dot{\hat{a}} = -i\omega_{\mathrm{r}}\hat{a} - \sum_q f_q \hat{b}_q. \tag{3.12}$$

Inserting (3.11) into the second term now yields

$$\sum_q f_q \hat{b}_q = \sum_q \left(f_q e^{-i\omega_q(t-t_0)} \hat{b}_q(t_0) + \int_{t_0}^{t} d\tau |f_q|^2 e^{-i\omega_q(t-\tau)} \hat{a}(\tau) \right). \tag{3.13}$$

We will aim to make this expression a bit more palatable starting by noting that the decay rate from a simple harmonic oscillator of frequency ω_c is given by the Fermi Golden Rule expression

$$\kappa(\omega_c) = 2\pi \sum_q |f_q|^2 \delta(\omega_c - \omega_q) \tag{3.14}$$

from which it follows that

$$\int_{-\infty}^{\infty} d\nu \frac{\kappa(\omega_c + \nu)}{2\pi} e^{-i\nu(t-\tau)} = \sum_q |f_q|^2 e^{-i(\omega_q - \omega_c)(t-\tau)}. \tag{3.15}$$

Making the Markov approximation that $\kappa(\nu) = \kappa$ is constant for a frequency range relevant to the cavity, we find that

$$\sum_q |f_q|^2 e^{-i(\omega_q - \omega_c)(t-\tau)} = \kappa\delta(t-\tau) \tag{3.16}$$

where we now can multiply by the factor $1 = e^{i\omega_r(t-\tau)}e^{-i\omega_r(t-\tau)}$ to insert

$$\begin{aligned} \sum_q \int_{t_0}^{t} d\tau e^{-i\omega_q(t-\tau)} f_q^* \hat{a}(\tau) &= \int_{t_0}^{t} d\tau \sum_q |f_q|^2 e^{-i(\omega_q - \omega_{\mathrm{r}})(t-\tau)} \hat{a} e^{-i\omega_{\mathrm{r}}(t-\tau)}(\tau) \\ &= \int_{t_0}^{t} d\tau \kappa\delta(t-\tau)\hat{a}e^{-i\omega_{\mathrm{r}}(t-\tau)}(\tau) = \frac{\kappa}{2}\hat{a} \end{aligned} \tag{3.17}$$

where the final equality is given by

$$\int_{-\infty}^{x_0} dx\ \delta(x - x_0) = \frac{1}{2}. \tag{3.18}$$

Inserting this into our equation of motion (3.12) we find

$$\dot{\hat{a}} = -i\omega_{\mathrm{r}}\hat{a} - \frac{\kappa}{2}\hat{a} - \sum_q f_q e^{-i\omega_q(t-t_0)}\hat{b}_q(t_0), \tag{3.19}$$

where the second term is a linear damping of the cavity under the implemented approximations.

We now apply the Markov approximation to the coupling strength f_q, stating that the interaction amplitude $f \equiv \sqrt{|f_q|^2}$ is constant for all relevant modes q, and define the constant density of states

$$\rho = \sum_q \delta(\omega_c - \omega_q) \tag{3.20}$$

such that

$$\kappa = 2\pi f^2 \rho. \tag{3.21}$$

with this, the third term in the Eq. (3.19) above can be described as a simple "input mode"

$$\hat{b}_{in} \equiv \frac{1}{\sqrt{2\pi\rho}} \sum_q e^{-i\omega_q(t-t_0)}\hat{b}_q(t_0) \tag{3.22}$$

giving the final EOM for the cavity

$$\dot{\hat{a}} = -i\omega_{\mathrm{r}}\hat{a} - \frac{\kappa}{2}\hat{a} - \sqrt{\kappa}\hat{b}_{\mathrm{in}}(t). \tag{3.23}$$

By changing the limits on the integral in (3.11), to instead consider the time until the distant future t_1, we similarly define an output mode

$$\hat{b}_{\mathrm{out}} \equiv \frac{1}{\sqrt{2\pi\rho}} \sum_q e^{-i\omega_q(t-t_1)}\hat{b}_q(t_1) \tag{3.24}$$

and equation of motion

$$\dot{\hat{a}} = -i\omega_{\mathrm{r}}\hat{a} + \frac{\kappa}{2}\hat{a} - \sqrt{\kappa}\hat{b}_{\mathrm{out}}. \tag{3.25}$$

where the sign difference in the second term here arises from changing the integration bounds.

By subtracting Eq. (3.23) from Eq. (3.25) and rearranging, we end up with

$$\hat{b}_{\mathrm{out}} = \sqrt{\kappa}\hat{a} + \hat{b}_{\mathrm{in}}(t). \tag{3.26}$$

The interpretation of this equation is that the outgoing mode at the boundary of interaction is given by the reflected incoming mode, and whatever is radiated from the cavity. Now, finally we describe the spectral domain of $\hat{a}$ by taking the Fourier transform of Eq. (3.23):

$$\hat{a}(\omega) = \frac{i\sqrt{\kappa}}{(\omega - \omega_\mathrm{r}) + i\kappa/2}\hat{b}_\mathrm{in}(\omega) \tag{3.27}$$

By using Eq. (3.26), we see that we can write this as

$$\hat{b}_\mathrm{out}(\omega) = \left(1 - \frac{i\kappa}{(\omega - \omega_\mathrm{r}) + i\kappa/2}\right)\hat{b}_\mathrm{in}(\omega) \equiv r(\omega)\hat{b}_\mathrm{in}(\omega) \tag{3.28}$$

where $r(\omega)$ is the reflection coefficient of the microwave cavity. We see that with only a single input/output port, the reflected signal is equal in magnitude to the input signal, with only a phase difference depending on the frequency. At the resonance frequency, the signal is reflected with a phase shift of π, such that $r = -1$.

3.2.2.2 Two-Port Resonator

Next, we consider a system with two input/output ports. Doing this, we will treat the second port in exactly the same manner as before, with an additional bath and interaction Hamiltonian for the new Bosonic modes described by the creation- and annihilation operators $\hat{c}$ and $\hat{c}^\dagger$. With this additional second port, Eq. (3.23) and (3.25) turns into

$$\dot{\hat{a}}(t) = -i\omega_\mathrm{r}\hat{a}(t) - \frac{\kappa}{2}\hat{a}(t) - \sqrt{\kappa_1}\hat{b}_\mathrm{in}(t) - \sqrt{\kappa_2}\hat{c}_\mathrm{in}(t) \tag{3.29}$$

$$\dot{\hat{a}}(t) = -i\omega_\mathrm{r}\hat{a}(t) + \frac{\kappa}{2}\hat{a}(t) - \sqrt{\kappa_1}\hat{b}_\mathrm{out}(t) - \sqrt{\kappa_2}\hat{c}_\mathrm{out}(t), \tag{3.30}$$

where κ_1 and κ_2 are the coupling rates to each respective bath, and $\kappa = \kappa_1 + \kappa_2$ is the total coupling rate. Again, Fourier transforming the above equations, we find

$$\hat{a}(\omega) = -i\left(\frac{\sqrt{\kappa_1}\hat{b}_\mathrm{in}(\omega)}{(\omega - \omega_\mathrm{r}) + i\kappa/2} + \frac{\sqrt{\kappa_2}\hat{c}_\mathrm{in}(\omega)}{(\omega - \omega_\mathrm{r}) + i\kappa/2}\right). \tag{3.31}$$

Looking at the output from port 1, and making again the substitution from Eq. (3.26), we find

$$\hat{b}_\mathrm{out} = \left(1 - \frac{i\kappa_1}{(\omega - \omega_c) + i\kappa/2}\right)\hat{b}_\mathrm{in} + \left(\frac{-i\sqrt{\kappa_1\kappa_2}}{(\omega - \omega_c) + i\kappa/2}\right)\hat{c}_\mathrm{in} \tag{3.32}$$

where we thus have the reflection- and transmission coefficients

$$r_1 = 1 - \frac{i\kappa_1}{(\omega - \omega_c) + i\kappa/2} \tag{3.33}$$

$$t = \frac{-\sqrt{\kappa_1\kappa_2}}{(\omega - \omega_c) + i\kappa/2} \tag{3.34}$$

If we instead were interested in the output from port 2, we would simply exchange $1 \leftrightarrow 2$ in the indices above. The transmission coefficient of course is identical with this transformation, whereas the reflection coefficient depends on which port the reflection occurs from.

3.2.2.3 One-Port Resonator with Internal Losses

One consequence of making experiments is that the system is not only coupled to the environment via the intended input/output ports. Spurious leakage of the resonance mode can occur due radiation, coupling to two-level fluctuators in the substrate, or imperfections in the resonator leading to internal resistance [92, 93]. All of these lead to additional losses which can be treated as an additional port to the environment. A system with one input/output port by design, is thus equivalent to a two-port system, where the second port is the accumulated coupling of the environment. We can thus use all of our expressions derived for a two-port resonator but with a helpful relabeling of $1 \rightarrow c$ for the coupling port and $2 \rightarrow i$ for the internal losses. The equation for the reflection coefficient then reads

$$r = 1 - \frac{i\kappa_c}{i\kappa/2 - (\omega - \omega_\mathrm{r})}, \tag{3.35}$$

where $\kappa = \kappa_c + \kappa_i$.

3.2.2.4 Photon Number

Finally, we will consider the number of photons $\langle n\rangle = \langle \hat{a}^\dagger \hat{a}\rangle$ stored inside the cavity as a result of some number of incident photons $\langle \hat{b}_\mathrm{in}^\dagger \hat{b}_\mathrm{in}\rangle$, which corresponds to an input power P_0 as

$$P_0 = \hbar\omega \langle \hat{b}_\mathrm{in}^\dagger \hat{b}_\mathrm{in}\rangle, \tag{3.36}$$

where we have assumed that $\hat{c}_\mathrm{in} = 0$. Next, we use Eqs. (3.26) and (3.31) to find an expression for the number of photons in the cavity

$$\langle \hat{a}^\dagger \hat{a}\rangle = \frac{\kappa_c \langle \hat{b}_\mathrm{in}^\dagger \hat{b}_\mathrm{in}\rangle}{(\omega - \omega_\mathrm{r})^2 + \kappa^2/4} = \frac{\kappa_c}{(\omega - \omega_\mathrm{r})^2 + \kappa^2/4} \frac{P_0}{\hbar\omega} \tag{3.37}$$

Assuming that we drive the resonator at the resonance frequency $\omega = \omega_\mathrm{r}$ we find

$$\langle n\rangle = \frac{4\kappa_c}{\kappa^2} \frac{P_0}{\hbar\omega_\mathrm{r}}. \tag{3.38}$$

3.3 Circuit Solution

Alternatively, one can consider resonator as a circuit, for which the reflection coefficient is defined as

$$r = \frac{Z - Z_0}{Z + Z_0} \tag{3.39}$$

where Z is the impedance of the resonator and Z_0 is the impedance of the environment, which is typically set to $Z_0 = 50\ \Omega$. For the simple LC oscillator of Fig. 3.2, we find the impedance

$$Z = \left(i\omega C + \frac{-i}{\omega L} \right)^{-1} . \tag{3.40}$$

We see that this impedance is imaginary for all frequencies, aside from the resonance frequency

$$\omega_r = \frac{1}{\sqrt{LC}} \tag{3.41}$$

where the LC oscillator has a vanishing impedance, resulting again in the reflection coefficient $r = -1$ for an undamped resonator[2]. Before proceeding, we also define the characteristic impedance

$$Z_\mathrm{r} = \sqrt{L/C}, \tag{3.42}$$

as the ratio of the voltage to current oscillations in the resonator.

By treating the resonator this way, we no longer capture the quantum properties of the resonator, however, we will instead gain insight into the connection between the the circuit elements and the resonator parameters which we defined in the previous sections. Just as before, however, we aim to discuss slightly more involved systems than the bare uncoupled resonator. To make these calculations convenient, we will now move see the system as a two-port network where each component in the network is represented by a transmission matrix.

3.3.1 Transmission Matrices

The transmission matrix (ABCD parameters) [94] relates the incoming (V_1, I_1) and outgoing (V_2, I_2) voltage and current signals for a two-port system as shown in figure 3.3 with a matrix of the form

$$\begin{bmatrix} V_1 \\ I_1 \end{bmatrix} = \begin{bmatrix} A & B \\ C & D \end{bmatrix} \begin{bmatrix} V_2 \\ I_2 \end{bmatrix} . \tag{3.43}$$

---

[2] Note here that the resonance frequency depends on the total inductance and capacitance of the circuit. Adding input/output ports will therefore change the frequency correspondingly.

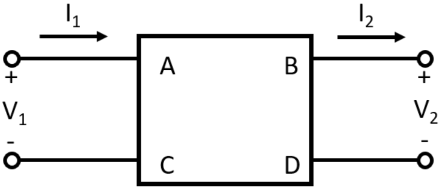

Figure 3.3: Two-port network with input parameters V_1, I_1 and output parameters V_2, I_2 related by a transmission matrix.

This transmission matrix representation easily treats cascading system each with transmission matrix T_i as

$$T_\Sigma = \prod_i T_i \tag{3.44}$$

allowing a more complex system to be easily represented by its smaller components, where the smallest units have tabulated solutions commonly presented in textbooks [94][3].

For the purposes of calculating the reflection coefficient we are more interested in the voltage waves being transmitted or reflected, so we additionally define a matrix

$$\begin{bmatrix} V_i^+ \\ V_i^- \end{bmatrix} = \frac{1}{2} \begin{bmatrix} 1 & Z_0 \\ 1 & -Z_0 \end{bmatrix} \begin{bmatrix} V_i \\ I_i \end{bmatrix} \tag{3.45}$$

which we can use to transform between the two bases, which will yield us a voltage transmission matrix T such that

$$\begin{bmatrix} V_1^+ \\ V_1^- \end{bmatrix} = T \begin{bmatrix} V_2^+ \\ V_2^- \end{bmatrix}. \tag{3.46}$$

3.3.2 Two-port resonator

Now, we consider a resonator with inductance L, capacitance C and conductance G coupled to the environment using two capacitors, C_1 and C_2, as illustrated in figure 3.4.

The system can be seen as three cascading systems where the input / output capacitors are seen as series impedances

$$Z = \frac{1}{j\omega C}, \tag{3.47}$$

---

[3] or on Wikipedia.

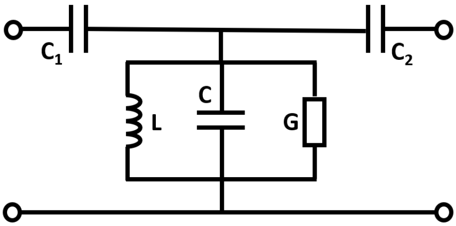

Figure 3.4: A circuit diagram of a two-port resonator with an internal inductance L, capacitance C and conductance G

while the resonator is seen as a shunt admittance

$$Y = G + j\omega C + \frac{1}{j\omega L} \tag{3.48}$$

From the aforementioned tables, we can find the corresponding transmission matrices, which in our voltage basis look like

$$T_Z = \begin{bmatrix} 1 - \frac{Z}{2Z_0} & \frac{Z}{2Z_0} \\ -\frac{Z}{2Z_0} & 1 + \frac{Z}{2_Z 0} \end{bmatrix} \tag{3.49}$$

$$T_Y = \begin{bmatrix} 1 + \frac{Z_0 Y}{2} & \frac{Z_0 Y}{2} \\ -\frac{Z_0 Y}{2} & 1 - \frac{Z_0 Y}{2} \end{bmatrix} \tag{3.50}$$

Defining the unitless quantities

$$z_i = \frac{Z_i}{2Z_0},\ y = YZ_0/2.$$

gives the transmission matrix for the resonator

$$T = \begin{bmatrix} 1 + z_1 & -z_1 \\ +z_1 & 1 - z_1 \end{bmatrix} \begin{bmatrix} 1 + y & y \\ -y & 1 - y \end{bmatrix} \begin{bmatrix} 1 + z_2 & -z_2 \\ +z_2 & 1 - z_2 \end{bmatrix}. \tag{3.51}$$

Now, assuming that $V_2^- = 0$ (i.e. we do not have any incoming voltage signals from the output port), we can find the reflection amplitude as

$$r \equiv \frac{T_{21}}{T_{11}} = \frac{(z_1 + z_2 - y) + 2(z_1 - z_2)y + 4z_1 z_2 y}{1 + (z_1 + z_2 + y) + 2(z_1 + z_2)y + 4z_1 z_2 y} \tag{3.52}$$

yielding the power reflection coefficient of the circuit

$$R = |r|^2. \tag{3.53}$$

3.3.3 Single-Port Resonator

Noting from the previous discussion that a vanishing C_2 still allows for matching to occur, we will consider the case where $C_2 \to 0 \Rightarrow z_2 \to \infty$. From equation (3.52) we then find a simplified expression for the reflection coefficient

$$r = \frac{(1-2y)+4z_1y}{(1+2y)+4z_1y} = 1 - \frac{4y}{(1+2y)+4z_1y}. \tag{3.54}$$

$$1 - \frac{-\frac{C_c^2\omega^2 Z_0}{C_\Sigma}\frac{Y}{\omega C_c}}{-\left(\frac{C_c^2\omega^2 Z_0}{2C_\Sigma}\frac{Y}{\omega C_c} + \frac{iG}{2C_\Sigma}\right) - (\omega_\mathrm{r} - \omega)}, \tag{3.55}$$

Here we have defined $\omega_\mathrm{r} = 1/\sqrt{LC}$, and assumed that $\omega \approx \omega_\mathrm{r}$ such that $(\omega^2 - \omega_\mathrm{r}^2) \approx 2\omega_\mathrm{r}(\omega - \omega_\mathrm{r})$ and $\omega/\omega_\mathrm{r} \approx 1$.

We recognize from this the same form as Eq. (3.35), where we can then define

$$\kappa_i = \frac{G}{C_\Sigma} = GZ_\mathrm{r}\omega_\mathrm{r} \tag{3.56}$$

and

$$-i\kappa_c = \frac{C_c^2\omega^2 Z_0}{C_\Sigma}\frac{Y}{\omega C_c}. \tag{3.57}$$

Expanding the last term here, we find that

$$\frac{Y}{\omega C} = \left(\frac{G}{\omega C_c} + i\frac{C}{C_c} - i\frac{\omega_\mathrm{r}^2 C_\Sigma}{\omega^2 C_c}\right) \approx \left(\frac{G}{\omega C_c} - i\right) \tag{3.58}$$

with our previously implemented assumption that $\omega \approx \omega_\mathrm{r}$. Additionally, the first term can be compared to the internal losses of the resonator $G/C_c > G/C_\Sigma = \kappa_i$. Assuming that the internal losses are small compared to the resonance frequency, this term is then small compared to unity, allowing us to safely ignore it. Thus, we find that

$$\kappa_c = \frac{C_c^2\omega_\mathrm{r}^2 Z_0}{C_\Sigma}. \tag{3.59}$$

3.4 Input Matching

From inspection of Eq. (3.35) we find the reflection coefficient at the resonance frequency

$$r(\omega_\mathrm{r}) = 1 - \frac{2\kappa_c}{(\kappa_c + \kappa_i)}, \tag{3.60}$$

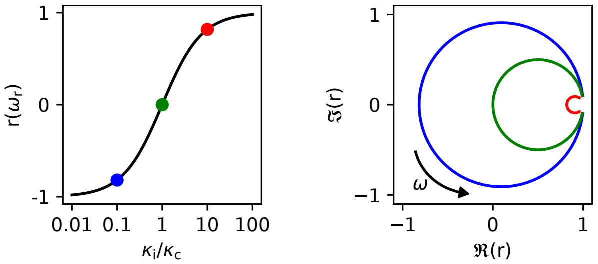

Figure 3.5: (a) The value of the reflection coefficient at the resonance frequency $\omega = \omega_r$ as a function of the ratio κ_i/κ_c. Three points are indicated at the ratios $\kappa_i/\kappa_c = 0.1$ (blue), 1 (green) and 10 (red). **(b)** The full response of the three indicated cases plotted in the complex plane. The arrow indicates the direction of increasing frequency

which is shown for various ratios of κ_c/κ_i in Fig. 3.5. We see that for both small and large κ_i, the magnitude of the reflected signal is the same $|r| = 1$, however, the phase of the reflected signal is different in the two cases. For small internal losses, the interaction with the cavity causes the signal phase to shift by π, whereas large internal losses lead to no phase shift whatsoever. This is highlighted in Fig. 3.5 (b) where we show the full complex response of the resonator as the frequency is varied for the three cases indicated by colored points in Fig. 3.5 (a). Here we see that, when the internal losses equal the input coupling $\kappa_i = \kappa_c$, none of the signal is reflected as all of the ingoing signal is absorbed by the cavity. In this case, the resonator is said to be matched as the resonator impedance equals the input impedance Z_0. Next, if $\kappa_c \gg \kappa_i$ (blue), the response is clearly distinct from the background due to the large phase shift despite not varying much in magnitude. Finally, if $\kappa_c \ll \kappa_i$ (red), however, the resonator response is nearly indistinguishable from that of the off-resonant reflected signal as everything is reflected at the input port. As these two cases depend on the magnitude of the input coupler, we label these cases as over- and undercoupled respectively.

3.5 Resonator Reflectometry

In resonator reflectometry, the resonator is connected to an additional system that causes a change in the resonator response in one or both of the following ways. First, dispersive systems, such as superconducting qubits [58–62] lead to a shift in the fundamental resonance frequency δf as one would achieve by adding a capacitance (or inductance) to the system. Second, the system can add dissipation $\kappa_s = G_s/C_\Sigma$ through a conductance G_s added to the resonator, such as from an SET [49, 95–97], quantum point contact [26, 38, 98] or quantum dot [44].

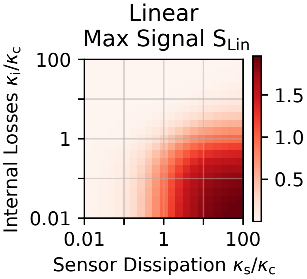

Figure 3.6: The maximum signal $|\Delta r|$ possible to achieve using a linear resonator as a function of κ_i/κ_c and κ_s/κ_c.

3.5.1 Signal strength and the matching condition

For the dissipative case, the signal difference at $\omega = \omega_r$ between a reference state with $\kappa_s = 0$ and one with a finite dissipation is

$$|\Delta r(\omega_r)| = 2\kappa_c \left(\frac{1}{\kappa_c + \kappa_i} - \frac{1}{\kappa_c + \kappa_i + \kappa_s} \right) = \frac{2\kappa_c}{\kappa} \left(\frac{\kappa_s}{\kappa + \kappa_s} \right), \tag{3.61}$$

where $\kappa = \kappa_i + \kappa_c$. We see from the equation that there are two conditions that should be satisfied to achieve a large readout signal. The first term tells us that the input coupling should be large relative to the linewidth of the resonator, or equivalently: we need small internal losses $\kappa_i \ll \kappa_c$. The second term tells us that the added dissipation κ_s should be large compared to the linewidth $\kappa_s \geq \kappa$. In Fig. 3.6 we visualize this matching condition by plotting Eq. (3.61) as a function of κ_s/κ_c and κ_i/κ_c. We see exactly this matching condition appear as the signal is maximized in the lower right corner - corresponding to $\kappa_s \gg \kappa_c \gg \kappa_i$.

3.5.2 Measurement Time

For real time resolved experiments, the aim to distinguish the signal difference between two (or more) states as soon as possible [38, 99]. For this, we need to have a high signal to noise ratio (SNR) and a large signal bandwidth. By satisfying the matching condition above, the signal is maximized, enabling a high SNR, provided that the noise level is sufficiently small [4].

The bandwidth of the measurement, then, is set by the linewidth κ of the resonator [49, 100]. We see this as the rate with which the resonator reaches equilibrium in the

---

[4] This is achieved by ensuring that the signal is amplified at the low temperature stages of the dilution refrigerator.

amount of cavity photons (and thus the rate of escaping photons) after its properties change. To increase the bandwidth then, we need κ_c to be sufficiently large, which according to the above matching condition sets a minimum dissipation κ_s that can be used. The measurement speed attainable is thus directly set by the conductance of the sensor.

Chapter 4

High Frequency Quantum Dot Transport

Typical implementations for the reflectometry readout rely on the use of tank circuits with resonance frequency of 100 MHz $- 1$ GHz, enabling readout bandwidths in the 10 MHz range [35]. By instead implementing the microwave resonators used in circuit QED experiments, we can access the $4 - 8$ GHz microwave band. Here, the energy of the microwave photons $E_{\mathrm{ph}} = \hbar\omega_{\mathrm{r}} \approx 15 - 30$ μeV exceeds the thermal energy arising from the electronic bath temperature $k_{\mathrm{B}}T \approx 5$ μeV typically achieved in dilution refrigerator units at $T = 50$ mK [52]. This leads to additional transport properties that changes the nature of the dissipation to not be determined directly by the low-frequency conductance of the quantum dots, that is otherwise typical [37].

4.1 Single Port Resonator coupled to quantum dot

The system introduced in Paper I, shown in Figure 4.1 consists of a half-wavelength resonator coupled on one end to the input port with a capacitor C_{c} and the output port being a quantum dot with admittance $Y(\omega)$ to ground. The coplanar waveguide is made with Nb using a lift-off method with optical lithography and has a strip width $W = 10$ μm and spacing $S = 5$ μm, with the total length of the strip $l = 9.66$ mm and a finger capacitor coupling the waveguide to the input port. This resonator geometry yields the estimated distributed capacitance $C_{\mathrm{s}} = 178$ pF/m and inductance $L_{\mathrm{s}} = 402$ nH/m, resulting in an impedance $Z_{\mathrm{r}} = \sqrt{L_{\mathrm{s}}/C_{\mathrm{s}}} = 47$ Ω and resonance frequency $f_{\mathrm{r}} = 1/(2l\sqrt{L_{\mathrm{s}}C_{\mathrm{s}}}) = 6.11$ GHz. Also defined in the same lithographic step are all of the DC lines which connect to the quantum dot system. The waveguide

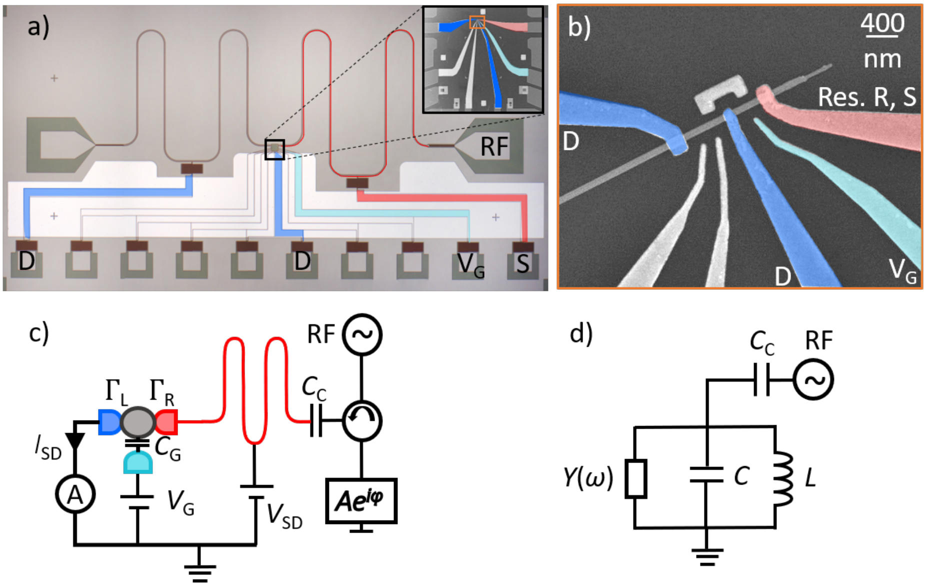

Figure 4.1: The device used in Paper I. **(a)** An optical micrograph of the full device. The resonator line is highlighted in red along with the source DC contact "S" for bias voltage, which connects to E-field node of the resonator. The drain contacts "D" (blue) are connected in the measurement setup to minimize noise from the unused double quantum dot. **(b)** A scanning electron micrograph showing the nanowire and the how the connections are made to it. **(c)** An illustration of the measurement setup. The RF drive is coupled into the resonator via a capacitance C_c, realized with a finger capacitor geometry, and the reflected signal is measured using a heterodyne detection scheme which records the amplitude and phase of the signal. **(d)** The equivalent LC circuit for the fundamental resonator mode which constitutes the basis for the mathematical analysis of the reflected microwave power.

and DC lines terminate at the edge of the 100 μm^2 write field in which the nanowire is deposited manually from a growth chip. The location of the quantum dots in the nanowire are determined using a scanning electron micrograph [101], after which the nanowire shell is etched and the DC contacts are defined with Ti/Au evaporation on an electron beam defined pattern. The device is wire bonded using Al wires and measured in a dilution refridgerator with electronic temperature $T = 50$ mK.

RF measurements are performed using coherent microwave drives where we can set the output frequency and power. The signals from these are fed via RF cabling into the dilution refrigerator where a circulator separates the incoming and reflected signals. The reflected signal is measured using a heterodyne detection scheme, as described in Appendix B with a local oscillator frequency offset $\Delta f = 1$ kHz. As we tune the frequency of the coherent drives, we probe the reflection coefficient as a function of the drive frequency.

Following Eq.(3.35), the coefficient of reflected power can be calculated as

$$R = |r|^2 = 1 - \frac{(\kappa_\mathrm{s} + \kappa_\mathrm{i})\kappa_\mathrm{c}}{(\kappa/2)^2 + (\omega - \omega_\mathrm{r} - \delta\omega_\mathrm{s})^2}, \tag{4.1}$$

where $\kappa = \kappa_\mathrm{s} + \kappa_\mathrm{c} + \kappa_\mathrm{i}$ is the linewidth of the resonance and $\omega_\mathrm{r} = 1/\sqrt{LC}$ is the resonance frequency of the cavity. $\kappa_\mathrm{c} = \frac{Z_0 \omega_\mathrm{r}^2 C_\mathrm{c}^2}{C_\Sigma}$, $\kappa_\mathrm{s} = \mathrm{Re}(Y(\omega))/C_\Sigma$ is the coupling strength of the coupling capacitor and quantum dot respectively, and κ_i is the internal loss dissipation rate. An additional parameter, $\delta\omega_\mathrm{s} = \mathrm{Im}(Y(\omega))/2C_\Sigma$ capturing the dispersive frequency shift caused by the imaginary component of $Y(\omega)$ has also been introduced here. Although the internal losses do not need to be resistive in nature they can be modeled as an additional parallel conductance in the circuit model of Figure 4.1 d).

The internal losses in the resonator can come from a variety of sources, e.g. substrate losses that can be minimized by using highly resistive substrates. Additionally, the resonators exhibit additional losses when connecting it to the other components in our measurement chip. These additional losses can be due to e.g. the use of normal conducting wires to connect the resonator to the nanowire, radiative losses from the endpoints of the resonator acting as an antenna, or leakage through the midpoint contact. In making our devices we attempt to minimize these losses for instance by making the nanowire connections wide, such that the sheet resistance of these lines is minimized, and by shunting all of our DC lines to the ground plane via a large capacitor made with 30 nm thick Al_2O_3, which covers the area shown in white of figure 4.1 a) [102].

A measurement of the reflection coefficient at the resonance frequency of the cavity $R(\omega_\mathrm{r})$ as we sweep V_b and V_G is shown next to the DC current and conductance in Figure 4.2. The clearly visible lines in the reflectometry measurement coincide well with the measured lines in the conductance, indicating that the resonator response aligns with the high-conductance states of the quantum dot.

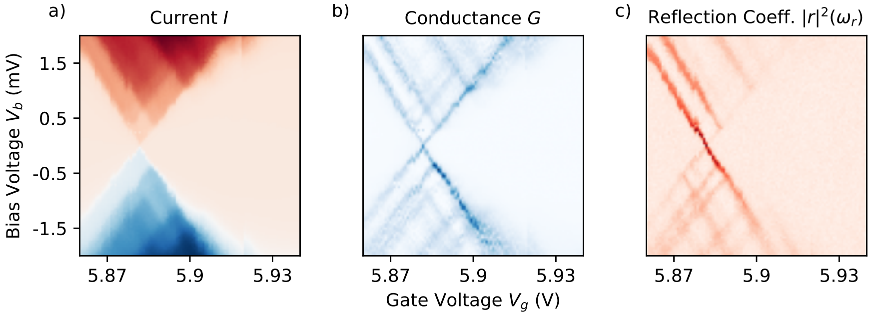

Figure 4.2: Three measurements of a Coulomb diamond, **(a)** shows the current, **(b)** shows the conductance and **(c)** shows the reflection coefficient at resonance frequency

4.2 Measuring the finite frequency admittance

Now, we move towards comparing the zero bias conductance G at DC with the corresponding finite frequency admittance $Y(\omega)$ for the quantum dot. To do this, we set the gate voltage to a value in Coulomb blockade and measure the current as we perform a small sweep of the bias voltage within the linear response regime ($|V_\mathrm{b}| \ll k_\mathrm{B}T$) with the coherent microwave drive turned off. We then set the DC bias to zero, turn on the microwave drive and sweep the frequency across the resonance frequency while measuring the reflected power and repeat at a new gate voltage point, until we have crossed the conductance resonance and entered the Coulomb blockade for the next electron.

At DC, the measurement yields a zero-bias conductance peak, as shown in Figure 2.4 (b), from which the tunnel couplings of the system can be extracted by fitting the data to the Landauer Büttiker theory. From the measurement of the reflection coefficient, shown in Figure 4.3 we can find the resonance frequency, linewidth and amplitude of the resonator as a function of the gate voltage. We first fit the resonator response when the quantum dot is in Coulomb blockade to find κ_i and κ_c, while $\kappa_\mathrm{s} = 0$. Then, keeping κ_i and κ_c constant, we fit the linewidth of the resonator to the remaining gate voltage points. Changes in the linewidth of the resonance are then attributed to the quantum dot coupling, from which the admittance is easily calculated as $\mathrm{Re}(Y(\omega)) = \kappa_\mathrm{s} C$.

When comparing the reflected power in Coulomb blockade with the one when we are resonant with the quantum dot, we see that both the amplitude of the response as well as the linewidth has changed while the resonance frequency is relatively unperturbed. This is in line with an increasing conductance as shown in the discussion about matching in Chapter 3.5.1.

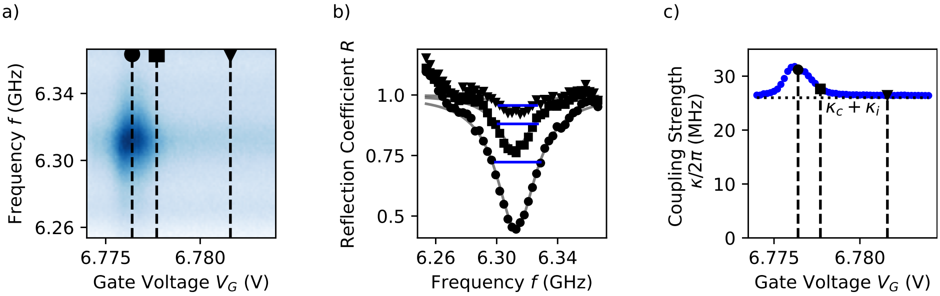

Figure 4.3: **(a)** the measurement of the reflection coefficient as a function of the quantum dot gate voltage and drive frequency. **(b)** Three line cuts in frequency showing the amplitude and linewidth of the resonator response for the three dashed lines in **a**. **(c)** The linewidth of the resonator as a function of the gate voltage, the dotted black line indicates the constant coupling strength of the cavity $\kappa_\mathrm{c} + \kappa_\mathrm{i}$, the changes are due to the quantum dot coupling κ_s

We performed the above measurements for two devices with resonator 1 (2) having $\omega_\mathrm{r}/2\pi = 6.315$ (6.829) GHz, $\kappa_\mathrm{c}/2\pi = 26$ (2.5) MHz, and $\kappa_\mathrm{i}/2\pi = 0.6$ (5.9) MHz, determined from measurements when the quantum dot was tuned to Coulomb blockade. The two quantum dots also vary in their asymmetry, with quantum dot 1 (2) having less (more) asymmetric barriers resulting in different measurement regimes for the two devices, although both devices have $\Gamma_\mathrm{L} < \Gamma_\mathrm{R}$.

In both devices, we make a measurement at two different gate voltage points, tuning the tunnel couplings through the gating. The measurement results for device 1 are presented in Figure 4.4. In panel a), we show the measurement of the DC conductance at a gate voltage $V_{\mathrm{G},0} = 6.78$ V, with a fit produced by Eq. (2.6) yielding the tunnel couplings $\Gamma_\mathrm{L} = 6$ μeV, $\Gamma_\mathrm{R} = 55$ μeV. The measurement of the finite frequency admittance is shown in panel b) and follows closely the DC conductance within measurement tolerance. In this regime, a finite frequency extension to the Landauer-Büttiker theory introduced in Appendix 2 (Eq. A.20) of Paper I is used to produce a prediction of the response based off of the tunnel couplings measured at DC, which is in close agreement with the data.

Figure 4.4 d) - f) shows the same measurement performed at a different gate voltage point $V_{\mathrm{G},0} = 4.72$ V. The DC peak is here thermally broadened, and a fit to the DC data only yields the smaller tunnel coupling. The finite frequency admittance displays a qualitatively different response, showing a factor two difference in admittance between the negative and positive level shift directions, as well as a broadening of $\hbar\omega$ in either direction. The aforementioned finite frequency Landauer Büttiker theory (solid line) now fails to predict the response, although still predicting a broadening due to the photon energy.

This admittance is attributed to a photon assisted tunneling effect illustrated in Figure 4.5 b) where a photon can excite an electron into the dot up to a QD energy level shift of $\epsilon = \hbar\omega$. If we instead shift the energy level of the dot to below the energy of the leads, the photon can now excite an electron out of the quantum dot into the lead. Since any one level of the quantum dot can be filled with two spins, the relative rate of these two processes depend on the filling of the quantum dot. We consider the process which involves the $N = 1 \leftrightarrow N = 2$ transitions. In the case when $-\hbar\omega \leq \varepsilon \leq 0$, the quantum dot has one electron with a specific spin on it, meaning that excitations into the dot can only be achieved with the remaining spin electron. When ε is increased such that $0 \leq \varepsilon \leq \hbar\omega$, both electrons now occupy the dot, meaning that the absorbed photon can excite either of the two electrons out of the dot. Theoretically, the above process is modelled using sequential tunneling approaches, both by considering a time periodic drive coupled to the QD as in Ref. [103], or using P(E) theory which considers the probability of photon absorption events in the cavity [104, 105], yielding the dashed line of Figure 4.4.

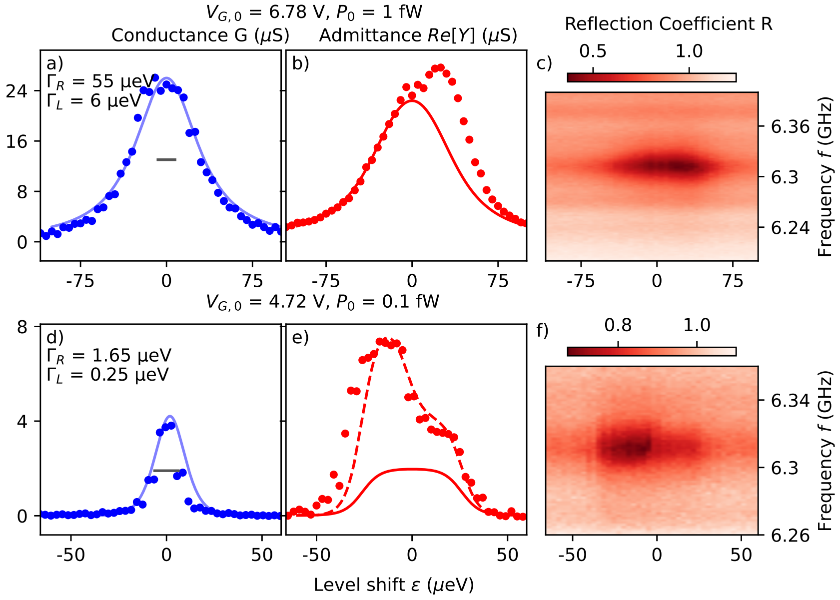

Figure 4.4: The measurement results for device 1. **(a)** The DC conductance as a function of the level shift $\varepsilon = \alpha_G V_G$ (circles) along with a fit to find the tunnel couplings (line, Eq.(2.6)). **(b)** The measured finite frequency admittance at the same gate voltage points as in a) (circles), prediction from finite frequncy Landauer Büttiker theory, Eq. A.20 of Paper I (line). **(c)** The measurement of the reflection coefficient from which the result in b) is found. **(d)-(f)** The same measurement as above for a second transition in which the DC conductance is thermally broadened such that $\hbar\omega > k_B T > \Gamma$. The finite frequency admittance is in this regime broadened due to photon assisted tunneling, as well as showing a factor two difference attributed to spin effects on the quantum dot. The dashed line in **(e)** shows a calculation based on finite frequency sequential tunneling, Eq. A.35 of Paper I, where the larger tunnel coupling in **(d)** has been used as a fitting parameter.

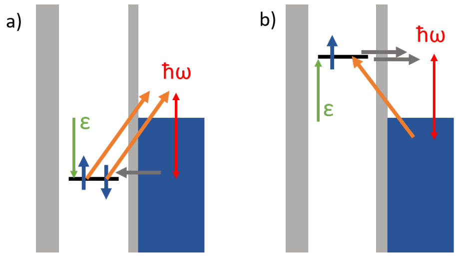

Figure 4.5: An illustration of the process leading to the factor two difference in admittance. We consider the transition where $N = 1 \leftrightarrow 2$, such that for a positive level shift ε as in **(a)**, the orbital is filled, and the photon can excite an electron with either spin up or spin down out of the dot. In **(b)** where the $\varepsilon < 0$, the photon supplies the energy to add the second electron. This process can only happen for electrons with the correct spin, meaning that the process fails half of the time. For transitions going from $N = 0 \leftrightarrow 1$, the two-level structure is thus expected to be mirrored with respect to ε.

An additional measurement performed on device 1 with $V_{G,0} = 4.72$ V is shown in Figure 4.6 where the linewidth of the DC conductance and RF admittance are measured as the input power P_0 is increased. At low input powers, the linewidth approaches those measured in Figure 4.4 d) and e). We see that for high input powers the linewidth is additionally broadened by the amplitude of the voltage oscillation amplitude, as reported in Refs. [11, 106].

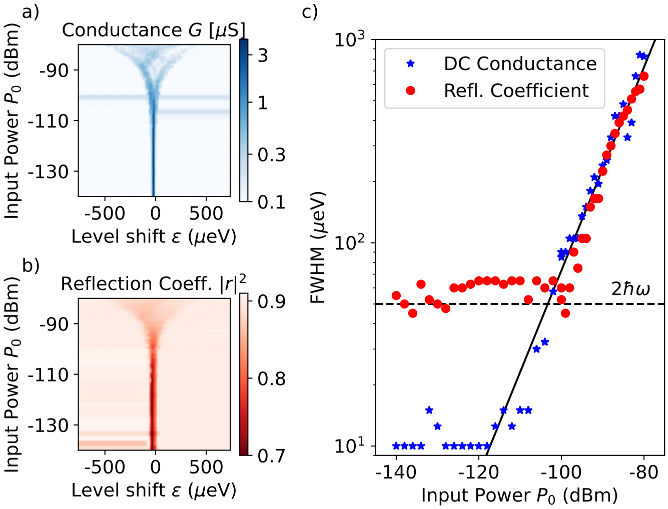

Figure 4.6: Measurement of the quantum dot resonance of Figure 4.4 (d) - (f) as the microwave input power P_0 is increased as the DC conductance$G$ **(a)**, and the RF amplitude **(b)** are measured. Two measurements with different level shift ranges are combined. The horizontal lines appear as a result of extending the edge data to fill the color plot. **(c)** The measured linewidth of the two measured quantities as a function of input power. At low powers they each saturate to the limits discussed in Figure 4.4, while at high power the linewidth is additionally broadened by the voltage amplitude of the cavity.

We see that for high input power P_0 the quantum dot becomes smeared, with a linewidth $\propto P_0^{1/2}$. This arises due to the voltage amplitude of the microwave mode biasing the quantum dot, resulting in additional dissipation [107]. The broadening can be calculated by considering the maximum voltage within the resonator, which is attained as all the stored energy lies across the capacitance

$$E = \hbar\omega_r \langle n \rangle = \frac{1}{2} C_\Sigma V_{\mathrm{MW}}^2. \tag{4.2}$$

Inserting eq. (3.38), we find then that

$$V_{\mathrm{MW}} = \left(\frac{8\kappa_c Z_r \omega_r P_0}{\kappa^2} \right)^{1/2}. \tag{4.3}$$

This result is different by a factor of two from that reported in previous literature [107]

$$V_{\mathrm{MW}} = \left(\frac{4\kappa_c Z_r \omega_r P_0}{\kappa^2} \right)^{1/2}. \tag{4.4}$$

The discrepancy here could possibly be due to the electric energy being split between the two antinodes of the resonator.

A fit of the high-power data to the above equation yields a cavity impedance $Z_\mathrm{r} = 53\ \Omega$, matching the typical value for coplanar waveguide resonators [53].

The measurements for the second device are presented in Figure 4.7. Again, the transparent configuration, with large tunnel couplings shows that finite frequency admittance is explained well by the DC conductance. However, for the second measurement with a lower gate voltage the DC transport is suppressed as the smaller tunnel coupling limits the transport while the finite frequency admittance is two orders of magnitude larger. This can be qualitatively understood by the photon assisted tunneling picture again, where the more transparent barrier allows for tunneling in and out, providing dissipation to the cavity, while the opaque barrier blocks DC transport. However, as the quantum dot is still lifetime broadened, it cannot be treated with sequential tunneling theories, and thus needs more refined theory to quantitatively explain the transport.

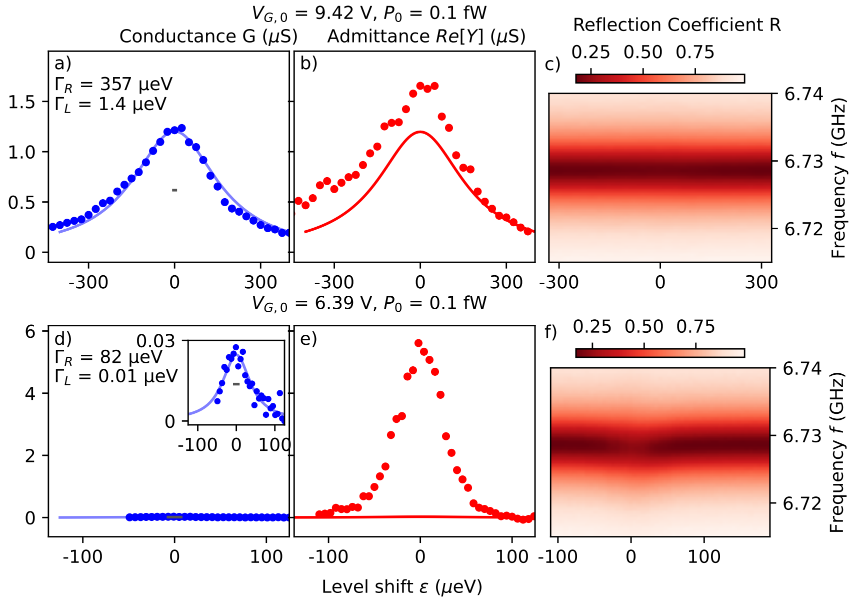

Figure 4.7: The same measurements for Device 2 show again that for $\Gamma > k_\mathrm{B}T, \hbar\omega$ **(a-c)** the finite frequency admittance is well-understood with the DC conductance alone. For the second measurement point **(d-f)**, we have that $\Gamma_\mathrm{L} \ll k_\mathrm{B}T, \hbar\omega$ but $\Gamma_\mathrm{R} > k_\mathrm{B}T, \hbar\omega$. The asymmetry leads to the DC conductance being limited by the smaller tunnel coupling, while the finite frequency admittance is two orders of magnitude larger. The weak response in RF is partially due to lower quantum dot admittance compared to device 1, as well as the resonator internal losses being larger $G_\text{int} \approx 4.5\ \mu$S.

Chapter 5

Nonlinear Resonators based on Josephson Junctions

Until now, we have considered only resonators with a coplanar geometry made from regular superconducting materials. As discussed in Ch. 3, these form a resonance mode due to the geometric inductance L and capacitance C, which depend on the geometry of the coplanar waveguide. Now, we will be considering resonators made from arrays of Josephson junctions (JJs) [108, 109] . These give rise to a kinetic inductance, that arises due to the phase difference of the superconducting state across a weak link, such as a tunnel junction [110, 111]. This allows the creation of high-impedance devices, which enable a strong coupling to quantum mechanical components [54, 112]. This chapter will begin by discussing the Josephson junction as a single component, followed by considering what happens when connecting several junctions in series to form an array.

5.1 Josephson Junctions

In superconductors, the dissipation-less current is arises due to an effective attractive coupling between electrons in the conductor, forming so-called Cooper pairs which move without resistance [113]. These pairs of electrons inhabit states described by the Ginzburg-Landau order parameter $\psi(r) = |\psi(r)|e^{i\phi(r)}$, which is akin to the wavefunction, with $|\psi(r)|^2$ giving the density of cooper pairs, and with $\phi(r)$ the phase of the order parameter.

In a Josephson Junction, illustrated in Fig. 5.1, we consider two superconductors that

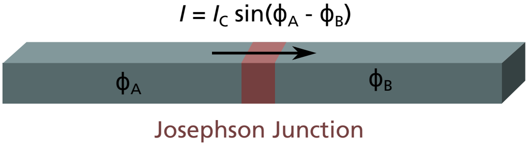

Figure 5.1: An illustration of an superconductir-insulator-superconductor (SIS) Josephson junction. The gray sections are superconductors with the red region being the barrier, making the JJ. Despite the interruption in the superconductor, a supercurrent arising from tunneling of Cooper pairs can be sustained through the junction, depending on the difference in Ginzburg-Landau phase $\phi_A - \phi_\mathrm{B}$ between the two superconductors.

are connected via a weak link such as an insulator [114], metal [115–117], or constriction [118]. The system can be described as two separate superconductors A, B with the corresponding order parameter with phase ϕ_A, ϕ_B. From the Schrödinger equation of this system, one finds the two Josephson equations [119, 120],

$$I(t) = I_\mathrm{C} \sin(\varphi(t)) \tag{5.1}$$

$$V(t) = \frac{\hbar}{2e}\frac{\partial\varphi}{\partial t} = \frac{\Phi_0}{2\pi}\frac{\partial\varphi}{\partial t} \tag{5.2}$$

where I_C is called the *critical current*, $\varphi = \phi_A - \phi_\mathrm{B}$ is the phase difference between the two superconductors and $\Phi_0 = h/2e$ is the magnetic flux quantum. The superconducting junction thus permits a dissipation-free current, which is bounded by the critical current I_C, after which the current transport becomes resistive. Additionally, a voltage across the Josephson junction implies a constant changing phase, resulting in an alternating current with frequency V/Φ_0.

For JJs made with insulating barriers (SIS junctions), the magnitude of the critical current depends on the thickness of the barrier, with more resistive junctions having a lower critical current, obeying the Ambegaokar-Baratoff relation

$$I_\mathrm{C} = \frac{\pi}{2}\frac{\Delta}{R_N} \tag{5.3}$$

where R_N is the resistance of the junction in the normal state, and Δ is the energy gap in the density of states of the superconductor [121]. At the critical current, we thus have a voltage drop across the junction of $U(I_\mathrm{C}) = \frac{\pi}{2}\frac{\Delta}{e}$, as the current now consists of normal electrons being taken across the gap by the applied voltage bias.

We see from the two Josephson equations that a time-varying current will give rise to a voltage, akin to an inductor

$$\frac{\partial I}{\partial t} = I_\mathrm{C}\cos(\varphi(t))\frac{2eV(t)}{\hbar} = \frac{1}{L_J}V(t), \tag{5.4}$$

Where we define the Josephson inductance

$$L_J = \frac{\Phi_0}{2\pi I_C \cos(\varphi)}. \tag{5.5}$$

Unlike a typical inductor, however, this relationship is not due to a buildup of a magnetic field in which the stored energy largely depends on the geometry of the inductor (which is thus called *geometrical* inductance). Rather it is due to the kinetic energy of the Cooper pairs being transmitted through the junction, and is therefore called a *kinetic* inductance.

5.1.1 Superconducting Quantum Interference Devices

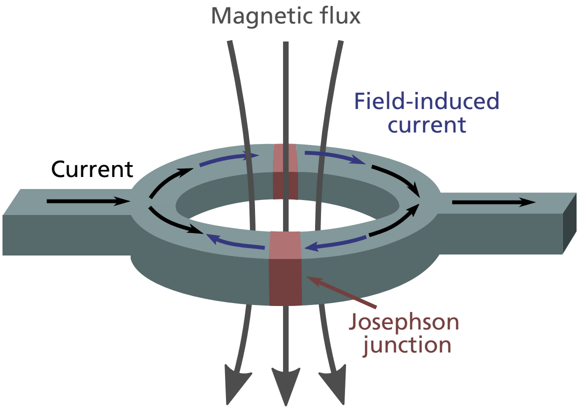

Figure 5.2: A superconducting quantum interference device (SQUID) has two parallel Josephson junctions in a loop geometry. The hole left in the middle permits a magnetic flux which can induce additional currents to flow inside the SQUID, leading to a variation in the phase across the junction.

A Superconducting Quantum Interfering Device, or SQUID is constructed by placing two Josephson Junctions in parallel in a loop geometry, such as in Figure 5.2. We consider such a SQUID with a current I going through it, evenly split between the two junctions. In the presence of a small external magnetic field, a screening current I_B is induced in the SQUID to counteract the external field [122]. As a superconducting loop can permit integer numbers of the flux quanta $\Phi_0 = h/2e$ to be enclosed by the loop, the circulating current switches direction when the external field reaches $\Phi_0/2$ to instead let in a whole flux quanta. Further increases to the field instead decreases the magnitude of the screening current as the external field approaches Φ_0, after which point the cycle repeats. Since the current in the two branches is no longer the same, we have a different phase φ across each junction that depends on the external field Φ[1]

$$\varphi_2 - \varphi_1 = 2\pi n + \frac{2\pi\Phi}{\Phi_0} \tag{5.6}$$

which gives the total current

$$I = 2I_C \cos\left(\frac{\pi\Phi}{\Phi_0}\right)\left(\varphi_1 + \frac{\pi\Phi}{\Phi_0}\right) \tag{5.7}$$

We see thus that the maximum current in the SQUID, found when the second term is maximized, oscillates with the applied magnetic field

$$I_{\max} = 2I_c \left|\cos\left(\frac{\pi\Phi}{\Phi_0}\right)\right|. \tag{5.8}$$

The magnetic field dependent maximum current allows the SQUID to work as an effective magnetometer, and for our interests it allows us to modulate the inductive properties of the SQUID. As we intend to use Josephson junctions to form the inductance of a resonator, this will allow us to tune its resonance frequency.

5.2 JJ-array resonators

As each Josephson Junction contributes an inductance L_j, by making an array of N junctions, the total inductance of the array $L = NL_j$ can be used to form the inductance of a lumped-element resonator, as shown in Fig. 5.3. The capacitance for the resonance mode $C_\Sigma = C_c + C$ is provided by an input coupling capacitance C_c and the stray capacitance C, which together with the inductance defines the resonance frequency $\omega_r = 1/\sqrt{LC_\Sigma}$

Since the kinetic inductance L_j is much greater than the geometric inductance of a regular coplanar waveguide, one can make devices with larger characteristic impedance $Z_r = \sqrt{L/C_\Sigma}$ [55]. Looking back at the equations (3.59), (3.56) for the input coupling κ_c and sensor dissipation κ_s, we note that these scale with a larger impedance. Intuitively, this is explained by the impedance corresponding to the ratio of the voltage oscillations to the current oscillations, with a larger impedance corresponding to larger voltage. As both the coupling capacitance and sensor dissipation couples via electric fields, a larger impedance results in a stronger interaction. The result of this is that the linewidth of the resonator is increased, leading to a larger bandwidth for the resonator, allowing faster measurements.

---

[1] We have here assumed that the self-inductance L of the SQUID is sufficiently small that $I_B L \ll \Phi$ which would otherwise need to be taken into account.

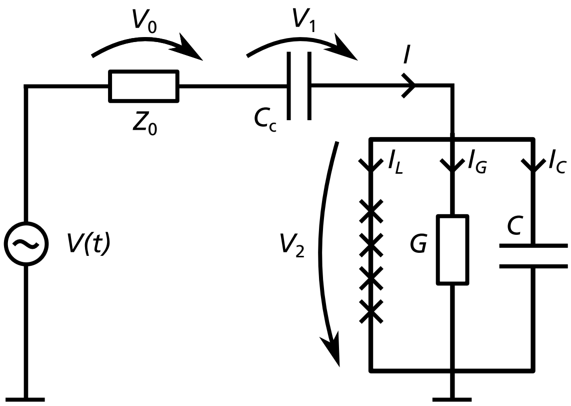

Figure 5.3: Circuit diagram of the JJ-array oscillator with input voltage signal $V(t)$ through a transmission line with characteristic impedance Z_0. The resonator has a coupling capacitance C_c, self-capacitance C and conductance G, the inductance arises from the array of Josephson junctions.

5.2.1 Hamiltonian solution to the nonlinear resonator

Although the inductance of the Josephson junction should allow us to make a resonator, the nature of this inductance is not the same as that for a regular coil. Notably, we have a phase-dependent term which introduces a non-linearity that affects the inductance as the phase across the junction changes. This can occur as we increase the amplitude of the oscillations within the resonator. In order to derive the effects of this non-linear inductance, we will now construct the Hamiltonian of the JJ-array resonator, beginning by considering the system with only a single Josephson junction. This system is a so-called Cooper pair box (CPB) [123, 124], which is considered to be a superconducting island coupled to the environment via a single Josephson junction. Such a CPB has a charging energy given by its self-capacitance C_Σ

$$E_\mathrm{C} = \frac{q^2}{2C_\Sigma} \tag{5.9}$$

which is the required energy to add a single particle of charge q to the island. As the charge of n Cooper pairs is $Q = n\,2e$, we find that the corresponding energy stored on the island is

$$U = 4E_\mathrm{C}n^2 \tag{5.10}$$

Next, in order to calculate the energy of the supercurrent flowing through the Josephson junction, we consider the energy difference ΔE as the phase difference φ changes with time. This energy difference is given by the time-integral of the work done to the junction

$$\Delta E = \int_{t_1}^{t_2} IV dt = \int_{t_1}^{t_2} I_\mathrm{C} \sin(\varphi(t)) V dt \tag{5.11}$$

using now the second Josephson relation, we can make a variable transformation to instead integrate over the phase difference φ.

$$\Delta E = \frac{\hbar}{2e} \int_{\varphi_1}^{\varphi_2} I_\mathrm{C} \sin(\varphi) d\varphi = -\frac{\hbar}{2e} I_\mathrm{C} (\cos(\varphi_2) - \cos(\varphi_1)) = -E_J \Delta \cos(\varphi) \tag{5.12}$$

Where E_J is the Josephson energy

$$E_J = \frac{\hbar I_\mathrm{C}}{2e} = L_J I_\mathrm{C}^2. \tag{5.13}$$

Finally, we use the second Josephson relation, along with the definition of the node flux ϕ, to realize that the phase difference can be expressed as

$$\varphi = 2\pi \frac{\phi}{\Phi_0} \tag{5.14}$$

Following the same arguments as in Chapter 3, we can now construct the Hamiltonian of a single Josephson junction

$$H = \frac{1}{2C} Q^2 - E_J \cos\left(2\pi \frac{\phi}{\Phi_0}\right) \tag{5.15}$$

We note that for small values of ϕ, the cosine term varies like ϕ^2, such that the Hamiltonian is equivalent to that of the linear harmonic oscillator. However, for large ϕ, i.e. large amplitudes of the resonant mode, the lowest-order approximation is no longer valid, as we will have to take into account higher order terms as well. In this section, we evaluate the next order terms to find a Hamiltonian describing the resonance mode up to the first nonlinear term.

We begin by Taylor expanding the cosine term to the first anharmonic term

$$E_J \cos 2\pi \frac{\phi}{\Phi_0} = E_J \left(1 - \frac{1}{2}\left(2\pi \frac{\phi}{\Phi_0}\right)^2 + \frac{1}{24}\left(2\pi \frac{\phi}{\Phi_0}\right)^4 + \mathcal{O}(\phi^6)\right), \tag{5.16}$$

From here, we ignore the constant offset term, and note that the Hamiltonian is then

$$H = \frac{1}{2C} Q^2 + \frac{1}{2L} \phi^2 - E_J \left(\frac{1}{24}\left(2\pi \frac{\phi}{\Phi_0}\right)^4 + \mathcal{O}(\phi^6)\right). \tag{5.17}$$

The first two terms here are the same that we find for a linear resonator, leaving the third term to be evaluated. We do this by rewriting the phase $\hat{\phi}$ in terms of the ladder operators

$$\hat{\phi} = \sqrt{\frac{\hbar Z}{2}} \left(\hat{a} + \hat{a}^\dagger \right) \tag{5.18}$$

which obey the commutation relation

$$\left[\hat{a}, \hat{a}^\dagger \right] = \hat{a}\hat{a}^\dagger - \hat{a}^\dagger \hat{a} = 1 \Rightarrow \hat{a}\hat{a}^\dagger = 1 + \hat{a}^\dagger \hat{a}. \tag{5.19}$$

We then focus on the quartic term

$$\begin{aligned}
&\frac{4}{\hbar^2 Z^2}\hat{\phi}^4 = \left(\hat{a} + \hat{a}^\dagger \right)^4 = \\
&\left(\hat{a}^2 + \hat{a}\hat{a}^\dagger + \hat{a}^\dagger \hat{a} + \hat{a}^{\dagger 2} \right)^2 = \\
&= \left(\hat{a}\hat{a}\hat{a}\hat{a} + \hat{a}\hat{a}\hat{a}\hat{a}^\dagger + \hat{a}\hat{a}\hat{a}^\dagger \hat{a} + \hat{a}\hat{a}\hat{a}^\dagger \hat{a}^\dagger \right) \\
&+ \left(\hat{a}\hat{a}^\dagger \hat{a}\hat{a} + \hat{a}\hat{a}^\dagger \hat{a}\hat{a}^\dagger + \hat{a}\hat{a}^\dagger \hat{a}^\dagger \hat{a} + \hat{a}\hat{a}^\dagger \hat{a}^\dagger \hat{a}^\dagger \right) \\
&+ \left(\hat{a}^\dagger \hat{a}\hat{a}\hat{a} + \hat{a}^\dagger \hat{a}\hat{a}\hat{a}^\dagger + \hat{a}^\dagger \hat{a}\hat{a}^\dagger \hat{a} + \hat{a}^\dagger \hat{a}\hat{a}^\dagger \hat{a}^\dagger \right) \\
&+ \left(\hat{a}^\dagger \hat{a}^\dagger \hat{a}\hat{a} + \hat{a}^\dagger \hat{a}^\dagger \hat{a}\hat{a}^\dagger + \hat{a}^\dagger \hat{a}^\dagger \hat{a}^\dagger \hat{a} + \hat{a}^\dagger \hat{a}^\dagger \hat{a}^\dagger \hat{a}^\dagger \right)
\end{aligned}$$

We enforce energy conservation to drop all terms which don't preserve the photon number in the cavity, and then utilize the commutation relation to swap terms

$$\begin{aligned}
\left(\hat{a} + \hat{a}^\dagger \right)^4 &\approx \hat{a}\hat{a}\hat{a}^\dagger \hat{a}^\dagger + \hat{a}\hat{a}^\dagger \hat{a}\hat{a}^\dagger + \hat{a}\hat{a}^\dagger \hat{a}^\dagger \hat{a} + \hat{a}^\dagger \hat{a}\hat{a}\hat{a}^\dagger + \hat{a}^\dagger \hat{a}\hat{a}^\dagger \hat{a} + \hat{a}^\dagger \hat{a}^\dagger \hat{a}\hat{a} \\
&= 6\hat{a}^\dagger \hat{a}^\dagger \hat{a}\hat{a} + 12\hat{a}^\dagger \hat{a} + 3
\end{aligned}$$

We note three terms, first we have the nonlinear term which increases proportional to n^2, describing the lowest-order nonlinear dynamics of the resonator. Second, we have a term proportional to n of the same form as in a regular Harmonic oscillator. This term will result in a correction to the bare resonator frequency, with magnitude depending on the ratio of $E_\mathrm{C}/E_\mathrm{J}$. Assuming that the resonator is closer to the transmon-regime than the charge-qubit regime however, we are free to neglect this correction. Third, we have an offset in the total energy of the junction, which we are also free to ignore. With these considerations, we insert the above into the Hamiltonian

$$H \approx \hbar\omega_\mathrm{r} \hat{a}^\dagger \hat{a} - E_J \left(\frac{2\pi^4}{3\Phi_0^4} \frac{\hbar^2 Z^2}{4} \left(6\hat{a}^\dagger \hat{a}^\dagger \hat{a}\hat{a} \right) \right) = \hbar\omega_\mathrm{r} \hat{a}^\dagger \hat{a} - \frac{E_\mathrm{C}}{2} \hat{a}^\dagger \hat{a}^\dagger \hat{a}\hat{a}. \tag{5.20}$$

Here, we note that the prefactor corresponds to the Kerr nonlinearity with coefficient $E_\mathrm{K} = -E_\mathrm{C}$.

In a JJ-array resonator, we have a series of N such Josepshon junctions. This means that the voltage in the array is divided evenly across the N junctions. Therefore, in order to reach the same voltage amplitude across a single junction, the total voltage amplitude in the resonator has to be increased by a factor of N Since the number of photons in the cavity is proportional to the stored energy which in turn is proportional to V^2, the required energy in the cavity to reach the same non-linearity is proportional to $\frac{1}{N^2}$. For the N-junction resonator, the Hamiltonian is thus

$$H = \hbar\omega_\mathrm{r}\hat{a}^\dagger\hat{a} - \frac{E_\mathrm{C}}{2N^2}\hat{a}^\dagger\hat{a}^\dagger\hat{a}\hat{a}. \tag{5.21}$$

5.2.1.1 Frequency Shift

Just as a linear Harmonic oscillator, the above Hamiltonian has eigenstates corresponding to the number of photons n, with eigenenergies

$$E_n = \hbar\omega_\mathrm{r}n^2 - E_\mathrm{C}(n^2 - n). \tag{5.22}$$

We consider now the energy for the n^th photon

$$E_n - E_{n-1} = E_\mathrm{K}(n-1), \tag{5.23}$$

and find that as $E_\mathrm{K} < 0$, the resonator energy decreases with the number of photons. This means that the resonance frequency shifts away from the low-power result by

$$\omega_K = \frac{E_\mathrm{K}}{\hbar}(n-1) \tag{5.24}$$

towards lower frequencies[2]. Assuming that $n \gg 1$ and inserting Eq. (3.38) for the photon number, we find

$$\frac{\omega_\mathrm{K}}{\omega_\mathrm{r}} = \frac{E_\mathrm{K}}{\hbar\omega_\mathrm{r}}n = \frac{4\pi Z_\mathrm{r}\kappa_\mathrm{c}}{R_Q N^2\kappa^2}\frac{P_0}{\hbar\omega_\mathrm{r}}, \tag{5.25}$$

Furthermore, we find that for a specific frequency shift ω_r there is a set photon number

$$n = \frac{N^2}{\pi}\frac{R_Q}{Z_\mathrm{r}}\frac{-\omega_\mathrm{r}}{\omega_\mathrm{r}} \tag{5.26}$$

depending on the number of junctions in series N and the characteristic impedance Z_r of the resonator.

---

[2] As the frequency of the resonator is decreasing with increasing power, we say that the resonator is softening. In the opposite case, we would say that the resonator was hardening if the frequency increased.

5.2.2 Numerical Solution to the Nonlinear Resonator

With the Hamiltonian solution method we have managed to show that the resonator reduces its resonance frequency as the input power is increased. However, we have no knowledge of the frequency response of the resonator. Calculating this would require to now add a coupling to an environment and solve the Hamiltonian of this shared system with an interaction term. However, this is a far too complicated problem for this thesis. Instead, we will now solve the full system numerically by considering the reflection coefficient of the circuit shown in Fig. 5.3. For this, we will need to calculate the impedance of the resonator $Z = (V_1 + V_2)/I$.

We begin by assuming a sinusoidal input tone

$$V(t) = V_0 \sin(\omega t) = \frac{V_0}{2}\left(e^{i\omega t} - e^{-i\omega t}\right), \tag{5.27}$$

corresponding to an input power $P_0 = (V_0/2\sqrt{2})^2/Z_0$, where the additional factor 2 is due to the voltage division across the input impedance. Now, we consider Kirchhoff's current continuity law for the circuit which gives

$$V_Z Z_0 = C_c \frac{\partial V_1}{\partial t} = C\frac{\partial V_2}{\partial t} + V_2 G + I_C \sin(\varphi), \tag{5.28}$$

Recalling the Josephson equations (Eq (5.1) and Eq (5.2)), we see that we can write the current I_L and the voltage V_2 in terms of the Josephson phase φ as

$$\begin{cases} I_L(t) = I_C \sin(\varphi(t)) \\ V_2 = \frac{\hbar N}{4e\pi}\frac{\partial\varphi}{\partial t} \end{cases}, \tag{5.29}$$

which upon insertion into Eq (5.28) gives

$$C\frac{\partial V_1}{\partial t} = C\frac{\hbar N}{2e}\frac{\partial^2\varphi}{\partial t^2} + \frac{\hbar N}{2e}\frac{\partial\varphi}{\partial t}G + I_C\sin(\varphi). \tag{5.30}$$

Now, applying the second of Kirchhoff's laws, we demand that the voltages in the circuit add up to the input voltage

$$\begin{aligned}\frac{\partial V}{\partial t} =& \frac{\partial V_Z}{\partial t} + \frac{\partial V_1}{\partial t} + \frac{\partial V_2}{\partial t} = Z_0\frac{\partial I}{\partial t} + \frac{\partial V_1}{\partial t} + \frac{\partial V_2}{\partial t} \\ =& Z_0 I_C\cos(\varphi)\frac{\partial\varphi}{\partial t} + Z_0 C\frac{\hbar N}{2e}\frac{\partial^3\varphi}{\partial t^3} + Z_0 G\frac{\hbar N}{2e}\frac{\partial^2\varphi}{\partial t^2} + \frac{\partial V_1}{\partial t} + \frac{\hbar N}{2e}\frac{\partial^2\varphi}{\partial t^2}.\end{aligned}$$

Using Eq. (5.30) to substitute the expression for V_1, we find

$$\begin{aligned} C_\mathrm{c}\frac{\partial V}{\partial t} =& C_\mathrm{c}\left(Z_0 I_\mathrm{C}\cos(\varphi)\frac{\partial\varphi}{\partial t} + Z_0 C\frac{\hbar N}{2e}\frac{\partial^3\varphi}{\partial t^3} + (1+Z_0 G)\frac{\hbar N}{2e}\frac{\partial^2\varphi}{\partial t^2}\right) \\ &+ C\frac{\hbar N}{2e}\frac{\partial^2\varphi}{\partial t^2} + G\frac{\hbar N}{2e}\frac{\partial\varphi}{\partial t} + I_\mathrm{C}\sin(\varphi) \\ =& I_\mathrm{C}\sin(\varphi) + \left(Z_0 I_\mathrm{C} C_\mathrm{c}\cos(\varphi) + G\frac{\hbar N}{2e}\right)\frac{\partial\varphi}{\partial t} \\ &+ \left((C + C_\mathrm{c}(1+Z_0 G))\frac{\hbar N}{2e}\right)\frac{\partial^2\varphi}{\partial t^2} + \left(Z_0 C C_\mathrm{c}\frac{\hbar N}{2e}\right)\frac{\partial^3\varphi}{\partial t^3}. \end{aligned}$$

Next, we make the assumption[3] that $Z_0 G \ll 1$, define $C_\Sigma = C + C_\mathrm{c}$ and rewrite the equation as

$$\begin{aligned} \frac{\partial^2\varphi}{\partial t^2} + \frac{2e}{\hbar N}\frac{I_\mathrm{C}}{C_\Sigma}\sin(\varphi) + \left(\frac{G}{C_\Sigma} + \frac{2e}{\hbar N}\frac{Z_0 I_\mathrm{C} C_\mathrm{c}}{C_\Sigma}\cos(\varphi)\right)\frac{\partial\varphi}{\partial t} \\ + \left(\frac{Z_0 C C_\mathrm{c}}{C_\Sigma}\right)\frac{\partial^3\varphi}{\partial t} = \frac{C_\mathrm{c}}{C_\Sigma}\frac{2e}{\hbar N}\frac{\partial V}{\partial t}. \end{aligned} \tag{5.31}$$

Since the system receives a sinusoidal input signal, we make the ansatz that the phase takes on an oscillating solution $\varphi(t) = \varphi_1 e^{i\omega t} + \varphi_1^* e^{-i\omega t}$. This lets us rewrite

$$\frac{\partial^3\varphi}{\partial t^3} = -\omega^2\frac{\partial\varphi}{\partial t}$$

and by substituting in the Josephson inductance for the array $L = \frac{\hbar N}{2eI_\mathrm{C}}$, and defining the resonance frequency $\omega_\mathrm{r} = 1/\sqrt{(LC_\Sigma)}$ we arrive at the equation of motion for the phase.

$$\begin{aligned} \frac{\partial^2\varphi}{\partial t^2} + \left(\frac{G}{C_\Sigma} + \frac{Z_0\omega_\mathrm{r}^2 C_\mathrm{c}^2}{C_\Sigma}\left(\frac{C_\Sigma}{C_\mathrm{c}}\cos(\varphi) - \frac{\omega^2}{\omega_\mathrm{r}^2}\frac{C_\Sigma}{C_\mathrm{c}} - \frac{\omega^2}{\omega_\mathrm{r}^2}\right)\right)\frac{\partial\varphi}{\partial t} \\ + \omega_\mathrm{r}^2\sin(\varphi) = \frac{2e}{\hbar N}\frac{C_\mathrm{c}}{C_\Sigma}\frac{\partial V}{\partial t} \end{aligned} \tag{5.32}$$

In order to solve the above system, we approximate the sinusoidal term in the coordinate position $\sin(\varphi) = \varphi - \varphi^3/6$, while ignoring the nonlinearity in the damping

---

[3] The input impedance Z_0 is typically set to $50\ \Omega$, meaning that a conductance of $G > 200\ \mu S$ would be needed to make an error in the 2nd decimal. Seeing as this already exceeds the conductance quantum $G_0 \approx 77.5\ \mu S$ by more than a factor of 2. Assuming that the circuit conductance arises from a single-channel sensor such as a QD or QPC which does not exceed this conductance quantum, we are therefore very safe in this assumption.

term[4] $\cos(\varphi) = 1$.

$$\frac{\partial^2 \varphi}{\partial t^2} + (\kappa_i + \kappa_{\mathrm{c}}) \frac{\partial \varphi}{\partial t} + \omega_{\mathrm{r}}^2 \varphi - \frac{\omega_{\mathrm{r}}^2}{6} \varphi^3 = \frac{2e}{\hbar N} \frac{C_{\mathrm{c}}}{C_\Sigma} \omega V_0 \cos(\omega t) \tag{5.33}$$

where $\kappa_{\mathrm{i}} = G/C_\Sigma$ is the internal losses and $\kappa_{\mathrm{c}} = \varepsilon(\omega) Z_0 \omega_{\mathrm{r}}^2 C_{\mathrm{c}}^2 / C_\Sigma$ the external coupling strength as found in Ch. 3 with an additional correction factor $\varepsilon(\omega)$, which is near unity as $\omega \approx \omega_{\mathrm{r}}$.

Written on this form, the equation of motion is the duffing equation

$$\ddot{\varphi} + \kappa \dot{\varphi} + \alpha \varphi + \beta \varphi^3 = \gamma \cos(\omega t) \tag{5.34}$$

with system parameters $\kappa = \kappa_i + \kappa_{\mathrm{c}}$, $\alpha = \omega_{\mathrm{r}}^2$, $\beta = -\omega_{\mathrm{r}}^2/6$, $\gamma = (2eC_{\mathrm{c}}\omega/\hbar N C_\Sigma)V_0$.

We solve this system using the harmonic balance method, where we insert our ansatz from above into the equation

$$\begin{aligned} &- \omega^2 \left(\varphi_1 e^{i\omega t} + \varphi_1^* e^{-i\omega t}\right) + i\kappa \left(\varphi_1 \omega e^{i\omega t} - \varphi_1^* \omega e^{-i\omega t}\right) \\ &\qquad + \alpha \left(\varphi_1 e^{i\omega t} + \varphi_1^* e^{-i\omega t}\right) + \beta \left(\varphi_1 e^{i\omega t} + \varphi_1^* e^{-i\omega t}\right)^3 = \gamma \cos(\omega t). \end{aligned}$$

We evaluate the cubic expression and discard terms of higher harmonics, then rearrange the expression to arrive at

$$\begin{aligned} &(-\varphi_1 \omega^2 + i\kappa\omega\varphi_1 + \alpha\varphi_1 + 3\beta|\varphi_1|^2\varphi_1 - \gamma/2)e^{i\omega t} \\ &\qquad + (-\varphi_1 \omega^2 - i\kappa\omega\varphi_1 + \alpha\varphi_1 + 3\beta|\varphi_1|^2\varphi_1 - \gamma/2)e^{-i\omega t} = 0. \end{aligned} \tag{5.35}$$

As the second term is simply the complex conjugate of the first, the above condition is non-trivially true only if

$$\varphi_1 = \frac{\gamma/2}{\alpha - \omega^2 + i\kappa\omega + 3\beta|\varphi_1|^2} \tag{5.36}$$

which in terms of the system parameters is

$$\varphi_1 = \frac{\frac{e}{\hbar N} \frac{C_{\mathrm{c}}}{C_\Sigma} \omega V_0}{\omega_{\mathrm{r}}^2 - \omega^2 + i\kappa\omega + \frac{\omega_{\mathrm{r}}^2}{2}|\varphi_1|^2}. \tag{5.37}$$

---

[4] This assumption may not seem initially justified, as we are already including a higher-order term in the coordinate position. However, this term belongs to the damping coefficient of the resonator, and is thus responsible for the linewidth of the resonator, not for the frequency evolution of the mode, making this term less important to preserve if one is interested in the frequency shift of the resonator as we are.

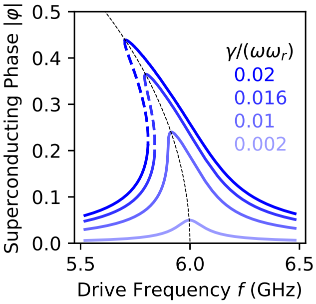

Figure 5.4: Solutions to Eq. (5.36) showing the Josephson phase φ as a function of the drive frequency ω with the system parameters $\alpha = \omega_\mathrm{r}^2$, $\beta = -\omega_\mathrm{r}^2/6$, $\kappa = 0.02\omega_\mathrm{r}$, $\gamma/(\omega\omega_\mathrm{r}) = 0.02, 0.016, 0.01$, and 0.002 counting from the top. Unstable solutions are shown with a dashed line of the same color. The black dotted line shows the backbone curve $\varphi_{bb} = \sqrt{2(1-(\omega/\omega_\mathrm{r})^2}$ of the response.

This self-consistent equation can be solved with a numerical iterative method in order to find stable solutions of φ_1. Figure 5.4 shows the magnitude of the phase $|\varphi|$ as a function of the frequency at three different drive amplitudes γ. We see that at low powers (blue curve) the phase has a response centered around the resonance frequency ω_r, but that for larger drive amplitudes γ (red line) the response tends towards lower frequencies, climbing along the backbone curve indicated by the black dashed line

$$\varphi_{bb} = \sqrt{\frac{\omega^2 - \alpha}{3\beta}} = \sqrt{2(1 - (\frac{\omega}{\omega_\mathrm{r}})^2)} \tag{5.38}$$

where the second equality holds for our system parameters. After some critical input amplitude, there begins to exist multiple solutions to Eq (5.37), resulting in a bifurcation of the resonance mode, which we will discuss in more in detail in the next section.

Now that we know the phase Josephson phase φ, we can calculate the impedance of the junction array We begin by considering the voltage across the array

$$V_2 = \frac{\hbar N}{2e}\frac{\partial\varphi}{\partial t} = \frac{\hbar N}{2e} i\omega\left(\varphi_1 e^{i\omega t} - \varphi_1^* e^{-i\omega t}\right) \tag{5.39}$$

and the current through the array I as

$$I = C_\mathrm{c}\frac{\partial V_1}{\partial t} = C_\mathrm{c}\frac{\partial}{\partial t}\left(V(t) - V_2 - V_\mathrm{Z}\right) = C_\mathrm{c}\frac{\partial}{\partial t}\left(V(t) - V_2 - Z_0 I\right) \tag{5.40}$$

again, assuming that the current is of a sinusoidal form

$$I = I_1 e^{i\omega t} + I_1^* e^{-i\omega t}$$

we rearrange the expression into

$$\begin{aligned}&\left(i\omega C_\mathrm{c}\frac{V_0}{2}+\frac{\hbar N}{2e}C_\mathrm{c}\omega^2\varphi_1-(1+i\omega C_\mathrm{c}Z_0)I_1\right)e^{i\omega t}\\&+\left(-i\omega C_\mathrm{c}\frac{V_0}{2}+\frac{\hbar N}{2e}C_\mathrm{c}\omega^2\varphi_1-(1-i\omega C_\mathrm{c}Z_0)I_1\right)e^{-i\omega t}=0\end{aligned}$$

which, following the same argumentation as for the superconducting phase above, results in

$$I_1=\frac{i\omega C_\mathrm{c}\frac{V_0}{2}+\frac{\hbar N}{2e}C_\mathrm{c}\omega^2\varphi_1}{1+i\omega C_\mathrm{c}Z_0}. \tag{5.41}$$

Finally, we can calculate the impedance of the resonator as

$$Z=\frac{V_1+V_2}{I_1}=\frac{\frac{V_0}{2}-\frac{\hbar N}{2e}C_\mathrm{c}Z_0\omega^2\varphi_1}{i\omega C_\mathrm{c}\frac{V_0}{2}+\frac{\hbar N}{2e}C_\mathrm{c}\omega^2\varphi_1}. \tag{5.42}$$

5.2.3 Reflection response

With the results from Eqs. (5.37) and(5.42) we can numerically calculate the reflection response of the resonator as

$$r=\frac{Z-Z_0}{Z+Z_0}. \tag{5.43}$$

In this section, we will study the outcome of the numerical calculations in order to understand how the nonlinearities impact the resonator with a large input amplitude V_0.

We begin by verifying that the low-frequency response is retained. Figure 5.5 shows the resonator response calculated with the linear reflection coefficient of Eq. (3.35) as well as with the numerical method. we see that the numerical method agrees quite well with that of the linear resonator, although there is a very slight deviation in the imaginary component.

Next, Fig. 5.6 (a) shows the frequency response of the resonator as the input amplitude $\gamma/(\omega\omega_\mathrm{r})$ is increased. Here we see the same behavior of the reflection coefficient as we did for the superconducting phase of Fig. 5.4, with the frequency of the resonator decreasing as the input power is increased. As the frequency shift of the resonator exceeds

$$\Delta\omega_\mathrm{r}=-\frac{3}{4}\kappa \tag{5.44}$$

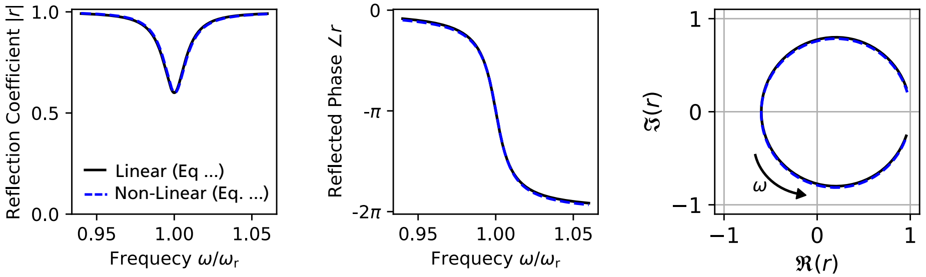

Figure 5.5: The reflection response of the resonator as the drive frequency is varied. The black lines show the low-power solution, Eq (3.35). The blue dashed lines show the result from the numerical calculations, Eq. (5.42) with $P_0 = 1$ aW. **(a)**: The amplitude reflection coefficient, $|r|$. **(b)**: The phase of the reflected signal $\angle r$. **(c)**: The real- and imaginary components of the solution.

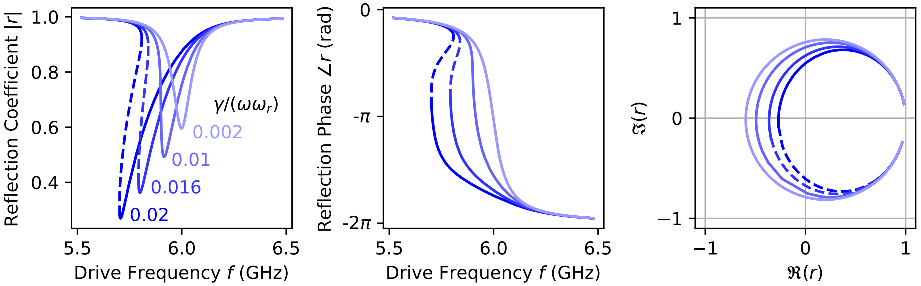

Figure 5.6: The amplitude **(a)**, phase **(b)** and full complex response **(c)** of the reflected signal in the nonlinear resonator at increasing input amplitudes $\gamma/(\omega\omega_\mathrm{r})$ with $\kappa = 0.02\omega_\mathrm{r}$.

the bifurcation of the resonator begins [57,125,126], after which three solutions exist to the duffing equation. One of the three solutions is unstable, and is indicated with the dashed line. A measurement of the reflection coefficient of the resonator will result in one of the two remaining stable solutions, depending on the sweep direction and the amount of noise acting on the system.

In Fig. 5.7 we consider the $\gamma/(\omega\omega_\mathrm{r}) = 0.02$ case from above, showing the two stable solutions. For a system with no external noise perturbing the resonator, the resonator will only switch at the jump-up and jump-down frequencies, indicated by solid markers [127]. With external perturbations, however, the resonator can switch spontaneously between the two states with increasing rate as the frequency approaches the jump-up/jump-down frequency [109]. If the measurement time exceeds the switching time, the measurement will thus result in an average of the two solutions, weighted by the corresponding switching rates.

Figure 5.8 shows the (high-amplitude solution) reflected amplitude a function of the input frequency f and power P_0, with the dashed line indicating the resonance fre-

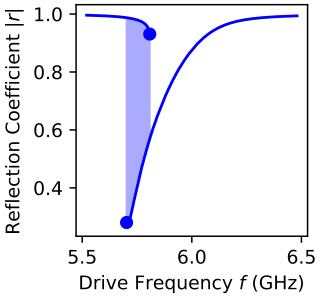

Figure 5.7: The two stable solutions in the nonlinear regime indicated by the solid blue lines. The switching points (with no external perturbation) are indicated with the dots, while the blue shaded region indicates the region in which switching can happen if external perturbations are present.

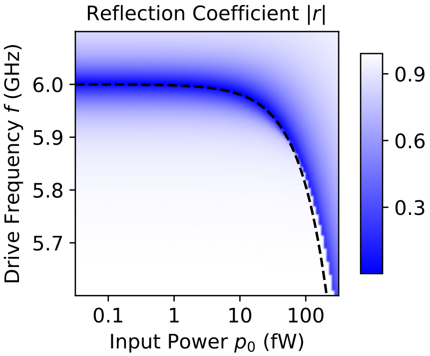

Figure 5.8: The resonator amplitude $|r|$ as a function of the drive power P_0 and frequency f. The dashed line indicates the frequency shift as calculated from Eq (5.25).

quency shift, as predicted by the Hamiltonian solution in ch. 5.2.1.1. We note that the two methods for calculating the response of the resonator agree well with each other for reasonable input amplitudes, where the resonance frequency only shifts on the order of a few linewidths[5].

---

[5] For very large input powers, the two methods do not agree. The Hamiltonian method predicts a frequency shift proportional to the square of the voltage, whereas the Duffing solution gives the solution as following a circular arc. This limit, however, is likely exceeding the approximation that only the first nonlinear term is relevant.

5.2.4 Onset of Bifurcation

As the aim of using a resonator to read out a charge sensor is to perform time-resolved measurements, the switching dynamics of the nonlinear resonator would interfere with any such measurements. However, in order to make the readout signal larger we will want to drive the resonator at a high input power P_0. It is therefore useful to consider the input power P_0 at which the bifurcation is onset, as this will set a limit to the device performance.

The onset of bifurcation occurs first for the low-frequency tail of the response at $\omega_\mathrm{r} = -\sqrt{(3/4)}\kappa$ [57], and reaches the peak at $\omega_\mathrm{r} = -\kappa$. From Eq. (5.26) we thus find that the number of photons in the resonator as the peak enters bifurcation is

$$n = \frac{N^2}{\pi}\frac{R_Q}{Z_\mathrm{r}}\frac{\kappa}{\omega_\mathrm{r}} \tag{5.45}$$

which, upon insertion into Eq (3.38) yields the critical power

$$P_\mathrm{c} = \frac{N^2\Phi_0^2\kappa^3}{2\pi^2 Z_\mathrm{r}\kappa_\mathrm{c}} \tag{5.46}$$

where the resonator becomes bifurcated at the peak.

Chapter 6

Dissipation in Nonlinear Resonators

Now that the response of a nonlinear resonator is well-understood, we will proceed with adding dissipation to the system by coupling such a resonator to a quantum dot. This chapter will present the experimental measurements on a device where a SQUID-array resonator was coupled to a QD charge sensor probing a DQD. We will begin in Sec. 6.1 by presenting the device geometry, and proceed with the measurements forming the basis for Paper II in Sec. 6.2. Finally in Sec. 6.3 and 6.4 we will consider the prospects and limitations to using this type of resonator for the charge readout.

6.1 Device Geometry

Figure 6.1 shows scanning electron micrographs of the measured device. The nonlinear resonator is made from an array of N=13 SQUIDs in series (blue inset) coupled to the input/output port via a capacitor on one end forming the antinode of oscillations, and directly connected to ground on the other end. The SQUIDs are formed via double angle shadow evaporation [128–130] and have a resistance of $R_{300\ \mathrm{K}} = 1.25\ \mathrm{k}\Omega$ per SQUID as measured at room temperature. The central loop for the SQUIDs in this resonator array is formed by a rectangular area of size 4.5 $\mu\mathrm{m}^2$. The antinode of the resonator is additionally connected to the source of a quantum dot embedded in a nanowire (red inset), with the drain defined by an ohmic contact. This drain contact is shared with a DQD residing in the other half of the nanowire. A second resonator

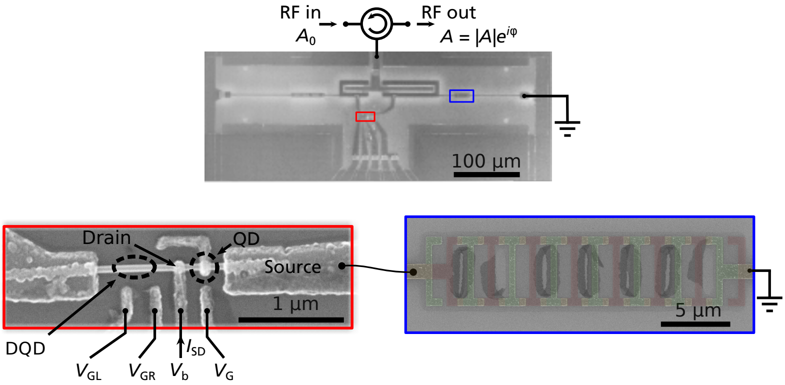

Figure 6.1: Scanning electron micrograph of the device (top) containing the nanowire with the quantum dots (red) and the resonator SQUID array (blue). The two shadows of the SQUID array have been colored in green and pink, showing the overlapping regions which form the Josephson junctions.

with N = 31 junctions and loop area 4 μm^2 [1] is present on the DQD side, but is not used for the studies presented herein. Additionally, a set of plunger gates enable us to tune the electron number on each of the three dots in the system semi-independently, apart from some crosstalk that can be compensated for. Finally, the QD is electrostatically coupled to the DQD via a coupler that extends from the QD over the drain. This coupler is directly connected to the QD in order to increase its sensitivity to the electrostatic environment of the DQD [2]. Further details on the device processing for this device are presented in Appendix A, and the details on the dilution refrigerator used for the measurements are presented in Appendix B

6.2 Measurement Results

6.2.1 Basic Characterization

Now we present the basic characterization of the device. We begin by measuring the DC transport of the quantum dot. Figure 6.2 (a) shows the current through the quantum dot as a function of the bias voltage and gate voltage. As before, we see the repeating pattern of coulomb diamonds with sharp conductance features. The

---

[1] The difference in loop area allows us to distinguish the two resonators by how quickly they oscillate with the magnetic field.

[2] This direct connection makes our quantum dot less "quantum" as the coupler is metallic / superconducting, and thus has a much shorter electronic wavelength compared to the size of the dot, meaning that coulomb interactions dominate. It would thus be more correct to call this device a "single electron transistor" [29].

conductance of one of the oscillations is shown in Figure 6.2 (b), where we select two points. The first is within coulomb blockade (CB) where the conductance of the quantum dot is minuscule, and one point at the coulomb degeneracy (CD) where the conductance is 0.4 μS.

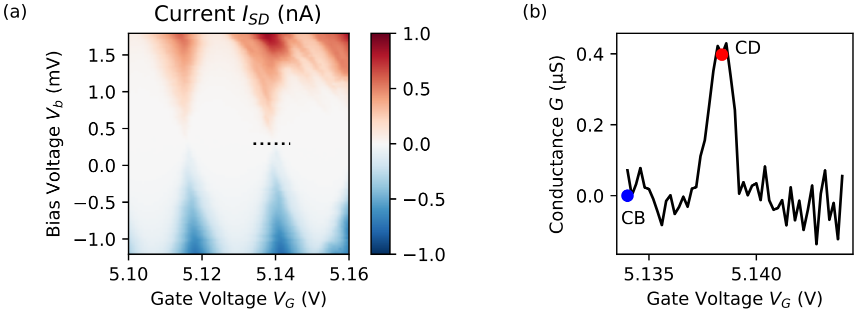

Figure 6.2: DC measurements of the QD. **(a)** The source-drain current I_{SD} of the QD measured as the bias voltage V_b and gate voltage V_G are varied. **(b)** The conductance of the coulomb oscillation near V_G 5.14 V, along the dashed black line in (a). The two points labeled CB and CD are the points used for subsequent measurements.

We now turn to the resonator, where we measure the reflected amplitude $|r|$ from the device while varying the frequency and an external magnetic field B. Figure 6.3 (a) shows two resonating modes oscillating in frequency as a function of the applied magnetic field, as expected from the magnetic field changing the phase ϕ across the junctions. The two modes correspond to the two resonators present on the device, with the higher maximum resonance frequency belonging to the resonator coupled to the quantum dot. The measurement here is normalized by the background amplitude, shown in Fig. 6.3 (b) [3]. We find this background amplitude as the median value of the reflected amplitude for each frequency. This method ignores account outliers such as the reflection dips, while also averaging away the noise.

We now fix the magnetic field such that the resonator attains a resonance frequency of $f_r = 6.75$ GHz, with the local oscillator frequency offset $\delta f = 12.5$ MHz and measure the reflection coefficient $|r|$ at a low input power $P_0 = 0.66$ fW. Figure 6.4 shows the reflected amplitude $|r|$ (a), phase $\angle r$ (b) of the resonator as a function of the drive frequency f. The blue dots shows the measured data in CB, from which we can fit eq. (3.35) to extract the bare resonator parameter values $\kappa_c = 62$ MHz, $\kappa_i = 60$ MHz, $\omega_r = 6.75$ GHz. The red data instead shows the resonator response at CD, where the QD has a large conductance. We see, that just as previously, the resonator response attains a larger linewidth, consistent with an added dissipation of $\kappa_s/2\pi = 28$ MHz, shown by the solid lines of the corresponding color. Lastly, in

---

[3] The amplitude of the background signal is decreasing because higher frequencies are attenuated stronger by the cabling

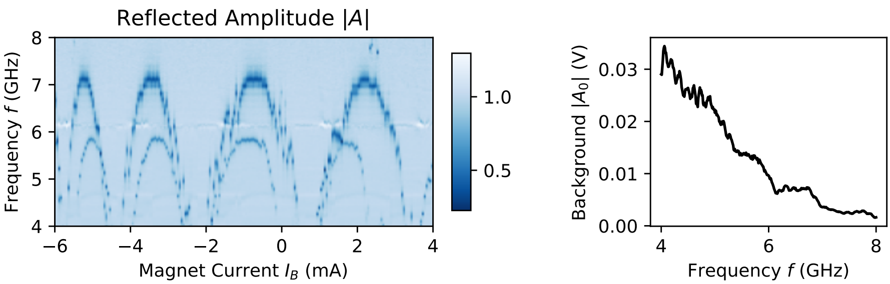

Figure 6.3: **(a)** The reflection response of the resonator as we vary the magnetic field. The signal has here been normalized with a background shown in **(b)** which we find from the median value of the reflected amplitude for each frequency.

Fig. 6.4 (c) we show the same data plotted instead in the complex plane showing the signal difference between the two states $|\Delta r| = 0.2$. We see that due to the large internal losses in the device, we are far from the ideal matching condition that would yield a maximized signal, where $\kappa_s \approx \kappa_c$ and $\kappa_i \ll \kappa_c$. Instead, the maximum signal difference between CB and CD here is $|\Delta r| = 0.2$.

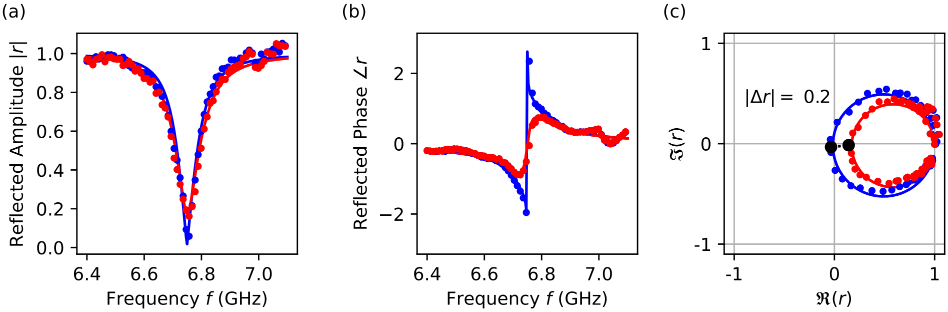

Figure 6.4: The low-power response of the resonator, measured with input power $P_0 = 0.66$ fW as the frequency f is varied. **(a)** shows the normalized reflected amplitude $|r|$, **(b)** the phase $\angle r$ and **(c)** the full complex response. The points in blue are the data measured at CB while the red is data measured at CD, while the lines are fits to eq. (3.35).

6.2.2 Nonlinear Response

Now we begin varying the input power P_0 of the resonator to bring it into the nonlinear regime. Figure 6.5 (a) shows this power- and frequency sweep of the resonator where we see it softening, just as in the numerical simulations.

From the measured resistance at room temperature $R_{300\ \mathrm{K}} = 1.25\ \mathrm{k}\Omega$ we can estimate the normal state resistance as $R_N = 1.5\ \mathrm{k}\Omega$, taking into account a $20\ \%$ increase

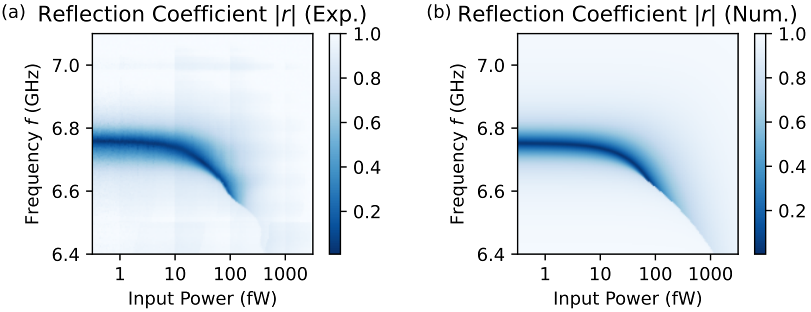

Figure 6.5: **(a)** Measurement of the reflection coefficient as we sweep the frequency f and input power P_0. **(b)** Numerical calculations of the system based on the device parameters found from the measurement.

in resistance as the temperature decreases [131]. Along with the resonator parameters found from the low-power measurements, this lets us calculate the inductance of the array along eq. (5.5) as $L = 20$ nH. With this value known, we can calculate the capacitance of the resonator as $C_\Sigma = 1/(\omega_{r,0}^2 L) = 25$ fF, giving us the characteristic impedance $Z_\mathrm{r} = 900\ \Omega$. Here, $\omega_{r,0} = 7.1$ GHz is the maximum frequency of the resonator in the magnetic field sweep where the inductance of the SQUID is unchanged due to the applied magnetic flux. Finally, using the input coupling κ_c, we can solve for the input capacitance $C_c = \sqrt{\kappa_c C_\Sigma/(Z_0\omega_r^2)} = 10$ fF. With these parameter values along with the number of junctions, Fig. 6.5 shows the numerically calculated resonator response. We see that our model is in good agreement with our experimental data, with the resonance frequency softening at the same rate [4].

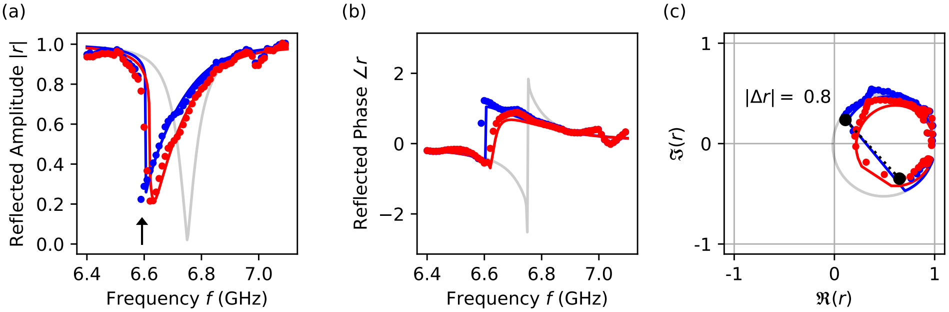

Figure 6.6: The high-power response of the resonator, measured with input power $P_0 = 66$ fW as the frequency f is varied. **(a)** shows the normalized reflected amplitude $|r|$, **(b)** the phase $\angle r$ and **(c)** the full complex response. The points in blue are the data measured at CB while the red is data measured at CD. The solid blue and red lines are solutions of the numeric calculations of eq. (5.42), while the gray line is showing the low-power CB response.

Now we fix the input power to $P_0 = 66$ fW, where the resonator is in the nonlinear

---

[4] There is a small discrepancy of 0.8 dB between the experiments and theory after taking into account the attenuation of the cryostat, however, as this is well within a reasonable error margin we adjust our attenuation estimate to include this discrepancy in the presented figures.

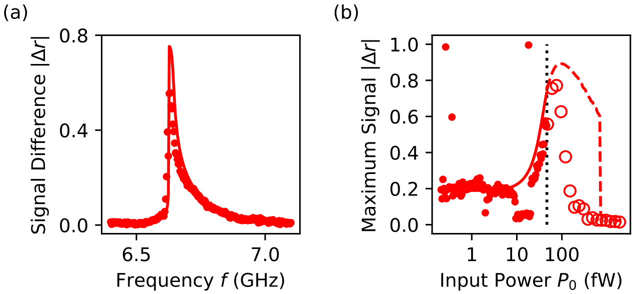

Figure 6.7: **(a)** The signal $|\Delta r|$ as a function of the input frequency at the power $P_0 = 66$ fW. **(b)** The maximum such signal measured for each input power in the experiment. The dashed arrow indicates P_C where the resonator enters the bifurcation. The points indicate the experimental values, and the lines show the result of the numerical calculations.

regime and measure again the resonator response in both CB and CD. Figure 6.6 shows the resulting measurement. We see here a qualitative difference between the low-power and high-power measurements. Notably, there is a frequency shift between CB and CD as a result of the added dissipation in the nonlinear response that does not appear in the linear regime. In Fig. 6.6 (c) we show the complex plane, with the black dots indicating two points in the CB and CD measurements at the same frequency, shown by the arrow in panel (a). From this we clearly see that the signal difference $|\Delta r| = 0.8$ is greatly increased compared to the low power linear response.

Figure 6.7 (a) shows this signal as a function of the frequency for a power $P_0 = P_c$ right at the onset of the bifurcation. We see here that the maximum signal depends strongly on the operating frequency f, increasing sharply from a low (near-zero) signal to the maximum of $|\Delta r| = 0.55$ (0.75) in the experiments (numerical calculations). Repeating this for each input power in the measurement yields Fig. 6.7 (b). The data shows that indeed, the low-power signal remains at 0.2 until the resonator enters the nonlinear regime, at which point the signal strength increases, reaching the threshold at which bifurcation occurs, indicated by the dashed black line. Further increases to the power appears to yield a greater signal in the numerical calculations. This, however, is due to the switching not being taken into account.

Furthermore, we can consider eq. (5.25) for the frequency shift of the resonance mode as the power is increased. Here we see that the added dissipation decreases the ratio κ_C/κ^2, reducing the shift of the resonant mode. We can quantify this difference as

$$\Delta\omega_K = \frac{4\pi Z_r \omega_r \kappa_c P_0}{R_Q N^2 \kappa_{CB} \hbar\omega_r}\left(1 - \frac{\kappa_{CB}^2}{(\kappa_{CB}+\kappa_s)^2}\right) \approx \frac{8\pi Z_r \omega_r \kappa_c P_0}{R_Q N^2 \hbar\omega_r}\frac{\kappa_s}{\kappa_{CB}} \tag{6.1}$$

where $\kappa_{CB} = \kappa_c + \kappa_i$ is the linewidth of the bare resonator.

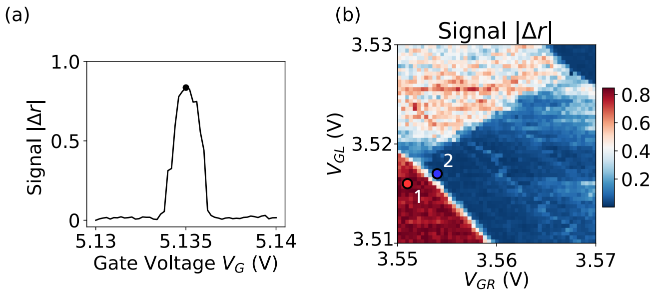

Figure 6.8: **(a)** The signal $|\Delta r|$ as a function of the gate voltage V_G on the sensor dot. The point indicates the point that the sensor was fixed to during the charge stability diagram measurement on the DQD shown in **(b)**. Here, two points are chosen in different charge regions for the subsequent measurements.

Intuitively, following eq. (5.45), we see that the resonator becomes nonlinear for a set number of photons. As the dissipation is increased, the lifetime for the photons in the cavity is decreased, resulting in a corresponding reduction to the photon number. This makes the resonator less nonlinear, and thus shifts the frequency. Since the nonlinear response has a steep slope at the low-frequency side, one attains a large signal difference for a relatively small frequency shift.

6.2.3 Charge Detection

Now we will use the device in order to probe the charge state of the DQD. We begin in Fig. 6.8 (a) by tuning the QD into the coulomb degeneracy point (CD) by measuring the reflected amplitude as the gate voltage of the sensor dot is varied. We then fix the QD to this state, while tuning the gate voltages on the DQD [5]. Figure 6.8 (b) shows the resulting charge stability diagram of the DQD as measured by the sensor, showing four different charge regions. We will now move to evaluating the readout speed of the charge sensor when using it in the linear regime and in the nonlinear regime

Here we choose two points in different charge regions, labeled in the charge stability diagram as 1 and 2. We then place the charge detector in each of these points to repeatedly measure the detector signal as a function of time, with the resonator tuned to the linear and nonlinear regimes respectively for a total of 100 measurements. The measurement retrieves a 2 ms long time trace of the detector signal with points every 20 ns, from which we find the in-phase and quadrature components as described in Section B.2. We then use the first N periods to calculate the time dependent signal

---

[5] Due to the cross-coupling, changing the DQD gate voltages will impose a change to the QD gate voltage, shifting the QD away from the degeneracy point. We correct for this by applying a compensation voltage that counteracts this effect.

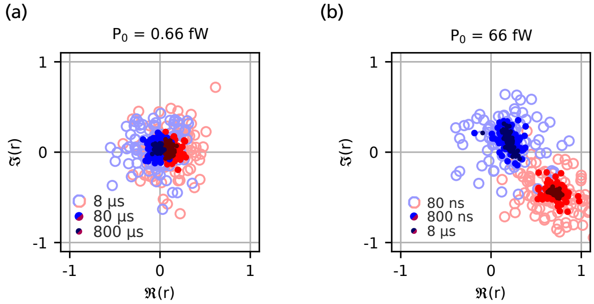

Figure 6.9: Scatter plots of the resonator signal taken **(a)** in the linear regime, $P_0 = 0.66$ fW, and **(b)** in the nonlinear regime $P_0 = 66$ fW. The red (blue) data corresponds to the gate voltage set to point 1 (2) in the charge stability diagram of 6.8, while the different markers indicate the integration time for the data.

with integration time $\tau = 80N$ ns. Figure 6.9 shows scatter plots for the resonator in the linear (a) and nonlinear (b) regime. The red (blue) data are measured at point 1 (2) from Fig. 6.8. We see here the data measured for three different integration times in each case, chosen to show the timescales for which the two different settings allow for clear separation of the two states.

Since there is a two orders of magnitude difference in the input power between the two cases, the linear regime naturally operates two orders of magnitude slower. Despite this inherent difference, however, we see a clear increase in performance when operating the resonator in the nonlinear regime, due to the much larger signal that we can utilize.

We can now calculate the noise $\sigma = \sqrt{\Re(r)^2 + \Im(r)^2}$, and the signal $S = |\bar{r_1} - \bar{r_2}|$ as a function of the integration time τ. From this, we find the signal to noise ratio which we show in Fig. 6.10 (a). Here, we make a fit to the data following SNR $= \sqrt{\tau/\tau_0}$. From this, we find the minimum integration time τ_0 where the $SNR = 1$ [49]. These data show the nonlinear resonator achieving an SNR of 1 at a minimum integration time of $\tau_0 = 10$ ns, which is within the same order of magnitude as some of the faster charge detectors in the literature [49, 99, 132]. In the linear operating regime, this is only achieved at $\tau_0 = 25\ \mu$s. Taking into account the two orders of magnitude difference, we see that this still corresponds to a speedup of 25 times due to the increased signal strength [6]. Next, we define the fidelity of the charge readout as the probability of correctly determining the charge state from the measurement. This is calculated by defining a threshold line and counting the number of data points on the correct side of the line. This quantity is shown in Fig. 6.10 (b) where we see

---

[6] The expected value for the improvement would be 16, since the signal increased by a factor 4. The deviation between these two values is likely either due to the sensor not going fully from CD to CB, or noise in the calibration resulting in the setpoint being offset slightly in the linear case.

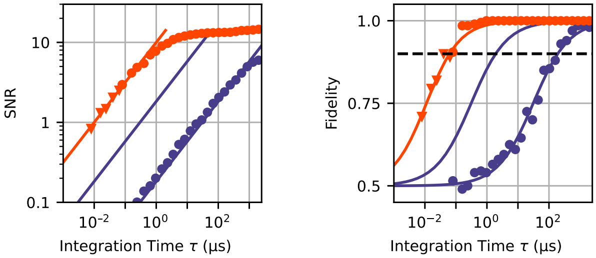

Figure 6.10: **(a)** The signal to noise ratio and **(b)** Fidelity as a function of the integration time τ. The red data shows the data gathered with the resonator in the nonlinear regime with $P_0 = 66$ fW, whereas the blue data shows the corresponding data measured in the linear regime measured at $P_0 = 0.66$ fW. The red triangles show a subsequent measurement where the intermediate frequency of the local oscillator was increased to $\delta f = 125$ MHz, resulting in measurement times of 8 ns. The solid lines are fits as described in the text. An additional copy of the linear fit line has been reproduced at two orders of magnitude shorter integration times, corresponding to the two orders of magnitude difference in input power used between the two cases.

that the fidelity exceeds 90 $\%$ for $\tau = 80$ ns. Using the same parameters as for the SNR, we fit these data to $F = 1 - 1/(1 + e^{\sqrt{\tau/\tau_0}})$, showing good agreement to the experimental data.

Finally, we present in Fig. 6.11 a measurement of the charge configuration on the DQD with a measurement time of $\tau = 80$ ns per data point[7]. We see that the (1,0) state in blue is easily distinguishable from both the (0,0), and (0,1) states, which both appear in red. The lack of contrast between the two remaining states here arises as the result of the nonlinear response. As the frequency shift occurs across the steep edge of the frequency response (as we see in Fig. 6.6), the continuously changing dissipation in the sensor leads to a steep change in response in the readout. After this point, further increases to the sensor dissipation leads only to a minimal change in the signal. In the presented charge stability diagram, the (0,0) state corresponds to a sensor dissipation above the threshold, the (1,0) state corresponds to a dissipation just above the threshold, and the (0,1) state corresponds a near-zero sensor dissipation, below the threshold.

---

[7] This would correspond to a total measurement time of 0.8 ms to retrieve the whole measurement. The actual experiment time is much longer as there is a significant time delay introduced in the communication time between the measurement script and the hardware. With proper optimization of this process, however, real-time video of the DQD charge configuration is possible, as was done in Ref. [132].

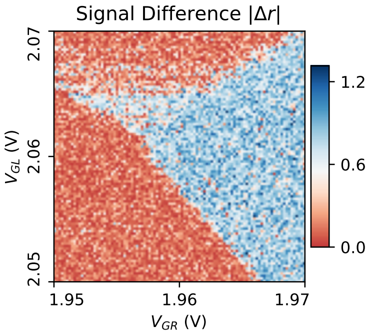

Figure 6.11: Measurement of the resonator signal $|\Delta r|$ as a function of the DQD gate voltages V_{GL} and V_{GR} using an integration time of $\tau = 80$ ns per point.

6.3 Prospects

In this section, we will discuss the potential benefits of performing the charge detection with a nonlinear resonator. These are all items which would benefit from further experiments to understand in better detail.

6.3.1 Increased Signal

We have experimentally demonstrated that the signal due to the added dissipation κ_s is increased in the measured device. The logical question to consider next then is for which range of parameters this signal increase can be found. To address this, we make use of the numerical calculations where, we now vary the sensor dissipation κ_s and internal losses κ_i while calculating the maximum signal difference. We do this by numerically calculating both the upper and lower branch of the resonator response, and excluding those frequencies for which two solutions exist. Then we find the largest signal difference between the two cases for a range of frequencies around $\omega_r - \kappa$ at the input power $P_0 = 0.95P_c$.

In Fig. 6.12 (a) we show the maximum signal for the linear resonator, as we found in Ch. 3, and in (b) we present the result of the above calculation. We see that using the nonlinearities allows us to maintain the large signal at a dissipation one order of magnitude lower than when using a linear resonator. This results in a region where the signal is increased, shown in Fig. 6.12 (c) where the nonlinear resonator provides a signal increase. We note that even for a device with $\kappa_s = \kappa_c$, there is a small improvement in the signal, corresponding to a 30 % increase in the reflected signal. Even a device which is otherwise well matched, would thus yield nearly a factor 2

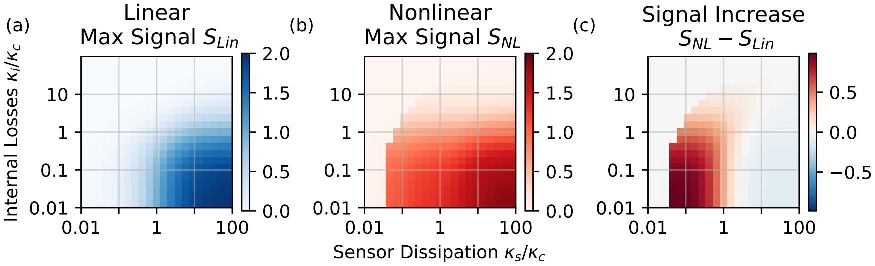

Figure 6.12: Calculations for varying sensor dissipation and internal losses. **(a)** The maximum signal possible in a linear resonator. **(b)** Maximum signal from the numerical calculations outside the switching regions with $P_0 = 0.95\ P_c$. **(c)** The signal increase from using the nonlinear operating mode over the linear operating mode.

increase in readout speed from the signal increase by using a nonlinear resonator.

6.3.2 Charge Noise Sensitivity

Next, we consider the effect of charge fluctuations, e.g. due to trapped states switching between being populated and empty of electrons [133]. The result of such changes in the charge environment is a small shift in the sensor, of the same character as that of the desired charge movement in the system of study. This leads to noise in the readout signal in magnitude proportional to the derivative of the sensor signal with respect to a small shift in the sensor voltage.

As the nonlinear operating regime relies on a frequency shift across the steep edge of the nonlinear response, the readout signal rapidly increases until the steep slope has been crossed, after which point further adding dissipation has little effect. In Fig. 6.13 (a) we calculate the signal for the resonator studied in paper II as a function of the sensor dissipation and input frequency f at $P_0 = 0.95 P_c$. We see that at the frequency corresponding to driving the resonator just at the edge of the steep reflection response, the signal increases sharply to a maximum after which it saturates to a fixed value for further increases in the dissipation. As we increase the drive frequency away from the edge, the dissipation required to reach the maximum signal is increased. Figure 6.13 (b) shows this clearly, as we plot the signal along the indicated horizontal cut lines, as a reference, the linear response, calculated from Eq. (3.61).

From the figure, we see that fluctuations in the dissipation thus have little effect in the high signal above a certain maximum dissipation. Provided that this value can be reached, one could then operate the sensor with reduced charge noise in the high conductance state. The tradeoff here, however, is that the low conductance state instead

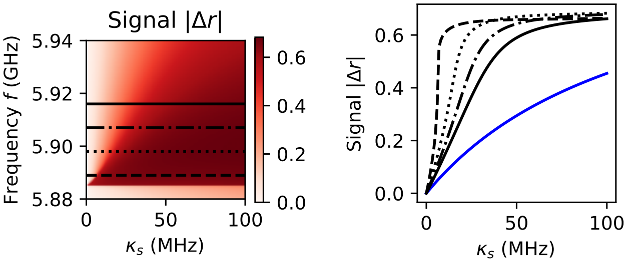

Figure 6.13: **(a)** Numerical calculation of the Signal at $P_0 = 0.95 P_c$ as a function of the input frequency f and added sensor dissipation κ_s. The remaining parameters as the device in Paper II. The four horizontal lines indicate cut-lines which are plotted separately in **(b)** along with the signal for a linear resonator.

becomes more sensitive to the same noise, as seen by the steeper signal increase for low dissipation compared to that of a linear resonator. However, an additional protection exists for all sensors of this time provided that the capacitive coupling to the system of interest is strong enough compared to that of the fluctuating charges. In this case, the sensor can be set such that the low conductance state lies firmly within the Coulomb blockade. Small changes to the sensor level will then not add any dissipation to the system, effectively eliminating the charge noise also for this state. This would be an interesting regime to study further as eliminating high-frequency charge noise could improve the noise level of the charge readout.

6.3.3 Bandwidth increase

As we saw in Ch. 3, the need to match the input coupling κ_c to the magnitude of added dissipation κ_s to reach a large signal sets a limit to the maximum bandwidth of the resonator. By using the nonlinear operating mode, however, we have seen that we can achieve the large signal difference even for smaller κ_s/κ_c. This implies that for a sensor of a set κ_s, a resonator operating within the nonlinear regime could use a higher κ_c to achieve the same readout signal, allowing for faster measurements within the resonator bandwidth. With the reported device, the bandwidth was 120 MHz in coulomb blockade, enabling sub-10 ns measurement times.

6.3.4 Backaction Protection

Finally, as the detector now relies on a frequency shift, there is a further benefit to consider to the backaction effects of the detector. Typically, the resonator in a dissipative sensor is always on resonance. When the quantum dot is in its conducting state, the input power from the resonator is thus dissipated into the sensor which can disturb the system of study [134–138]. With the nonlinear resonator, however, the resonance frequency shifts away from the drive frequency when the sensor is conducting. As the resonator is no longer driven on resonance, the transmitted power is thus reduced also in the conducting state, which may therefore reduce the backaction from the sensor.

6.4 Limits

In this section, we consider the limits to the performance of the nonlinear readout method.

6.4.1 Input Power Limit

In order to maximize the signal to noise ratio of the measurements, we want to operate the device at a high input power. Within this thesis, we have discussed two factors that sets a limit to this power[8]. First, we have the voltage amplitude of the resonator

$$V_{MW} = \left(\frac{4\kappa_c\omega_r Z_r P}{\kappa^2}\right)^{1/2} \tag{6.2}$$

which should not greatly exceed the linewidth of the sensor, $V_{MW} \lesssim \Gamma/e$. This sets a voltage-limited input power

$$P_V = \frac{\kappa^2\Gamma^2}{4e^2\kappa_c\omega_r Z_r}, \tag{6.3}$$

depending on the linewidth of the sensor. Second, we have the critical power at which the resonator bifurcation reaches the peak

$$P_C = \frac{N^2\Phi_0^2\kappa^3}{4\pi^2 Z_r\kappa_c}, \tag{6.4}$$

which depends on the number of junctions N. This is also the power at which the nonlinear advantage is the greatest.

For an optimal device, we can tune the number of junctions such that $P_c \approx P_V$, which gives

$$N = \frac{\pi K_J}{\sqrt{2\kappa\omega_r}}\frac{\Gamma}{e}, \tag{6.5}$$

---

[8] Among those left out we find the local heating of the device due to the input power [49] and the effects of back-action on the sensed device [134, 135]

where $K_J = 2e/h$ is the Josephson constant. As an example: for a bandwidth $\kappa/2\pi = 100$ MHz, corresponding to a rise-time of 10 ns, and a sensor linewidth of $\Gamma = 100\ \mu$eV, we find $N = 22$.

To make explicit the fact that this provides an optimal solution, we consider now deviations of N away from the derived value. As the power P_V is independent of the number of junctions in the array, this power is constant, and sets directly the maximum power where we would like to operate. If N is smaller than the optimal value, we find then that the bifurcation occurs at a power $P_0 < P_V$, forcing us to use a power such that we are not yet voltage broadened, meaning that we would not make the sensor worse by increasing the power further. Should N instead be larger than the optimal value, we end up not being able to reach the optimal nonlinearity where the signal is maximized before the sensor gets smeared by the voltage amplitude in the resonator, reducing the contrast and sensitivity of the detector.

6.4.2 Impedance Limits

Assuming that the number of junctions N is at the optimal value, the maximum input power we can use for the device is then set by

$$P_{\max} = \frac{\kappa^2\Gamma^2}{4e^2\kappa_c\omega_r Z_r}. \tag{6.6}$$

Keeping in mind that V_0, κ, κ_c and ω_r are fixed by previous assumptions[9] this leaves Z_r as the device parameter to minimize in order to increase the maximum power. However, doing so will in turn reduce the input coupling $\kappa_c = C_c\omega_r^3 Z_r Z_0$ and the sensor dissipation $\kappa_s = \mathrm{Re}(Y)\omega_r Z_r$ (where we have used $Z_r\omega_r = 1/C_\Sigma$), which we want to keep as large as possible. Choosing the impedance to use for the resonator thus becomes an optimization problem depending on the properties of the sensor, the desired resonator bandwidth and operating power.

6.4.3 High Current Limit

Another concern for driving the Josephson junction array strongly is that at some point the current oscillations become sufficiently large to exceed the critical current in the junctions. The maximum current in the resonator is found when the stored energy is entirely on the inductor, and settings this current to equal the critical current, we find

$$E = \frac{LI_C^2}{2} = n\hbar\omega_r. \tag{6.7}$$

---

[9] Although ω_r is not explicitly fixed, κ_c strongly depends on ω_r which implicitly fixes this parameter.

Expanding these expressions, we end up with

$$P_0 = \frac{N\Phi_0 I_C}{2\pi}\frac{\kappa^2}{4\kappa_c} \tag{6.8}$$

which we can insert into our Eq. (5.25) for the nonlinear frequency shift, we find that all terms cancel, leaving only

$$\frac{\omega_K}{\omega_r} = \frac{1}{16} \tag{6.9}$$

as a maximum frequency shift that can be supported by the nonlinear resonator. The current thus sets an upper bound for the bandwidth of the resonator at $\kappa = \omega_r/16$. This conclusion, however, depends on the assumption that the equations for the photon number in a linear resonator generalize to the nonlinear case, which is not necessarily true. It would thus be interesting to test this limit experimentally, as a verification of this equivalence.

Chapter 7

Conclusions and Outlook

To summarize this thesis we have studied the resonator-based readout method of charge-sensitive quantum dots at microwave frequencies between 4 and 8 GHz. In Paper I, we focused on the impact to the readout signal that is gained by operating the resonator at these frequencies, showing that the microwave photons within the resonator lead to additional transport possibilities. This serves both as a mechanism to enhance the dissipation of the quantum dot, allowing a larger signal at microwave frequencies than would be expected based on the DC transport, but also leads to a potential broadening of the sensor state which can limit the sensitivity. Furthermore, we also emphasize the impact of a large input power, resulting in that the wave-nature of the resonator also leads to a sensitivity reduction.

In Paper II, we further implement a high-impedance microwave resonator based on an array of SQUIDs. With a high impedance, a larger coupling can be achieved to the sensor, yielding a larger bandwidth for the resonator readout. Furthermore, we find that when driving the resonator strongly, such that we operate in the nonlinear regime, the resonator response is qualitatively different, leading to a larger readout signal. This allows us to achieve a near-unity readout signal from a poorly matched resonator system, yielding further benefits to the readout bandwidth.

Finally, we highlight a number of directions in which the work within this thesis could be continued. First, just as the sensor detects the charge on the system it is probing, so is that system detecting the charge on the sensor. However, as noted in Paper II, we anticipate that sensing with the nonlinear resonator offers some additional protection against backaction compared to a regular linear resonator. This is something that can be experimentally verified e.g. as in Ref. [138], where the decoherence of a charge qubit was measured while increasing the current through a capacitively coupled quantum dot, acting as a sensor. Extending this study to instead consider the different backaction achieved from using a linear, contra nonlinear resonator as the sensor conductivity is varied. Furthermore, one could study the backaction as a function of the input power of the resonator, again both in the linear and nonlinear regime. Second, it would be interesting to study the effect of charge noise on the nonlinear readout signal. Since the response increases sharply for a range of dissipation where the frequency shift crosses the steep slope while being insensitive to changes in dissipation outside of this range, small fluctuations in the sensor dissipation will therefore have a corresponding sensitivity. This may enable an additional protection against charge noise, which may reduce the overall noise present in the measurement. Finally, we have discussed the limit where the voltage amplitude in the microwave resonator broadens the sensor state. However, breaking this limit does not fundamentally stop the device from working as a sensor, as this only reduces the contrast in the sensor dissipation. It would thus be interesting to study whether this effect is strong enough to offset the benefit to the signal strength one would get for breaching the limit.

Appendix A

Cleanroom Fabrication

This chapter exists as a record of the cleanroom processing techniques that were used in the fabrication of the device used for Paper II. Its primary purpose is to exist as a starting point for others who want to create similar structures.

A.1 Full Processing Procedure.

We begin with a high-resistivity 2” silicon wafer grown with the Float-Zone method.

The first processing step involves placing alignment markers and contact pads for subsequent processes. This is done with an electron beam lithography (EBL) step, using 950 k PMMA A6 [1] electron beam resist spin-coated at 5000 rpm and baked at 180 °C for 2 minutes. The exposure is done with a 50 kV system using a dose of 700 μC/cm^2 for areas, and 14000 pC/cm for lines, and developed in 1:3 MIBK:IPA for 60 seconds followed by rinsing in IPA for 60 seconds. We then clean the sample in an oxygen plasma asher for 15 seconds under a Faraday cage. The pattern is then transferred by electron beam evaporating 5 nm Ti [2] and 45 nm Au. We then do the lift-off in acetone using a pipette to agitate until all resist has dissolved and the undesired metal has released. The wafer is then rinsed in IPA for 1 minute and blow-dried with nitrogen.

The second process step defines the Aluminium structures used for the RF input line, the DC contact pads, and the surrounding ground structure. These are defined with

---

[1] Poly(methyl methacrylate) polymer chains of molecular weight 950 000, dissolved to 6% in anisole.

[2] Titanium is used in a lot of the processes as a good sticking layer, as it easily bonds to oxygen present in surface layers of the substrate.

an optical lithography process using a 405 nm direct-write laser (DWL). The mask here is a two-layered mask with LOR 3A, spin coated at 2500 rpm and baked at 150 °C for 5 minutes followed by S1813 spin coated at 6000 rpm and baked to 115 °C for 90 seconds. After exposure with a dose of 200 μJ/cm^2, the resist is developed in MF-319 developer for 53 seconds, followed by a 60 second rinse in de-ionized water, we then clean the sample in the plasma asher as above. The pattern is transferred into 5 nm Ti and 95 nm of Al using the electron beam evaporator followed by lift-off in Remover 1165. Here we use two beakers of Remover 1165, switching to the second beaker (after approximately 10 minutes) as the majority of the resist and metal has been removed in the first. We keep the device in this beaker until they are free of additional metal, using an ultrasonic bath if necessary. We then rest the sample in IPA for 10 minutes before switching to a clean beaker of IPA where we let the sample rest for another 10 minutes before drying with nitrogen[3].

In the third step we repeat the above lithography process to create a large opening over the DC lines and ground planes. This pattern is then transferred into an atomic-layer-deposition of AlO$_x$ followed by 100 nm of electron beam evaporated Al and lift-off with . This creates a large capacitive shunting of all DC lines to ground, shunting high-frequency signals to prevent leakage of the microwave modes.

After this processing step, we coat the wafer with a protective layer of PMMA A6[4] and dice the 2" wafer into 6 smaller chips. We clean the protective layer for 2 min in Acetone and rinse it in 2 min in IPA before depositing nanowires with a micro manipulator within the 100x100 μm^2 fields of alignment marks defined in step 1. Each field is then inspected with an SEM to find suitable nanowires for further processing. For this we use the alignment markers placed in a 5x5 μm^2 grid pattern to discern the location of each nanowire. The nanowires here are made from InAs with built-in electrical barriers made by switching the crystal growth from Zinc-Blende (ZB) to Wurtzite (WZ). In order to correctly locate these barriers, a shell of GaSb has been grown selectively on the ZB regions. This overgrowth makes the nanowire thinner where we have barriers, which we can see in the electron micrograph, allowing us to align gates and ohmic contacts to the nanowire.

Next, we need to etch the GaSB shell from the nanowire. We spin coat PMMA A6 at 5000 rpm and bake at 180 °C and expose all but the ends of the nanowire in the EBL. After developing as above, we then submerge the chip in MF319 for 5 minutes to wet etch the shell. Following this, we spin coat PMMA A4 at 5000 rpm and bake

---

[3] This liftoff process is more involved than that for EBL resist, particularly the LOR is difficult to remove, hence requiring Remover 1165, which itself can leave residues on the sample if not washed away properly in the IPA.

[4] This layer is only here to protect the surface from the dicing process, the exact type of resist is not important.

at 180 °C. We then pattern the nanowire contacts and resonator input capacitance structures, develop and clean all with the same exposure parameters, chemistry and plasma ashing as in step 1. The pattern is then transferred into 5 nm Ti and 135 nm Al to make the contacts with as low resistance as possible.

Finally, we will put the Josephson junction array onto the chip. Here we will use a two-layer mask to create a large undercut for two-angle evaporation [128–130]. We first spin coat MMA EL9 at 4000 rpm, and bake at 150 °C for 1 minute and repeat this step for a total of three layers. Then we spin coat 950k PMMA A6 at 5000 rpm and bake at 150 °C for 2 minutes. Using the 50 kV EBL system, we then expose the sample with a dose of 700 μC/cm^2 where we want to clear the PMMA, followed by a dose of 150 μC/cm^2 where we want an undercut. After developing as in step 1 without plasma ashing the sample, we then load the devices into the evaporator where we evaporate a layer of 35 nm Al at a 30° angle (in the direction of the resonator array). Next, oxygen is let into the chamber, reaching a pressure of 0.49 T after 2 minutes, which is maintained for another 2 minutes before pumping down to a vacuum again. The angle is then changed to -30° where a second layer of 70 nm Al is deposited. Finally, the mask is removed in an acetone bath until fully dissolved, followed by a wash in IPA.

Appendix B

Measurement Setup

All measurements presented in this thesis were measured in a Dilution refrigerator at temperatures of 10 mK. As the high-frequency signals are generated at room temperature, they also carry high-temperature noise. However, the experiments performed within this thesis require signals of specific (low) power levels, that

B.1 Measurement Attenuation

To minimize the amount of this noise that makes it into the cryostat, we generate a larger signal than we need, which we then attenuate as the signal reaches the colder parts of the dilution refrigerator, as shown in Fig. B.1.

We generate the signal at the top of the input line and passes via a total of 88.5 dB attenuation and the two circulators into the device. The reflections from the device then go through the circulators into the output line, where they are first amplified by +40 dB at the $T \approx 2\text{K}$ stage by a high-electron mobility transistor (HEMT) [1]. The amplification from the HEMT ensures that the noise in the measurement is limited by the noise level of the cold signal as it was leaving the cryostat, as further thermal fluctuations are small compared to the amplified low-temperature noise. A final set of room temperature amplifiers are then sufficient to make the signal level large enough to digitize it.

---

[1] We use two circulators here as there is a risk of the signal being reflected at the HEMT. With only a single circulator, the isolation to the device from this reflected signal is only about 20 dB (or 99 % of the power), which could lead to errors in the measurements. Adding a second circulator further reduces this leakage by another 20 dB, significantly reducing the risk of this process impacting the measurements.

However, as the signal is also attenuated slightly by the high-frequency lines between the signal generators and the device, we have to take these into account in order to determine the signal level at the device input. We do this by assuming that the attenuation from the input- and output line are identical, with a value of x dBm each. The total attenuation of the setup is then given by

$$\alpha = \alpha_{in} + \alpha_{out} + 2x, \tag{B.1}$$

where $\alpha_{in} = -88.8$ and $\alpha_{out} = 96.8$ is the sum of attenuation from all components inserted into the circuit. We then send a signal of known power ($P = 0$ dBm) into the cryostat and determine the power at the measurement end ($P = -19.6$ dBm), giving the total attenuation, from which we find the cable losses $x = -13.8$. Table B.1 shows all the components included in this calibration, as done for Paper II. In Paper I, the setup was identical to that of Ref. [10], where the corresponding power calibration can be found.

Table B.1: Tabulated values for the attenuation / amplification of each component used in the measurement circuitry at the $f = 6.7$ GHz frequency used in the measurements.

Cryostat Input	Signal change at $f = 6.7$ GHz (dB)
36 inch cable: 141-36SM+	-1.2
Splitter: ZX10R-14-S+	-7.16
20 dB attenuator: FW-20+	-21.27
Cryostat attenuation	-59
Circulator insertion loss	-0.2 dBm
Additional cable losses	$x = -13.8$ dBm
Cryostat Output	**Signal change at $f = 6.7$ GHz (dB)**
2×Circulator: LNF-CIC4_8A (Insertion Loss)	-0.2
HEMT amplifier: LNF-LNC4_8C	$+41.62$
Cryostat attenuation	-4
3×MOSFET amplifier: ZX60-83LN12+	$+20.58$
4 × 3 dB attenuation: FW-3+	4×-3.43
Mixer: ZMX-10G+ (Conversion loss)	-4.7 [a]
Additional cable losses	$x = -13.8$ dBm
Post-Mixer	**Signal change at $f = 12.5$ MHz (dB)**
2 inch cable: 141-2SM+	-0.01
3.4 GHz LPF: VLF-3400+	-0.01
80 MHz LPF: VLF-80+	-0.35
Attenuation [b]	-2.44
Amplifier: HVA-200M-40-B	$+20$
20 MHz Oscilloscope Bandwidth	-0.86

---

[a] Upon further inspection of the data sheet, there appears to be a discrepancy with this value. The tabulated value is 4.7 dB, however, the measured value as indicated in the figures is rather around 6.8.

[b] This attenuation was unintended, but arose as a connector with a parallel grounding stub was used on the amplifier input.

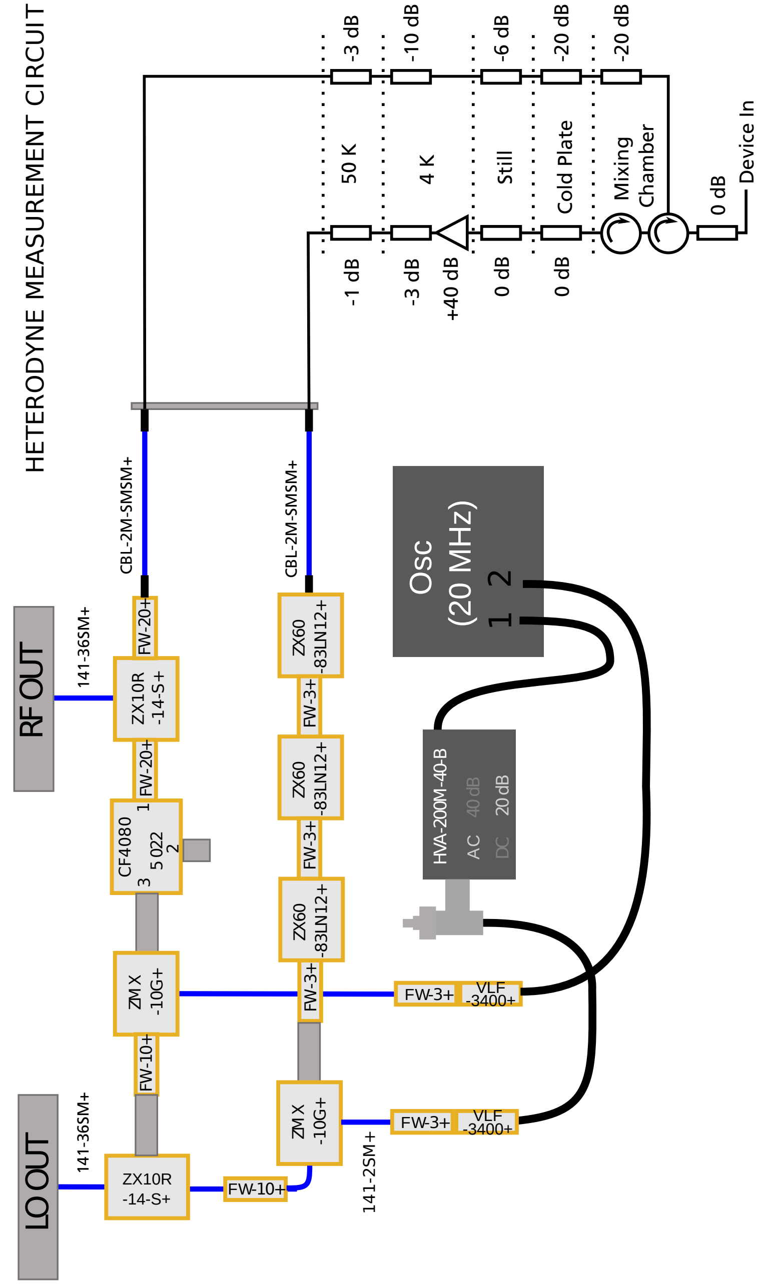

Figure B.1: Circuitry used for the RF measurements in Paper II.

B.2 High-Frequency Measurements

Digitizing GHz signals can be difficult due to the high frequency oscillations. However, by utilizing a frequency mixer with our signal of frequency f and that of a local oscillator with frequency $f_{LO} = f + \delta f$, we end up with a signal, shown in Fig. B.2 as the gray line, containing the sum and difference of the two frequencies, $f_1 = f + f_{LO} = 2f + \delta f$ and $f_2 = f - f_{LO} = \delta f$. Provided that $\delta f < f$, we can filter out the high-frequency signal with a simple low-pass filter, resulting in the black line the figure. The measurement then digitizes the signal with a sampling frequency of $f_s = 4\delta f$ such that we have four points per period of the oscillation. This allows us to extract the two quadratures of the signal in Fig. B.2. From the two quadratures, we easily calculate the amplitude $A = \sqrt{I^2 + Q^2}$ and phase $\phi = \arctan(I/Q)$. The phase of the signal, however, is random due to uncertainty in when the sampling started. To extract the real phase information of the signal, we compare it to a phase reference that is generated by splitting both the original signal and the local oscillator and mixing these as above without passing them through the sample. This makes a phase reference, which can be used to find the phase difference that the signal accumulated by interacting with the device.

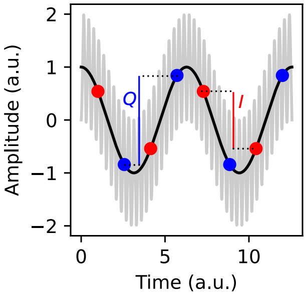

Figure B.2: The resulting signals after the frequency mixing. The gray line shows the resulting signal with a high-frequency component $f + f_{LO}$ which is filtered away, the black line shows the remaining low frequency signal $f - f_{LO}$ which is measured. The dots show the points that are sampled in the digitization, with the quadratures calculated as the difference between the pairs of points as shown by the vertical lines.

References

[1] V. Bouchiat, D. Vion, P. Joyez, D. Estève, and M. H. Devoret, "Quantum coherence with a single cooper pair," *Physica Scripta*, vol. 1998, pp. 165–170, 1998.

[2] T. Duty, D. Gunnarsson, K. Bladh, and P. Delsing, "Coherent dynamics of a josephson charge qubit," *Phys. Rev. B*, vol. 69, p. 140503, Apr 2004.

[3] N. E. Penthorn, J. S. Schoenfield, J. D. Rooney, L. F. Edge, and H. Jiang, "Two-axis quantum control of a fast valley qubit in silicon," *npj Quantum Information*, vol. 5, p. 94, Nov 2019.

[4] B. E. Kane, "A silicon-based nuclear spin quantum computer," *Nature*, vol. 393, pp. 133–137, May 1998.

[5] D. Loss and D. P. DiVincenzo, "Quantum computation with quantum dots," *Phys. Rev. A*, vol. 57, pp. 120–126, Jan 1998.

[6] L. M. K. Vandersypen, H. Bluhm, J. S. Clarke, A. S. Dzurak, R. Ishihara, A. Morello, D. J. Reilly, L. R. Schreiber, and M. Veldhorst, "Interfacing spin qubits in quantum dots and donors—hot, dense, and coherent," *npj Quantum Information*, vol. 3, p. 34, Sep 2017.

[7] R. Hanson, L. P. Kouwenhoven, J. R. Petta, S. Tarucha, and L. M. K. Vandersypen, "Spins in few-electron quantum dots," *Rev. Mod. Phys.*, vol. 79, pp. 1217–1265, Oct 2007.

[8] S. Gustavsson, M. Studer, R. Leturcq, T. Ihn, K. Ensslin, D. C. Driscoll, and A. C. Gossard, "Frequency-selective single-photon detection using a double quantum dot," *Phys. Rev. Lett.*, vol. 99, p. 206804, Nov 2007.

[9] A. Ghirri, S. Cornia, and M. Affronte, "Microwave photon detectors based on semiconducting double quantum dots," *Sensors*, vol. 20, no. 14, 2020.

[10] W. Khan, P. P. Potts, S. Lehmann, C. Thelander, K. A. Dick, P. Samuelsson, and V. F. Maisi, “Efficient and continuous microwave photoconversion in hybrid cavity-semiconductor nanowire double quantum dot diodes,” *Nature Communications*, vol. 12, p. 5130, Aug 2021.

[11] S. Cornia, V. Demontis, V. Zannier, L. Sorba, A. Ghirri, F. Rossella, and M. Affronte, “Calibration-free and high-sensitivity microwave detectors based on inas/inp nanowire double quantum dots,” *Advanced Functional Materials*, vol. n/a, no. n/a, p. 2212517.

[12] M. W. Keller, A. L. Eichenberger, J. M. Martinis, and N. M. Zimmerman, “A capacitance standard based on counting electrons,” *Science*, vol. 285, no. 5434, pp. 1706–1709, 1999.

[13] J. P. Pekola, O.-P. Saira, V. F. Maisi, A. Kemppinen, M. Möttönen, Y. A. Pashkin, and D. V. Averin, “Single-electron current sources: Toward a refined definition of the ampere,” *Rev. Mod. Phys.*, vol. 85, pp. 1421–1472, Oct 2013.

[14] D. J. van Woerkom, A. Geresdi, and L. P. Kouwenhoven, “One minute parity lifetime of a nbtin cooper-pair transistor,” *Nature Physics*, vol. 11, pp. 547–550, Jul 2015.

[15] E. T. Mannila, P. Samuelsson, S. Simbierowicz, J. T. Peltonen, V. Vesterinen, L. Grönberg, J. Hassel, V. F. Maisi, and J. P. Pekola, “A superconductor free of quasiparticles for seconds,” *Nature Physics*, vol. 18, pp. 145–148, Feb 2022.

[16] A. Ranni, F. Brange, E. T. Mannila, C. Flindt, and V. F. Maisi, “Real-time observation of cooper pair splitting showing strong non-local correlations,” *Nature Communications*, vol. 12, p. 6358, Nov 2021.

[17] J. V. Koski, V. F. Maisi, J. P. Pekola, and D. V. Averin, “Experimental realization of a Szilard engine with a single electron,” *PNAS*, vol. 111, pp. 13786–13789, Sept. 2014.

[18] J. V. Koski, V. F. Maisi, T. Sagawa, and J. P. Pekola, “Experimental observation of the role of mutual information in the nonequilibrium dynamics of a maxwell demon,” *Phys. Rev. Lett.*, vol. 113, p. 030601, Jul 2014.

[19] D. Barker, M. Scandi, S. Lehmann, C. Thelander, K. A. Dick, M. Perarnau-Llobet, and V. F. Maisi, “Experimental verification of the work fluctuation-dissipation relation for information-to-work conversion,” *Phys. Rev. Lett.*, vol. 128, p. 040602, Jan 2022.

[20] R. Garreis, J. D. Gerber, V. Stará, C. Tong, C. Gold, M. Röösli, K. Watanabe, T. Taniguchi, K. Ensslin, T. Ihn, and A. Kurzmann, “Counting statistics of

single electron transport in bilayer graphene quantum dots," *Phys. Rev. Res.*, vol. 5, p. 013042, Jan 2023.

[21] B. Küng, C. Rössler, M. Beck, M. Marthaler, D. S. Golubev, Y. Utsumi, T. Ihn, and K. Ensslin, "Irreversibility on the level of single-electron tunneling," *Phys. Rev. X*, vol. 2, p. 011001, Jan 2012.

[22] G. Manzano, D. Subero, O. Maillet, R. Fazio, J. P. Pekola, and E. Roldán, "Thermodynamics of gambling demons," *Phys. Rev. Lett.*, vol. 126, p. 080603, Feb 2021.

[23] B. Annby-Andersson, P. Samuelsson, V. F. Maisi, and P. P. Potts, "Maxwell's demon in a double quantum dot with continuous charge detection," *Phys. Rev. B*, vol. 101, p. 165404, Apr 2020.

[24] M. Field, C. G. Smith, M. Pepper, D. A. Ritchie, J. E. F. Frost, G. A. C. Jones, and D. G. Hasko, "Measurements of coulomb blockade with a noninvasive voltage probe," *Phys. Rev. Lett.*, vol. 70, pp. 1311–1314, Mar 1993.

[25] E. Buks, R. Schuster, M. Heiblum, D. Mahalu, and V. Umansky, "Dephasing in electron interference by a 'which-path' detector," *Nature*, vol. 391, pp. 871–874, Feb 1998.

[26] J. M. Elzerman, R. Hanson, L. H. Willems van Beveren, B. Witkamp, L. M. K. Vandersypen, and L. P. Kouwenhoven, "Single-shot read-out of an individual electron spin in a quantum dot," *Nature*, vol. 430, pp. 431–435, Jul 2004.

[27] T. Fujisawa, T. Hayashi, R. Tomita, and Y. Hirayama, "Bidirectional counting of single electrons," *Science*, vol. 312, no. 5780, pp. 1634–1636, 2006.

[28] J. R. Petta, A. C. Johnson, C. M. Marcus, M. P. Hanson, and A. C. Gossard, "Manipulation of a single charge in a double quantum dot," *Phys. Rev. Lett.*, vol. 93, p. 186802, Oct 2004.

[29] D. V. Averin and K. K. Likharev, "Coulomb blockade of single-electron tunneling, and coherent oscillations in small tunnel junctions," *Journal of Low Temperature Physics*, vol. 62, pp. 345–373, Feb 1986.

[30] T. A. Fulton and G. J. Dolan, "Observation of single-electron charging effects in small tunnel junctions," *Phys. Rev. Lett.*, vol. 59, pp. 109–112, Jul 1987.

[31] G. Bazán, A. O. Orlov, G. L. Snider, and G. H. Bernstein, "Charge detector realization for algaas/gaas quantum␣dot cellular automata," *Journal of Vacuum Science & Technology B: Microelectronics and Nanometer Structures Processing, Measurement, and Phenomena*, vol. 14, no. 6, pp. 4046–4050, 1996.

[32] C. Volk, A. Chatterjee, F. Ansaloni, C. M. Marcus, and F. Kuemmeth, “Fast charge sensing of si/sige quantum dots via a high-frequency accumulation gate,” *Nano Letters*, vol. 19, pp. 5628–5633, Aug 2019.

[33] W. Li, J. Mu, Z.-H. Liu, S. Huang, D. Pan, Y. Chen, J.-Y. Wang, J. Zhao, and H. Q. Xu, “Charge detection of a quantum dot under different tunneling barrier symmetries and bias voltages.,” *Nanoscale*, 2021.

[34] L. Roschier, P. Hakonen, K. Bladh, P. Delsing, K. W. Lehnert, L. Spietz, and R. J. Schoelkopf, “Noise performance of the radio-frequency single-electron transistor,” *Journal of Applied Physics*, vol. 95, pp. 1274–1286, 02 2004.

[35] F. Vigneau, F. Fedele, A. Chatterjee, D. Reilly, F. Kuemmeth, M. F. Gonzalez-Zalba, E. Laird, and N. Ares, “Probing quantum devices with radio-frequency reflectometry,” *Applied Physics Reviews*, vol. 10, p. 021305, 02 2023.

[36] M. De Michielis, E. Ferraro, E. Prati, L. Hutin, B. Bertrand, E. Charbon, D. J. Ibberson, and M. Fernando Gonzalez-Zalba, “Silicon spin qubits from laboratory to industry,” *Journal of Physics D: Applied Physics*, vol. 56, p. 363001, jun 2023.

[37] R. J. Schoelkopf, P. Wahlgren, A. A. Kozhevnikov, P. Delsing, and D. E. Prober, “The radio-frequency single-electron transistor (rf-set): A fast and ultrasensitive electrometer,” *Science*, vol. 280, no. 5367, pp. 1238–1242, 1998.

[38] W. Lu, Z. Ji, L. Pfeiffer, K. W. West, and A. J. Rimberg, “Real-time detection of electron tunnelling in a quantum dot,” *Nature*, vol. 423, pp. 422–425, May 2003.

[39] A. J. Ferguson, N. A. Court, F. E. Hudson, and R. G. Clark, “Microsecond resolution of quasiparticle tunneling in the single-cooper-pair transistor,” *Phys. Rev. Lett.*, vol. 97, p. 106603, Sep 2006.

[40] M. C. Cassidy, A. S. Dzurak, R. G. Clark, K. D. Petersson, I. Farrer, D. A. Ritchie, and C. G. Smith, “Single shot charge detection using a radio-frequency quantum point contact,” *Applied Physics Letters*, vol. 91, no. 22, p. 222104, 2007.

[41] D. J. Reilly, C. M. Marcus, M. P. Hanson, and A. C. Gossard, “Fast single-charge sensing with a rf quantum point contact,” *Applied Physics Letters*, vol. 91, no. 16, p. 162101, 2007.

[42] H. A. Nilsson, T. Duty, S. Abay, C. Wilson, J. B. Wagner, C. Thelander, P. Delsing, and L. Samuelson, “A radio frequency single-electron transistor based on an inas/inp heterostructure nanowire,” *Nano Letters*, vol. 8, pp. 872–875, Mar 2008.

[43] S. J. Angus, A. J. Ferguson, A. S. Dzurak, and R. G. Clark, "A silicon radio-frequency single electron transistor," *Applied Physics Letters*, vol. 92, no. 11, p. 112103, 2008.

[44] C. Barthel, M. Kjærgaard, J. Medford, M. Stopa, C. M. Marcus, M. P. Hanson, and A. C. Gossard, "Fast sensing of double-dot charge arrangement and spin state with a radio-frequency sensor quantum dot," *Phys. Rev. B*, vol. 81, p. 161308, Apr 2010.

[45] C. Ciccarelli and A. J. Ferguson, "Impedance of the single-electron transistor at radio-frequencies," *New Journal of Physics*, vol. 13, p. 093015, sep 2011.

[46] S. J. Chorley, J. Wabnig, Z. V. Penfold-Fitch, K. D. Petersson, J. Frake, C. G. Smith, and M. R. Buitelaar, "Measuring the complex admittance of a carbon nanotube double quantum dot," *Phys. Rev. Lett.*, vol. 108, p. 036802, Jan 2012.

[47] M. Jung, M. D. Schroer, K. D. Petersson, and J. R. Petta, "Radio frequency charge sensing in inas nanowire double quantum dots," *Applied Physics Letters*, vol. 100, no. 25, p. 253508, 2012.

[48] N. Ares, F. J. Schupp, A. Mavalankar, G. Rogers, J. Griffiths, G. A. C. Jones, I. Farrer, D. A. Ritchie, C. G. Smith, A. Cottet, G. A. D. Briggs, and E. A. Laird, "Sensitive radio-frequency measurements of a quantum dot by tuning to perfect impedance matching," *Phys. Rev. Appl.*, vol. 5, p. 034011, Mar 2016.

[49] D. Keith, M. G. House, M. B. Donnelly, T. F. Watson, B. Weber, and M. Y. Simmons, "Single-shot spin readout in semiconductors near the shot-noise sensitivity limit," *Phys. Rev. X*, vol. 9, p. 041003, Oct 2019.

[50] R. Mizokuchi, S. Bugu, M. Hirayama, J. Yoneda, and T. Kodera, "Radio-frequency single electron transistors in physically defined silicon quantum dots with a sensitive phase response," *Sci Rep*, vol. 11, p. 5863, Mar. 2021.

[51] V. O. Turin and A. N. Korotkov, "Analysis of the radio-frequency single-electron transistor with large quality factor," *Appl. Phys. Lett*, vol. 83, pp. 2898–2900, 10 2003.

[52] A. Blais, A. L. Grimsmo, S. M. Girvin, and A. Wallraff, "Circuit quantum electrodynamics," *Rev. Mod. Phys.*, vol. 93, p. 025005, May 2021.

[53] M. Göppl, A. Fragner, M. Baur, R. Bianchetti, S. Filipp, J. M. Fink, P. J. Leek, G. Puebla, L. Steffen, and A. Wallraff, "Coplanar waveguide resonators for circuit quantum electrodynamics," *Journal of Applied Physics*, vol. 104, no. 11, p. 113904, 2008.

[54] A. Stockklauser, P. Scarlino, J. V. Koski, S. Gasparinetti, C. K. Andersen, C. Reichl, W. Wegscheider, T. Ihn, K. Ensslin, and A. Wallraff, "Strong coupling cavity qed with gate-defined double quantum dots enabled by a high impedance resonator," *Phys. Rev. X*, vol. 7, p. 011030, Mar 2017.

[55] A. Ranni, H. Havir, S. Haldar, and V. F. Maisi, "High impedance josephson junction resonators in the transmission line geometry," *Applied Physics Letters*, vol. 123, p. 114002, 09 2023.

[56] N. Pedersen, "Non-linear properties of josephson junctions," *Physica D: Nonlinear Phenomena*, vol. 68, no. 1, pp. 27–34, 1993.

[57] F. R. Ong, M. Boissonneault, F. Mallet, A. Palacios-Laloy, A. Dewes, A. C. Doherty, A. Blais, P. Bertet, D. Vion, and D. Esteve, "Circuit QED with a nonlinear resonator: AC-Stark shift and dephasing," *Phys. Rev. Lett.*, vol. 106, p. 167002, Apr 2011.

[58] I. Siddiqi, R. Vijay, F. Pierre, C. M. Wilson, M. Metcalfe, C. Rigetti, L. Frunzio, and M. H. Devoret, "RF-driven Josephson bifurcation amplifier for quantum measurement," *Phys. Rev. Lett.*, vol. 93, p. 207002, Nov 2004.

[59] A. Wallraff, D. I. Schuster, A. Blais, L. Frunzio, J. Majer, M. H. Devoret, S. M. Girvin, and R. J. Schoelkopf, "Approaching unit visibility for control of a superconducting qubit with dispersive readout," *Phys. Rev. Lett.*, vol. 95, p. 060501, Aug 2005.

[60] A. Lupaşcu, E. F. C. Driessen, L. Roschier, C. J. P. M. Harmans, and J. E. Mooij, "High-contrast dispersive readout of a superconducting flux qubit using a nonlinear resonator," *Phys. Rev. Lett.*, vol. 96, p. 127003, Mar 2006.

[61] Y. Sunada, K. Yuki, Z. Wang, T. Miyamura, J. Ilves, K. Matsuura, P. A. Spring, S. Tamate, S. Kono, and Y. Nakamura, "Photon-noise-tolerant dispersive readout of a superconducting qubit using a nonlinear purcell filter," *PRX Quantum*, vol. 5, p. 010307, Jan 2024.

[62] Y. Ye, J. B. Kline, S. Chen, A. Yen, and K. P. O'Brien, "Ultrafast superconducting qubit readout with the quarton coupler," *Sci. Adv.*, vol. 10, no. 41, p. eado9094, 2024.

[63] A. Manaselyan, V. Mughnetsyan, and A. Kirakosyan, "Planar quantum dots: Theoretical approaches," in *Encyclopedia of Condensed Matter Physics (Second Edition)* (T. Chakraborty, ed.), pp. 297–307, Oxford: Academic Press, second edition ed., 2024.

[64] R. C. Ashoori, “Electrons in artificial atoms,” *Nature*, vol. 379, pp. 413–419, Feb 1996.

[65] Y.-M. Huang, K. J. Singh, A.-C. Liu, C.-C. Lin, Z. Chen, K. Wang, Y. Lin, Z. Liu, T. Wu, and H.-C. Kuo, “Advances in quantum-dot-based displays,” *Nanomaterials*, vol. 10, no. 7, 2020.

[66] P. Senellart, G. Solomon, and A. White, “High-performance semiconductor quantum-dot single-photon sources,” *Nature Nanotechnology*, vol. 12, pp. 1026–1039, Nov 2017.

[67] D. L. Huffaker, G. Park, Z. Zou, O. B. Shchekin, and D. G. Deppe, “1.3 µm room-temperature gaas-based quantum-dot laser,” *Applied Physics Letters*, vol. 73, pp. 2564–2566, 11 1998.

[68] C. Melnychuk and P. Guyot-Sionnest, “Multicarrier dynamics in quantum dots,” *Chemical Reviews*, vol. 121, pp. 2325–2372, Feb 2021.

[69] B. A. Kairdolf, A. M. Smith, T. H. Stokes, M. D. Wang, A. N. Young, and S. Nie, “Semiconductor quantum dots for bioimaging and biodiagnostic applications,” *Annual Review of Analytical Chemistry*, vol. 6, no. Volume 6, 2013, pp. 143–162, 2013.

[70] H. Y. Ramírez, J. Flórez, and ⌧. S. Camacho, “Efficient control of coulomb enhanced second harmonic generation from excitonic transitions in quantum dot ensembles,” *Phys. Chem. Chem. Phys.*, vol. 17, pp. 23938–23946, 2015.

[71] P. C. J. Clark, H. Radtke, A. Pengpad, A. I. Williamson, B. F. Spencer, S. J. O. Hardman, M. A. Leontiadou, D. C. J. Neo, S. M. Fairclough, A. A. R. Watt, I. Pis, S. Nappini, F. Bondino, E. Magnano, K. Handrup, K. Schulte, M. G. Silly, F. Sirotti, and W. R. Flavell, “The passivating effect of cadmium in pbs/cds colloidal quantum dots probed by nm-scale depth profiling,” *Nanoscale*, vol. 9, pp. 6056–6067, 2017.

[72] M. A. Kastner, “The single-electron transistor,” *Rev. Mod. Phys.*, vol. 64, pp. 849–858, Jul 1992.

[73] T. Ito, T. Otsuka, S. Amaha, M. R. Delbecq, T. Nakajima, J. Yoneda, K. Takeda, G. Allison, A. Noiri, K. Kawasaki, and S. Tarucha, “Detection and control of charge states in a quintuple quantum dot,” *Scientific Reports*, vol. 6, p. 39113, Dec 2016.

[74] A. Kurzmann, H. Overweg, M. Eich, A. Pally, P. Rickhaus, R. Pisoni, Y. Lee, K. Watanabe, T. Taniguchi, T. Ihn, and K. Ensslin, “Charge detection in gate-defined bilayer graphene quantum dots,” *Nano Letters*, vol. 19, no. 8, pp. 5216–5221, 2019. PMID: 31311270.

[75] J. R. J, J. T. Mazumder, A. B. Aloshious, and R. K. Jha, "Single electron transistor based charge sensors: fabrication challenges and opportunities," *Nanoscale*, vol. 17, pp. 11960–12013, 2025.

[76] Y. Alhassid, "The statistical theory of quantum dots," *Rev. Mod. Phys.*, vol. 72, pp. 895–968, Oct 2000.

[77] C. W. J. Beenakker, "Theory of coulomb-blockade oscillations in the conductance of a quantum dot," *Phys. Rev. B*, vol. 44, pp. 1646–1656, Jul 1991.

[78] S. De Franceschi, S. Sasaki, J. M. Elzerman, W. G. van der Wiel, S. Tarucha, and L. P. Kouwenhoven, "Electron cotunneling in a semiconductor quantum dot," *Phys. Rev. Lett.*, vol. 86, pp. 878–881, Jan 2001.

[79] R. Landauer, "Spatial variation of currents and fields due to localized scatterers in metallic conduction," *IBM Journal of Research and Development*, vol. 1, no. 3, pp. 223–231, 1957.

[80] M. Büttiker, "Absence of backscattering in the quantum hall effect in multiprobe conductors," *Phys. Rev. B*, vol. 38, pp. 9375–9389, Nov 1988.

[81] G. Breit and E. Wigner, "Capture of slow neutrons," *Phys. Rev.*, vol. 49, pp. 519–531, Apr 1936.

[82] J. Gorman, D. G. Hasko, and D. A. Williams, "Charge-qubit operation of an isolated double quantum dot," *Phys. Rev. Lett.*, vol. 95, p. 090502, Aug 2005.

[83] D. Kim, D. R. Ward, C. B. Simmons, J. K. Gamble, R. Blume-Kohout, E. Nielsen, D. E. Savage, M. G. Lagally, M. Friesen, S. N. Coppersmith, and M. A. Eriksson, "Microwave-driven coherent operation of a semiconductor quantum dot charge qubit," *Nature Nanotechnology*, vol. 10, pp. 243–247, Mar 2015.

[84] M. Josefsson and M. Leijnse, "Double quantum-dot engine fueled by entanglement between electron spins," *Phys. Rev. B*, vol. 101, p. 081408, Feb 2020.

[85] Y.-Y. Liu, K. D. Petersson, J. Stehlik, J. M. Taylor, and J. R. Petta, "Photon emission from a cavity-coupled double quantum dot," *Phys. Rev. Lett.*, vol. 113, p. 036801, Jul 2014.

[86] Y.-Y. Liu, T. R. Hartke, J. Stehlik, and J. R. Petta, "Phase locking of a semiconductor double-quantum-dot single-atom maser," *Phys. Rev. A*, vol. 96, p. 053816, Nov 2017.

[87] W. G. van der Wiel, S. De Franceschi, J. M. Elzerman, T. Fujisawa, S. Tarucha, and L. P. Kouwenhoven, "Electron transport through double quantum dots," *Rev. Mod. Phys.*, vol. 75, pp. 1–22, Dec 2002.

[88] D. Bothner, M. Knufinke, H. Hattermann, R. Wölbing, B. Ferdinand, P. Weiss, S. Bernon, J. Fortágh, D. Koelle, and R. Kleiner, "Inductively coupled superconducting half wavelength resonators as persistent current traps for ultracold atoms," *New Journal of Physics*, vol. 15, p. 093024, sep 2013.

[89] L. McKenzie-Sell, J. Xie, C.-M. Lee, J. W. A. Robinson, C. Ciccarelli, and J. A. Haigh, "Low-impedance superconducting microwave resonators for strong coupling to small magnetic mode volumes," *Phys. Rev. B*, vol. 99, p. 140414, Apr 2019.

[90] S. M. Girvin, "113circuit qed: superconducting qubits coupled to microwave photons," in *Quantum Machines: Measurement and Control of Engineered Quantum Systems: Lecture Notes of the Les Houches Summer School: Volume 96, July 2011*, Oxford University Press, 06 2014.

[91] Andersson, Samuel, "Light-Matter Interactions in a Single Josephson Junction Microwave Resonator," 2024. Student Paper.

[92] D. S. Wisbey, J. Gao, M. R. Vissers, F. C. S. da Silva, J. S. Kline, L. Vale, and D. P. Pappas, "Effect of metal/substrate interfaces on radio-frequency loss in superconducting coplanar waveguides," *Journal of Applied Physics*, vol. 108, p. 093918, 11 2010.

[93] J. Goetz, F. Deppe, M. Haeberlein, F. Wulschner, C. W. Zollitsch, S. Meier, M. Fischer, P. Eder, E. Xie, K. G. Fedorov, E. P. Menzel, A. Marx, and R. Gross, "Loss mechanisms in superconducting thin film microwave resonators," *Journal of Applied Physics*, vol. 119, p. 015304, 01 2016.

[94] *Scattering Parameters and ABCD Matrices*, ch. 1, pp. 1–21. John Wiley & Sons, Ltd, 2008.

[95] J. Bylander, T. Duty, and P. Delsing, "Current measurement by real-time counting of single electrons," *Nature*, vol. 434, pp. 361–364, Mar 2005.

[96] S. J. Angus, A. J. Ferguson, A. S. Dzurak, and R. G. Clark, "A silicon radio-frequency single electron transistor," *Appl. Phys. Lett*, vol. 92, p. 112103, 03 2008.

[97] J. P. Dehollain, J. T. Muhonen, K. Y. Tan, A. Saraiva, D. N. Jamieson, A. S. Dzurak, and A. Morello, "Single-shot readout and relaxation of singlet and triplet states in exchange-coupled ^{31}P electron spins in silicon," *Phys. Rev. Lett.*, vol. 112, p. 236801, Jun 2014.

[98] D. J. Reilly, C. M. Marcus, M. P. Hanson, and A. C. Gossard, “Fast single-charge sensing with a RF quantum point contact,” *Appl. Phys. Lett.*, vol. 91, p. 162101, 10 2007.

[99] B. Thyagarajan, S. Kanhirathingal, B. Brock, J. Li, M. Blencowe, and A. Rimberg, “Fast high-fidelity charge readout by operating a cavity-embedded cooper-pair transistor in the kerr bistable regime,” *Phys. Rev. Appl.*, vol. 21, p. 014064, Jan 2024.

[100] M. Sandberg, C. M. Wilson, F. Persson, T. Bauch, G. Johansson, V. Shumeiko, T. Duty, and P. Delsing, “Tuning the field in a microwave resonator faster than the photon lifetime,” *Applied Physics Letters*, vol. 92, p. 203501, 05 2008.

[101] D. Barker, S. Lehmann, L. Namazi, M. Nilsson, C. Thelander, K. A. Dick, and V. F. Maisi, “Individually addressable double quantum dots formed with nanowire polytypes and identified by epitaxial markers,” *Applied Physics Letters*, vol. 114, p. 183502, May 2019.

[102] J. Stehlik, Y.-Y. Liu, C. M. Quintana, C. Eichler, T. R. Hartke, and J. R. Petta, “Fast charge sensing of a cavity-coupled double quantum dot using a josephson parametric amplifier,” *Phys. Rev. Appl.*, vol. 4, p. 014018, Jul 2015.

[103] C. Bruder and H. Schoeller, “Charging effects in ultrasmall quantum dots in the presence of time-varing fields,” *Phys. Rev. Lett.*, vol. 72, pp. 1076–1079, Feb 1994.

[104] G.-L. Ingold and Y. V. Nazarov, *Charge Tunneling Rates in Ultrasmall Junctions*, pp. 21–107. Boston, MA: Springer US, 1992.

[105] J.-R. Souquet, M. J. Woolley, J. Gabelli, P. Simon, and A. A. Clerk, “Photon-assisted tunnelling with nonclassical light,” *Nature Communications*, vol. 5, p. 5562, Nov 2014.

[106] T. Frey, P. J. Leek, M. Beck, K. Ensslin, A. Wallraff, and T. Ihn, “Characterization of a microwave frequency resonator via a nearby quantum dot,” *Applied Physics Letters*, vol. 98, p. 262105, 06 2011.

[107] S. Haldar, H. Havir, W. Khan, S. Lehmann, C. Thelander, K. A. Dick, and V. F. Maisi, “Energetics of microwaves probed by double quantum dot absorption.,” 2022.

[108] N. A. Masluk, I. M. Pop, A. Kamal, Z. K. Minev, and M. H. Devoret, “Microwave characterization of josephson junction arrays: Implementing a low loss superinductance,” *Phys. Rev. Lett.*, vol. 109, p. 137002, Sep 2012.

[109] P. R. Muppalla, O. Gargiulo, S. I. Mirzaei, B. P. Venkatesh, M. L. Juan, L. Grünhaupt, I. M. Pop, and G. Kirchmair, "Bistability in a mesoscopic josephson junction array resonator," *Phys. Rev. B*, vol. 97, p. 024518, Jan 2018.

[110] J. M. Martinis, S. Nam, J. Aumentado, and C. Urbina, "Rabi oscillations in a large josephson-junction qubit," *Phys. Rev. Lett.*, vol. 89, p. 117901, Aug 2002.

[111] M. Tinkham, *Introduction to Superconductivity: Second Edition*. Dover Books on Physics, Dover Publications, 2004.

[112] F. De Palma, F. Oppliger, W. Jang, S. Bosco, M. Janík, S. Calcaterra, G. Katsaros, G. Isella, D. Loss, and P. Scarlino, "Strong hole-photon coupling in planar ge for probing charge degree and strongly correlated states," *Nature Communications*, vol. 15, p. 10177, Nov 2024.

[113] L. N. Cooper, "Bound electron pairs in a degenerate fermi gas," *Phys. Rev.*, vol. 104, pp. 1189–1190, Nov 1956.

[114] A. L. Pankratov, L. S. Revin, A. V. Gordeeva, A. A. Yablokov, L. S. Kuzmin, and E. Il'ichev, "Towards a microwave single-photon counter for searching axions," *npj Quantum Information*, vol. 8, p. 61, May 2022.

[115] C. Ishii, "Josephson currents through junctions with normal metal barriers," *Progress of Theoretical Physics*, vol. 44, pp. 1525–1547, 12 1970.

[116] J. Baselmans, A. Morpurgo, B. van Wees, and T. Klapwijk, "Tunable supercurrent in superconductor/normal metal/superconductor josephson junctions," *Superlattices and Microstructures*, vol. 25, no. 5, pp. 973–982, 1999.

[117] S. A. Lemziakov, B. Karimi, S. Nakamura, D. S. Lvov, R. Upadhyay, C. D. Satrya, Z.-Y. Chen, D. Subero, Y.-C. Chang, L. B. Wang, and J. P. Pekola, "Applications of superconductor–normal metal interfaces," *Journal of Low Temperature Physics*, vol. 217, pp. 54–81, Oct 2024.

[118] S. Battisti, J. Koch, A. Paghi, L. Ruf, A. Gulian, S. Teknowijoyo, C. Cirillo, Z. M. Kakhaki, C. Attanasio, E. Scheer, A. Di Bernardo, G. De Simoni, and F. Giazotto, "Demonstration of high-impedance superconducting nbre dayem bridges," *Applied Physics Letters*, vol. 124, p. 172601, 04 2024.

[119] B. Josephson, "Possible new effects in superconductive tunnelling," *Physics Letters*, vol. 1, no. 7, pp. 251–253, 1962.

[120] P. W. Anderson and J. M. Rowell, "Probable observation of the josephson superconducting tunneling effect," *Phys. Rev. Lett.*, vol. 10, pp. 230–232, Mar 1963.

[121] V. Ambegaokar and A. Baratoff, “Tunneling between superconductors,” *Phys. Rev. Lett.*, vol. 10, pp. 486–489, Jun 1963.

[122] R. C. Jaklevic, J. Lambe, A. H. Silver, and J. E. Mercereau, “Quantum interference effects in josephson tunneling,” *Phys. Rev. Lett.*, vol. 12, pp. 159–160, Feb 1964.

[123] V. Bouchiat, D. Vion, P. Joyez, D. Esteve, and M. Devoret, “Quantum coherence with a single cooper pair,” *Physica Scripta*, vol. 1998, p. 165, Dec 2006.

[124] Y. Nakamura, Y. A. Pashkin, and J. S. Tsai, “Coherent control of macroscopic quantum states in a single-cooper-pair box,” *Nature*, vol. 398, pp. 786–788, Apr 1999.

[125] L. S. Bishop, E. Ginossar, and S. M. Girvin, “Response of the strongly driven Jaynes-Cummings oscillator,” *Phys. Rev. Lett.*, vol. 105, p. 100505, Sep 2010.

[126] A. Mavalankar, T. Pei, E. M. Gauger, J. H. Warner, G. A. D. Briggs, and E. A. Laird, “Photon-assisted tunneling and charge dephasing in a carbon nanotube double quantum dot,” *Phys. Rev. B*, vol. 93, p. 235428, Jun 2016.

[127] M. Brennan, I. Kovacic, A. Carrella, and T. Waters, “On the jump-up and jump-down frequencies of the duffing oscillator,” *Journal of Sound and Vibration*, vol. 318, no. 4, pp. 1250–1261, 2008.

[128] J. Niemeyer, “Eine einfache metode zur herstellung kleinster josephson-elemente,” *P.T.B. MITT*, 1974.

[129] J. Niemeyer and V. Kose, “Observation of large dc supercurrents at nonzero voltages in josephson tunnel junctions,” *Applied Physics Letters*, vol. 29, pp. 380–382, 09 1976.

[130] G. J. Dolan, “Offset masks for lift-off photoprocessing,” *Applied Physics Letters*, vol. 31, pp. 337–339, 09 1977.

[131] T. Holmqvist, M. Meschke, and J. P. Pekola, “Double oxidation scheme for tunnel junction fabrication,” *J. Vac. Sci. & Techol. B*, vol. 26, pp. 28–31, 01 2008.

[132] J. Stehlik, Y.-Y. Liu, C. M. Quintana, C. Eichler, T. R. Hartke, and J. R. Petta, “Fast charge sensing of a cavity-coupled double quantum dot using a josephson parametric amplifier,” *Phys. Rev. Appl.*, vol. 4, p. 014018, Jul 2015.

[133] L. Cockins, Y. Miyahara, and P. Grutter, “Spatially resolved low-frequency noise measured by atomic force microscopy,” *Phys. Rev. B*, vol. 79, p. 121309, Mar 2009.

[134] A. Aassime, G. Johansson, G. Wendin, R. J. Schoelkopf, and P. Delsing, “Radio-frequency single-electron transistor as readout device for qubits: Charge sensitivity and backaction,” *Phys. Rev. Lett.*, vol. 86, pp. 3376–3379, Apr 2001.

[135] K. Bladh, D. Gunnarsson, G. Johansson, A. Käck, G. Wendin, A. Aassime, M. Taslakov, and P. Delsing, “Reading out charge qubits with a radio-frequency single-electron-transistor,” *Physica Scripta*, vol. 2002, p. 167, jan 2002.

[136] A. Morello, J. J. Pla, F. A. Zwanenburg, K. W. Chan, K. Y. Tan, H. Huebl, M. Möttönen, C. D. Nugroho, C. Yang, J. A. van Donkelaar, A. D. C. Alves, D. N. Jamieson, C. C. Escott, L. C. L. Hollenberg, R. G. Clark, and A. S. Dzurak, “Single-shot readout of an electron spin in silicon,” *Nature*, vol. 467, pp. 687–691, Oct 2010.

[137] J. Park, H. Jang, H. Sohn, J. Yun, Y. Song, B. Kang, L. E. A. Stehouwer, D. D. Esposti, G. Scappucci, and D. Kim, “Passive and active suppression of transduced noise in silicon spin qubits,” *Nat. Commun.*, vol. 16, p. 78, Jan 2025.

[138] S. Haldar, M. Munk, H. Havir, W. Khan, S. Lehmann, C. Thelander, K. A. Dick, P. Samuelsson, P. P. Potts, and V. F. Maisi, “Coherence of an electronic two-level system under continuous charge sensing by a quantum dot detector,” *Phys. Rev. Lett.*, vol. 134, p. 023601, Jan 2025.

Scientific publications

Author contributions

Co-authors are abbreviated as follows:
Subhomoy Haldar (S.H.), Sebastian Lehmann (S.L.), Kimberly A. Dick, (K.D.), Claes Thelander (C.T.), Peter Samuelsson (P.S), Ville Maisi (V.M.), Andrea Cicovic (A.C.), Pierre Glidic (P.G.).

Paper i: Quantum Dot Source-Drain Transport Response at Microwave Frequencies

H. Havir, S. Haldar, W. Khan, S. Lehman, K. A. Dick, C. Thelander, P. Samuelsson and V. F. Maisi, *Phys. Rev. B* **108**, 205417S.H. fabricated the device with nanowires fabricated by S.L., K.D. and C.T. I performed the measurements and analysis of the data, wrote the code to calculate the numerical fits based on the theory considerations made by P.S. and V.M., and prepared the main manuscript with input from the co-authors.

Paper ii: Near-Unity Charge Readout in a Nonlinear Resonator without Matching

I designed and developed the fabrication recipe for the SQUID array resonators and fabricated the device from as-grown nanowires by S.L and K.D. I performed the measurements along with A.C. with support from P.G. and S.H. The scripts for numerical calculations were developed by V.M. who also performed the Kerr-term analysis. I analyzed the experimental data with these theory inputs and was the lead author of the manuscript along with input from V.M., A.C. and P.G. during the writing process.

Thank you to my wonderful colleagues.
Pictured, left to right: Pia, Samuel, Pierre, Ville, Me, Subhomoy, Andrea.
Not pictured: David B., Waqar, Antti, Antoine, Corentin, David.H, Ebba, Hilma.
You have all made my time here very memorable and fulfilling, I wish you all the best in your future careers.

Printed by Media-Tryck, Lund 2025 NORDIC SWAN ECOLABEL 3041 0903

LUND UNIVERSITY

Solid State Physics
Department of Physics

ISBN 978-91-8104-646-5